STRATHCLYDE UNIVERSITY

Computational Investigation Of InGaN Alloys Over The Full Composition Range

by

Fathi Elfituri

A thesis submitted in partial fulfillment for the degree of Doctor of Philosophy

in the

Faculty of Science
Physics Department

February 2014

Declaration of Authorship

This thesis is the result of the authors original research. It has been composed by the author and has not been previously submitted for examination which has led to the award of a degree.

Signed:

_____

Date:

_____

Abstract

The properties of InGaN alloys are important for many applications in optoelectronics, since the fundamental band gap of this material system spans the visible range. Calculating properties, particularly for InN, is theoretically challenging, especially obtaining accurate values for the band gap. We have developed a semi-empirical parameterization for the simulation of (In,Ga)N using the density functional based tight binding method (DFTB), where the band gaps of InN and GaN have been empirically adjusted to match experiment. This is the first application of this method to In containing materials. We demonstrate the performance of this method by calculating a range of properties for both compounds and also their alloy for a range of crystal structures (wurtzite, zincblende and, for the pure compounds, rocksalt).

There are several methods to model alloys of these materials, here the virtual crystal approximation and the cluster expansion method been used to study the alloy system of InGaN. While 8, 16 atom supercells are commonly used for cluster expansions, in this work these results are critically compared against the larger 32 atom cell, the effect of the ensemble used to simulate the alloy is also investigated by using both the Strictly Regular Solution and Generalised Quasi-Chemical approximations to provide limiting cases around the experimental conditions of Molecular Beam Epitaxy (MBE) and Metal-Organic Chemical Vapor Deposition (MOCVD) alloys.

Acknowledgements

First of all and foremost, I would like to thank my supervisor Dr. Ben Hourahine for all the guidance and advice he provided, for the stimulating discussions and most of all for the patience he still displays, especially considering the amount of time I spent on writing this thesis. Furthermore, I would like to thank my second-supervisor Dr. Carol Trager-Cowan for her important notes and advises. Also, I would like to thank the entire Semiconductor Spectroscopy and Devices group.

Last but not least, I would like to express my love and thanks to all my family members for their support and help.

Contents

List of Figures

List of Tables

List of Publications and Conferences

Publications

- Fathi Elfituri and Ben Hourahine "Simple models for InGaN alloy", Phys. Status Solidi A **209**, No. 1, 7982 (2012). DOI 10.1002/pssa.201100147
- Fathi Elfituri and Ben Hourahine "Structural Phase Stability in The III-V nitrides", (In preparation).
- Fathi Elfituri and Ben Hourahine "Bowing Behavior in InGaN alloys", (In preparation).
- Fathi Elfituri and Ben Hourahine "Size and Pressure Dependant Effects in Models of $In_xGa_{1-x}N$ Over The Full Composition Range", (In preparation).

Conferences

- Simple models for InGaN alloy *(Poster Presentation)*, (E-MRS ICAM IUMRS 2011 Spring Meeting, May 9-13, 2011 Congress Center, Nice, France).
- Virtual Crystal investgation for InGaN Alloy *(Poster Presentation)*, (NanoTP: COST Action MP0901: WG4 Meeting 2011 13-15 June 2011, University of Strathclyde, Glasgow, UK).
- Simple models for the electronic structure of InGaN alloys *(Poster Presentation)*, (9th International Conference on Nitride Semiconductors (ICNS-9) 10th - 15th July 2011 Glasgow, UK).
- Cluster Expansion for InGaN alloy *(Poster Presentation)*, (UK Nitrides Consortium (UKNC) Annual Conference, 4th-5th January 2012, The Bailbrook House Hotel, Bath, UK).
- Cluster Expansion Of Semiconductors *(Oral Presentation)*, (WG4 Theory Meeting: Advanced atomic scale modelling for nanoscale interfaces including Advanced AIMPRO workshop, University Of Surrey, Guildford, United Kingdom, June 4-7 2013)

Chapter 1

Nitride Semiconductors and their alloys

1.1 Introduction

The group-III nitrides semiconductors gallium nitride (GaN), indium nitride (InN) and aluminum nitride (AlN) and their alloys such as $In_xGa_{1-x}N$ and $In_xAl_{1-x}N$ are technologically important, particularly for optoelectronics applications such as light emited diodes LEDs [1], solar cells[2], vertical-external-cavity surface-emitting lasers [3] and vertical-cavity surface-emitting lasers [4]. Wurtzite GaN, AIN and InN form a continous alloy system whose direct band gaps cover the range from about 0.7 eV for InN [5], via 3.4 eV for GaN to 6.2 eV for AIN [6] associated with lattice constants ranged from a= 3.112 Å and c= 4.982 Å for AlN to a = 3.545 Å and c=5.703 Å for InN (see table 1.1). Thus, the III-V nitrides can

be used to fabricate into optical devices which are active at wavelengths ranging from near infrared well into the ultraviolet (See Figure 1.1). GaN based materials in principle allow the production of semiconductor devices to detect and emit the three primary colours of the visible spectrum (red, green and blue). Blue LEDs have been extremely successful and green and yellow LEDs have been recently grown [7]. This feature of group-III nitrides semiconductors opens the way for a range of applications such as imaging and graphic applications [6], while $In_xGa_{1-x}N$ is currently used in construction of green-blue-violet light emitting diodes (LEDs) and blue violet laser diodes (LDs) [1]. Furthermore, $In_xGa_{1-x}N$ based detectors, operating at short wavelengths have been constructed in several laboratories [8]. The major advantage for $In_xGa_{1-x}N$ is its direct energy gap (E_g), which leads to high efficiency in optoelectronic devices (potentially such as solar cells) [2, 9]. Highly efficent multi-junction solar cells, where the wanted band gaps are between 0.7 and 2.5 eV realized by a changing the indium composition, which means that current matching between sub-cells will be easily achieved using InGaN systems [2].

1.2 Crystal Structures

The group-III nitrides crystallise in one of three structures: wurtzite (WZ), zincblende (ZB) and rocksalt (RS). However, the wurtzite structure is the one which is thermodynamically most stable at standard conditions, i.e. at room temperature and atmospheric pressure.

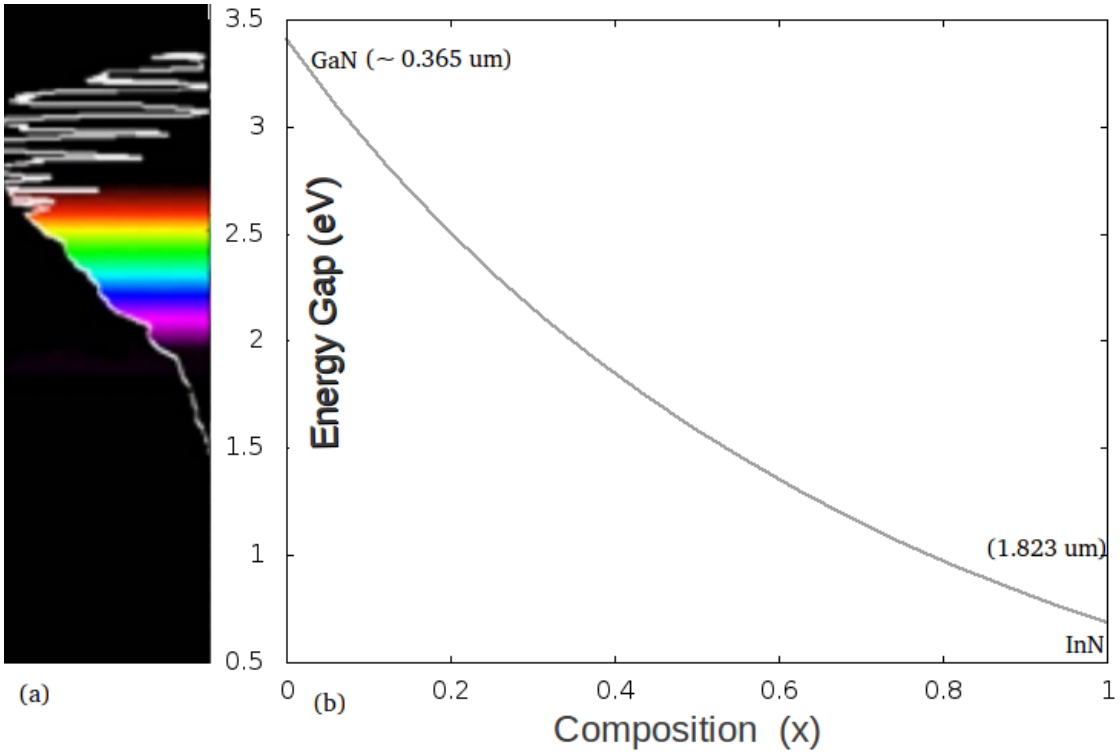

FIGURE 1.1: The visible colours of the solar spectrum (a) (taken from Ref. [5]) compared to, (b) the electronic band gaps of $In_xGa_{1-x}N$ alloys based on VCA result (see chapter 4).

1.2.1 Wurtzite:

Wurtzite is a hexagonal structure and the ideal lattice constants a and c are related by $c/a = \sqrt{8/3} \simeq 1.633$. There are four atoms in the primitive unit cell and the structure's internal parameter u is 3/8 (= 0.375), where uc corresponds to the length of the bonds parallel to [0001]. The lattice vectors for the primitive cell of wurtzite structure are written as:

$$\begin{aligned} \vec{a}_1 &= \tfrac{a}{2}\hat{x} - \tfrac{a\sqrt{3}}{2}\hat{y} \\ \vec{a}_2 &= \tfrac{a}{2}\hat{x} + \tfrac{a\sqrt{3}}{2}\hat{y} \\ \vec{a}_3 &= c\hat{z} \end{aligned} \tag{1.1}$$

In the WZ structure (Fig 1.2) there are pairs of cation and anion atoms aligned along the [0001] (or [001]) direction and attracted to each other by electrostatic forces. It is considered that these electrostatic interactions make the WZ structure more stable than the ZB, because the ionicity of these compounds is large among the III-V and II-VI compound semiconductors [10]. In the WZ structure, therefore,

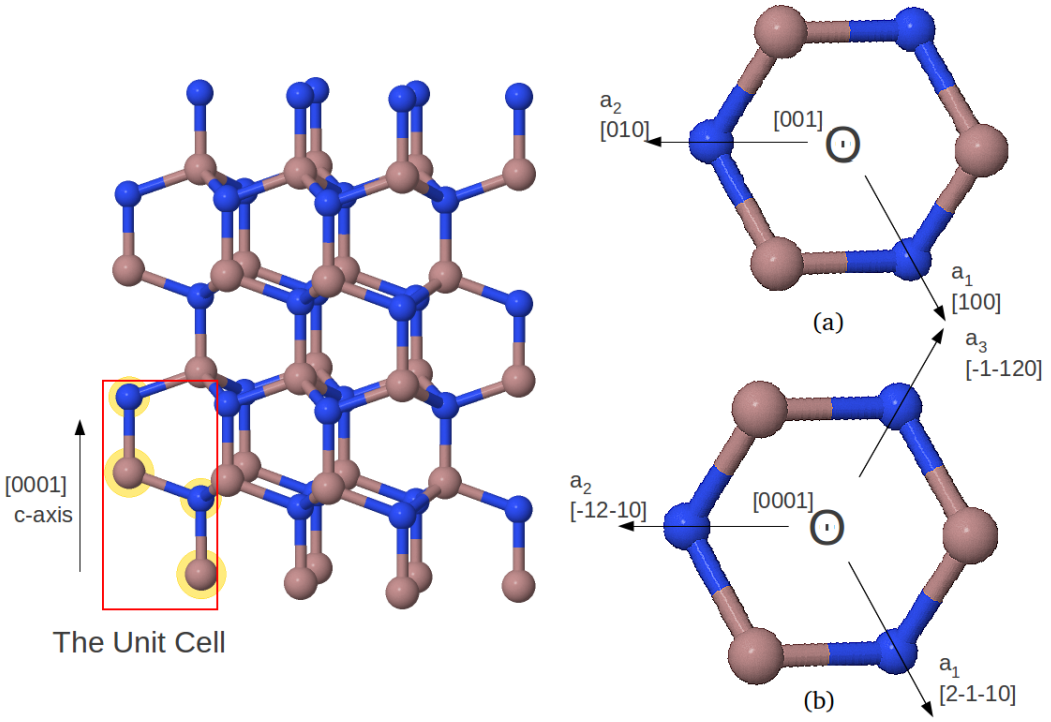

FIGURE 1.2: The wurtzite crystal structure, with atoms in the primitive unit cell marked with a box, the lattice directions in the (a) reciprocal 3-axis notation system and (b) hexagonal 4-axis notation system are illustrated.

the bond length along the [0001] direction tends to be shorter than the ideal WZ distance. In fact the, c/a ratio is also smaller than the ideal (1.633) for most of the WZ type materials, as shown in table 1.1. We can define coordinates for the WZ-structure as fractions of the lattice vectors; one choice for the primitive unit cell is where cations atoms (e.g. Ga or In) are positioned such that one atom is at the origin, [0, 0, 0] and the other at [1/3, 1/3, 1/2] and the N atoms are

positioned directly above the cations atoms along [0001]. In the "ideal" wurtzite structure, these are at [0, 0, 3/8] and [1/3, 1/3, 7/8]. The hexagonal system can be described as either a four-axis coordinate system or a three-axis system. The use of four indices for directions in hexagonal system is based on four component vectors, parallel to a_1, a_2, a_3 and c, the relationships between the three axis indices directions $[UVW]$ and the four axis indices directions $[hkil]$ are given by [11];

$$\begin{aligned} U &= h - i \qquad h = \tfrac{1}{3}(2U - V) \\ V &= k - 1 \qquad k = \tfrac{1}{3}(2V - U) \\ W &= l \qquad\quad i = -(h + k) \quad = -\tfrac{1}{3}(U + V) \\ & \qquad\quad l = W \end{aligned} \tag{1.2}$$

1.2.2 Zincblende

The cubic-zincblende structure (*Sphalerite*) Fig 1.3, is similar to the diamond structure and may be viewed as two interpenetrating fcc lattices displaced from each other by one quarter of a body diagonal. The cubic zinc blende structure results when cation atoms are positioned on one fcc lattice and N atoms on the other fcc lattice. The coordinates in the primitive unit cell of the cation atoms are [0, 0, 0] and the N atom at [1/4, 1/4, 1/4]. The lattice vectors for zincblende structure written as:

$$\begin{aligned} \vec{a}_1 &= \tfrac{a_0}{2}\hat{y} + \tfrac{a_0}{2}\hat{z} \\ \vec{a}_2 &= \tfrac{a_0}{2}\hat{x} + \tfrac{a_0}{2}\hat{z} \\ \vec{a}_3 &= \tfrac{a_0}{2}\hat{x} + \tfrac{a_0}{2}\hat{y} \end{aligned} \tag{1.3}$$

	a^{WZ} (Å)	c^{WZ} (Å)	c/a	u	a_0^{ZB} (Å)
GaN[a]	3.189	5.185	1.626	0.3768	4.50
InN[a]	3.545	5.703	1.613	0.3790	4.98
AlN[a]	3.112	4.982	1.601	0.3819	4.38[e]
ZnO[b]	3.25	5.21	1.603	...	4.595
MgO[c]	3.45	...	1.20	0.50	...
CdO[c]	3.60	...	1.55	0.391	...
$C^{d}_{Lonsdaleite/diamond}$	2.51	4.12	1.641	...	...

TABLE 1.1: The lattice constants for wurtzite and zincblende materials from Refs. a-[13], b-[14], c-[15], d-[16], e-[17].

1.2.3 Rocksalt:

The rocksalt structure occurs for nitrides at high pressure conditions (≈ 13.5 GPa for InN Ref. [12]), the primitive lattice vectors of this structure are the same as ZB but in this case the cation atom is positioned at the origin, [0, 0, 0] and the N atoms are positioned at [1/2, 1/2, 1/2].

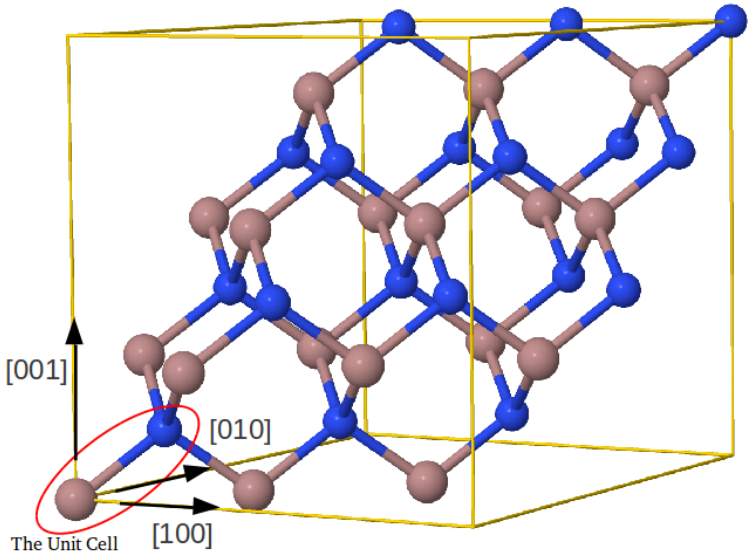

FIGURE 1.3: The zincblende crystal structure, with atoms in the primitive unit cell marked and lattice directions.

1.3 The Electronic Band-Structure Structure of III-N Semiconductors

When atoms approach to form a solid, their discrete atomic energy levels transform into energy bands due to overlap of the atomic functions to form (eventually) a continuum of states (in the limit of large numbers of atoms). The band structure determines the optical and electrical properties of semiconductors materials. Wurtzite and zincblende nitrides (In, Ga, Al)N at room temperature and low pressure are direct band gap semiconductors which means that the fundamental optical transitions of lowest energy (between the highest valence band and lowest conduction band) take place at or near the Γ-point ($|\mathbf{k}|$=0) of the Brillouin zone (BZ). Direct-gap semiconductors are more effective in optoelectric applications than indirect-gap ones. This is because in the former, electrons can make direct transitions between the conduction (E_c) and valence bands (E_v) by absorption or emission of a photon of energy equal to the band gap. This occurs because photons with energy similar to the band gap (E_g) have very little momentum (E_g/c, where c is the speed of light). To conserve both energy and momentum, direct optical transitions therefore occur nearly vertically between E_v and E_c. To transfer an electron between E_v and E_c in an indirect gap semiconductor, phonons must be created or absorbed, and these phonon-assisted processes are much slower than direct transitions. [18].

1.3.1 GaN

The GaN valence band splits into three bands with symmetry labels Γ_9, Γ_{7a} and Γ_{7b} for wurtzite and Γ_8, Γ_6[1] for zincblende under the influence of crystal field and the spin-orbit interactions [20] (see section 2.5.3). Figures 1.4-b and 1.5 shows the ordering of the band structure for ZB-InN and WZ-InN respectively (which is same as in GaN), the holes associated with the Γ_9, Γ_{7a} and Γ_{7b} bands are called heavy, light and split-off band holes, respectively. The currently accepted experimental value for the wurtzite GaN band gap is $\approx$ 3.510 eV according to Ref. [21] (or more recent value 3.47 eV [22]) at 0 K and 3.41 eV at 300 K [22] and for zincblende is $\approx$ 3.23 eV at room temperature [23].

1.3.2 InN

Early research indicated that the value of the energy gap of indium nitride was about 1.9 eV [24, 25], while the current value is $\approx$ 0.7 eV for the wurtzite case and about 0.60 eV for zincblende [26] which is now widely accepted on the basis of later theoretical [20, 27] and experimental [28, 29] research. The recent availability of InN with better crystalline quality (e.g. modern material shows good quality x-ray diffraction and photoluminescence properties [30] with XRD rocking curve peaks of $< 1^\circ$ width.) led to the a suggestion that the previous InN band gap value was in error due to the accidental formation of oxynitrides in early samples [31],

[1] Γ_8 and Γ_6 in figure 1.4 and Γ_9, Γ_9, Γ_{7a} and Γ_{7b} in figure 1.5 are in the symmetry notation of Ref. [19], and used here to label the energy bands.

and/or due to the Burstein-Moss shift[2]. This effect arises from the Pauli exclusion principle and describes how adding electrons or holes to semiconductors [33], where the electron carrier concentration exceeds the conduction band edge density of states, causes an apparent absorption shift of up to E_g+ Fermi energy E_f [34].

1.4 Effective Masses

The effective mass of a carriers is a parameter characteristic of metalic or semiconductor materials, which describes the effective movement of electrons or holes inside the solid under the effect of atomic and external potentials (e.g. an applied electric field). Light effective mass materials such as InN can be used for high-frequency electronic devices, where a small effective mass means that the electrons respond more quickly to the applied electric field, and that means that they can change direction quickly when the field changes its direction. One example of the use of materials with a higher effective mass would be [0001] WZ GaN based quantum well lasers, which require high carrier densities to generate optical gain, which is possible due to their heavier (see table 1.2 for values of the effective masses) hole effective mass [35].

In solid state physics, there are many different definitions used for the effective mass such as the conductivity, density-of-states, optical effective mass and cyclotron effective mass. The most commonly used theoretical definition of the effective mass is inverse of the second derivative of the energy E with respect to

[2]The Burstein-Moss shift is greatest in semiconductors with low effective masses. That is because a low value of effective mass means that the curvature of the band is high (equation 1.9) and the density of states are low. With low DOS, Fermi energy E_f rises significantly as electrons are added to the conduction band [32].

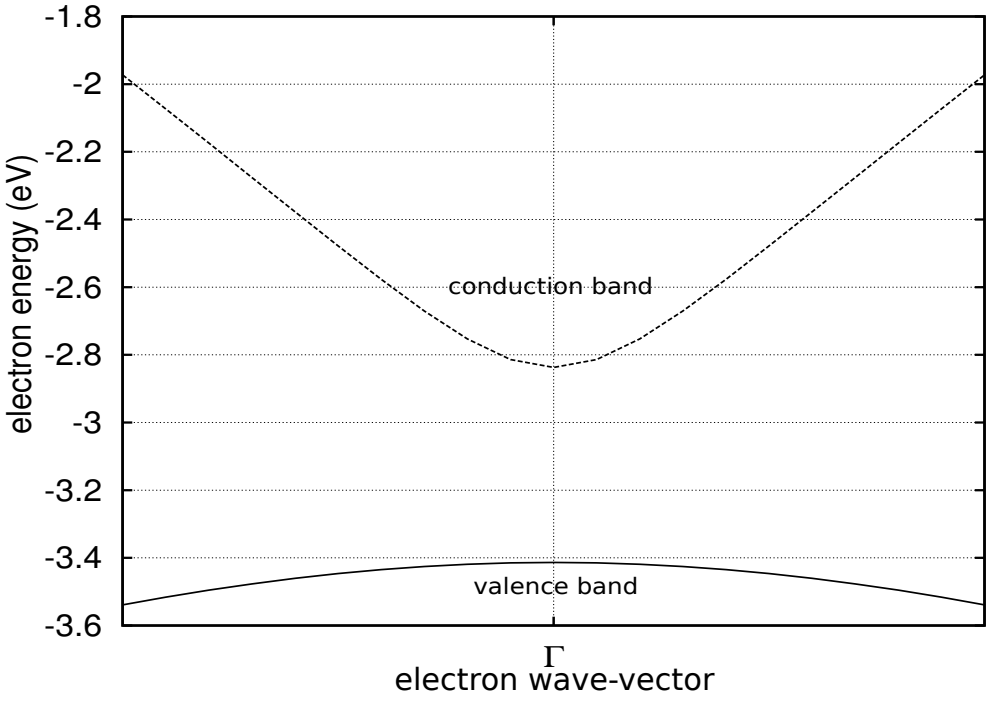

a: ZB-InN without spin-orbit interactions

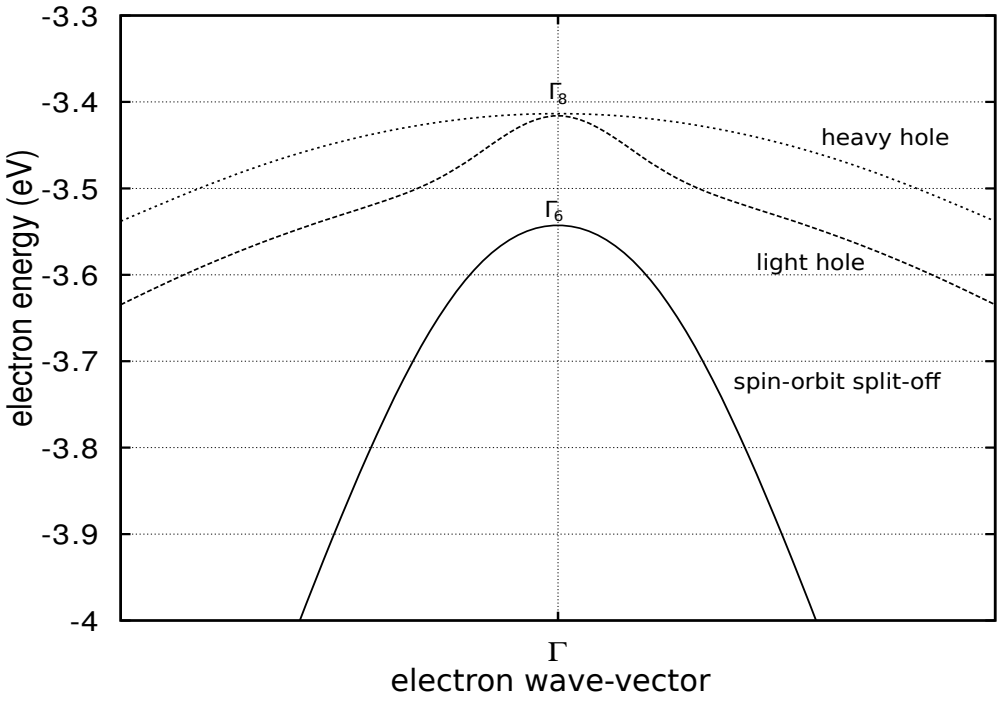

b: valence band splitting with spin-orbit interactions

FIGURE 1.4: Illustration of the band structure of ZB-InN along the [111] direction (a) without spin-orbit interactions (b) with spin-orbit interactions.

wave vector $\mathbf{k}$ i.e. the curvature of the band (see equation 1.9) which used in this thesis.

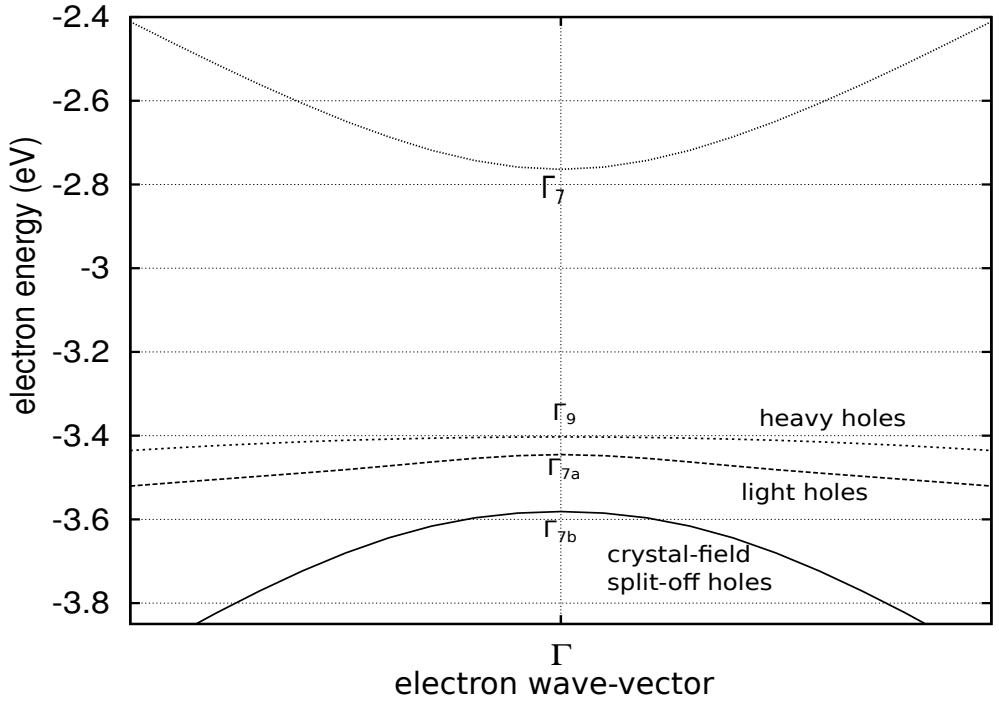

FIGURE 1.5: The band structure of WZ-InN with spin-orbit interactions, plotted along [0001].

When an electron is moving inside a solid material, the force from the electrons and nuclei will affect its movement, and induce a change in the electron wave vector **k**. The free electron energy is often represented according the relation 1.4 [36], which for semiconductors is used for the nearly parabolic region near to the valence band maximum and conduction band.

$$E(k) = \frac{\hbar^2 k^2}{2m^*} \tag{1.4}$$

where m^* is called the effective mass for a mobile particle within the crystal. To derive the effective mass, starting from the expectation value of the velocity (group velocity), given by [36];

$$\langle \upsilon \rangle \equiv \upsilon_g = \frac{1}{\hbar}\frac{dE}{dk} \tag{1.5}$$

and an external force F, which induces a change in the particle wave vector;

$$\hbar\frac{dk}{dt} = F \tag{1.6}$$

From equation 1.5;

$$\frac{d\langle \upsilon \rangle}{dt} = \frac{1}{\hbar}\frac{d}{dt}\frac{dE}{dk} \tag{1.7}$$

then from equation 1.5 we can rewrite equation 1.7 as:

$$\frac{1}{\hbar}\frac{d}{dt}\frac{dE}{dk} = \frac{1}{\hbar}\frac{dk}{dt}\frac{d^2E}{dk^2} \tag{1.8}$$

which in turn gives;

$$\frac{1}{m^*} = \frac{1}{\hbar^2}\frac{d^2E}{dk^2} \tag{1.9}$$

where m^* the effective mass. The general form of the inverse effective mass $\frac{1}{m^*}$ is given by;

$$\left(\frac{1}{m^*}\right)_{ij} = \frac{1}{\hbar^2}\frac{\partial^2 E}{\partial k_i \partial k_j} \tag{1.10}$$

where i and j are label the directions.

Without spin-orbit interactions the valence bands of ZB materials are not split, as shown in Fig 1.4-a, in this case there is only the electrons effective mass from the conduction band (CB) curve and one hole effective mass from the valence band

	$m_e^\star$	$m_{hh}^\star$	$m_{lh}^\star$	$m_{ch}^\star$
theo. GaN	0.21	2.00	1.22	0.21
expt. GaN	0.228^a	1.76^b	0.419^b	0.299^b
theo. InN	0.06	1.98	1.02	0.08
expt. InN	0.037^c	...	...	...

TABLE 1.2: The effective masses of hexagonal GaN and InN in directions parallel to the c-axis ([0001]) for electrons, heavy and light holes and the split-off band holes in units of m_0 compared to theoretical (theo.) [20] and experimental (expt.) a-[37], b-[38] and c-[39] values

(VB) curve which can be calculated *(Note:The calculation is done over a very small distance around the* Γ*-point (k=0) where the curves are well approximated by a parabola, i.e. equation 1.4 represents the dispersion well).* But in fact when electrons move around positive charges (nuclei) at relativistic speeds, the existence of the nuclear electric field leads to a magnetic field in the electron frame of rest, splitting the band structures due to this effect. This splitting occurs in the valence band as shown in Fig. 1.4-b for the ZB case and Fig. 1.5 for the WZ, and in this case we can calculate the effective mass for light-holes (m_{lh}^*), heavy-holes (m_{hh}^*), crystal field split-off holes[3] (m_{ch}^*) for WZ, spin-orbit split-off holes[4] (m_{so}^*), and electrons (m_e^*) by applying equation 1.9 to these separate curves.

Label	Cartesian Coordinates (real space)	Lattice Coordinates (reciprocal space)
Γ	0, 0, 0	0, 0, 0
A	0, 0, 1/2	0, 0, 1/2
K	2/3, 1/3, 0	1/3, 1/3, 0
M	1/2, 0, 0	1/2, 0, 0
L	1/2, 0, 1/2	1/2, 0, 1/2

TABLE 1.3: The k-vector coordinates of high symmetry points in the Brillouin zone of WZ Brillouin zone (taken from [42]).

[3]The holes effective mass of the bands which split due to crystal field which is from a static electric field produced by a the surrounding charge distribution (primarily the anion neighbors) [40]

[4]The main difference between the valence band structure of ZB and WZ crystals is the crystal field splitting absent in the ZB structures because of the cubic symmetry. [41]

Label	Cartesian Coordinates (real space)	Lattice Coordinates (reciprocal space)
Γ	0, 0, 0	0, 0, 0
X	0, 1, 0	1/2, 0, 1/2
L	1/2, 1/2, 1/2	1/2, 1/2, 1/2
W	1/2, 1, 0	1/2, 1/4, 3/4

TABLE 1.4: The k-vector coordinates of high symmetry points in the Brillouin zone of ZB Brillouin zone (taken from [42]).

1.5 Linear Elastic Constants for Hexagonal and Cubic Structures

The knowledge of elastic constants is required for studying the effect of strain on the material properties, where these constants describe the response to an applied macroscopic stress. Also by knowledge of elastic constants, the critical thickness of the material for misfit dislocation[5] generation for growth on non-lattice matched substrate can be calculated [43].

There are two important tensors that link stress (σ) to strain (ϵ) in crystals, namely the elastic compliance tensor (S) that links an induced strain to an applied stress,

$$\epsilon_{ik} = \sum_{j,l} S_{ijkl}\sigma_{jl} \tag{1.11}$$

and the elastic constant tensor (C)that gives the value of an applied stress required to produce a given strain:

[5]The misfit dislocations relieve lateral stress when the lattice constant of the substrate and layer are different . This occurs via the termination of half planes of atoms at the dislocation core allowing relaxation of the lattice.

$$\sigma_{ik} = \frac{\partial E}{\partial \epsilon_{ik}} = \sum_{j,l} C_{ijkl}\epsilon_{jl} \tag{1.12}$$

where C_{ijkl} are the elastic stiffness coefficients, which are characteristic properties of the solid. The energy that accompanies a particular strain is

$$E = \frac{1}{2}\sum_{j,l} C_{ijkl}\epsilon_{ij}\epsilon_{kl} \tag{1.13}$$

Although there are 3^4 terms in the full elastic constant tensor, the number of independent terms is smaller. Use of the symmetry implicit in the Voigt notation [44], namely that $C_{ijkl} = C_{jikl} = C_{ijlk} = C_{jilk}$, reduces the number of independent coefficients to 6×6. Within the Voigt notation, we also have the symmetry that $C_{nm} = C_{mn}$ (where C_{nm} is used to describe C_{ijkl} with $m = ij$ and $n = lk$ [18]), the maximum number of independet coefficients is 27. This number of coefficients will reduced further by crystal symmetry. For the hexagonal lattice there are six nonzero independent elastic stiffiness constants namely $C_{11}, C_{12}, C_{13}, C_{44}$ and C_{66}, where $C_{66} = (C_{11} - C_{12})/2$ [45]. So, the elastic tensor for a hexagonal material can be written as:

$$C_{Hex.} = \begin{pmatrix} C_{11} & C_{12} & C_{13} & 0 & 0 & 0 \\ C_{12} & C_{11} & C_{13} & 0 & 0 & 0 \\ C_{13} & C_{13} & C_{33} & 0 & 0 & 0 \\ 0 & 0 & 0 & C_{44} & 0 & 0 \\ 0 & 0 & 0 & 0 & C_{44} & 0 \\ 0 & 0 & 0 & 0 & 0 & C_{66} \end{pmatrix} \tag{1.14}$$

and the bulk modulus B is given by [45];

$$B = \frac{C_{33}\left(C_{11}C_{12}\right) - 2\left(C_{13}\right)^2}{C_{11} + C_{12} + 2C_{33} - 4C_{13}} \tag{1.15}$$

and giving the response to isotropic pressure pressure. For the cubic lattice, to which the zinc blende and diamond structure semiconductors belong, there are only three nonzero independent elastic stiffiness constants namely C_{11}, C_{12} and C_{44}, and the elastic tensor is written as:

$$C_{Cub.} = \begin{pmatrix} C_{11} & C_{12} & C_{12} & 0 & 0 & 0 \\ C_{12} & C_{11} & C_{12} & 0 & 0 & 0 \\ C_{12} & C_{12} & C_{11} & 0 & 0 & 0 \\ 0 & 0 & 0 & C_{44} & 0 & 0 \\ 0 & 0 & 0 & 0 & C_{44} & 0 \\ 0 & 0 & 0 & 0 & 0 & C_{44} \end{pmatrix} \tag{1.16}$$

where the bulk modulus for the cubic case is given by [18];

$$B = \frac{C_{11} + C_{12}}{3} \tag{1.17}$$

1.6 Crystal Growth

III-Nitrides Semiconductor GaN, AlN, InN and their ternaries alloys are usually grown with hydride vapour phase epitaxy (HVPE), metal-organic chemical vapour deposition (MOCVD) or molecular beam epitaxy (MBE).[6] HVPE methods are usually used to grow thick GaN layers [47, 48], whereas for thin layers and hetero-junctions formed by the above binaries and their alloys, growth is usually by either MOCVD or MBE. The MBE growth is operated in an ultra-high vacuum (UHV) environment and relatively low growth temperature (e.g. the low temperature-GaN buffer layer is grown at 650 °C before the epitaxial growth of the GaN layer at 820 °C [49].). This can be an advantage over MOVPE for obtaining high quality InN which has a low dissociation temperature [49]. There are many substrates used for III-nitrides growth such as, sapphire (Al_2O_3), silicon (Si), silicon carbide (SiC), gallium arsenide (GaAs), zinc oxide (ZnO) and gallium nitride itself. The lattice mismatch depends on the used substrate, e.g. GaN on GaN substrate has a 0 % lattice mismatch while for GaN on sapphire is about 16 %, and InN on a GaN substrate has lattice mismatch of about 10 % [49].

[6] Grown AlN,GaN and InN as liquid melt is difficult due to their the high melting point temperature and corresponding high nitrogen pressures [46]

1.7 Structure of the Thesis

The present work is motivated by an interest in investigating the group-III nitrides namely indium nitride (InN), gallium nitride (GaN) and their alloy InGaN. It is based on systematic theoretical studies using the density functional based tight binding methods (DFTB). This chapter presents general information about the nitride semiconductors and their alloys including their structures, fundamental band gap, effective masses, lattice and elastic constants. Chapter 2, describes the theory of modelling crystals, and focuses on DFTB, since it is the method used in this work. In chapter 3, the results obtained for structural and electronic properties of bulk InN and GaN, by using a new set of semiempircal parameters are introduced including the first application of DFTB to InN, and using an independent parameterization for GaN (see Ref. [50] for the earlier work on GaN defects). The study of InGaN by using virtual crystal approximation (VCA) together with DFTB is presented in chapter 4, here the variation of InGaN properties with In composition have been described comparing with other theory and experiment from literature. The calculations in chapter 4 have been repeated with the more physical method, of cluster expansion (CEM) in chapter 5. Finaly chapter 6 gives a summary of the thesis and future work.

Chapter 2

Theory of Modelling Crystals

This chapter gives brief reviews of density functional theory based tight binding (DFTB) which is used later in this thesis for the calculations. The Many Body Problem, Born-Oppenheimer approximation, Hartree-Fock method and Density Functional Theory are also reviewed.

2.1 The Many Body Problem

A system in quantum mechanics is called many body if it contains two or more particles. That system is usually described by the many body *Schrödinger equation*

$$\hat{H}\Psi = E\Psi \tag{2.1}$$

where $\hat{H}$ is the Hamiltonian and E is the energy of the system (the time independent form is shown here). The wavefunction Ψ describes the system; in the

case of a crystal it is a function of the coordinates of electrons and nuclei, r and R respectively. The time independent Hamiltonian for equation 2.1 for a collection of atoms is then

$$\begin{aligned}\hat{H} = &-\frac{1}{2}\sum_{i}^{N_e}\nabla_i^2 - \sum_{j=1}^{N_n}\frac{1}{2M_j}\nabla_j^2 + \frac{1}{2}\sum_{i,k=1,i\neq k}^{N_e}\frac{1}{\mid \vec{r}_i - \vec{r}_k \mid} \\ &- \sum_{i,j=1}^{N_n,N_e}\frac{Z_j}{\mid \vec{r}_i - \vec{R}_j \mid} + \frac{1}{2}\sum_{j,l=1,j\neq l}^{N_n}\frac{Z_j Z_l}{\mid \vec{R}_j - \vec{R}_l \mid}\end{aligned} \tag{2.2}$$

where M_j and Z_j are the mass and charge of the jth nucleus respectively and N_e and N_n are the number of electrons and nuclei respectively. We can rewrite the Hamiltonian in simple form as:

$$\hat{H} = \underbrace{\hat{T}_e}_{electrons-K.E.} + \overbrace{\hat{T}_n}^{nuclei-K.E.} + \underbrace{\hat{V}_{ee}}_{electrons-P.E.} + \overbrace{\hat{V}_{en}}^{electron-nucleus-P.E} + \underbrace{\hat{V}_{nn}}_{nuclei-P.E} \tag{2.3}$$

where K.E and P.E denote the kinetic energy and potential energy respectively.

- The electron (e) kinetic energy;

$$\hat{T}_e = -\frac{1}{2}\sum_{i}^{N_e}\nabla_i^2 \tag{2.4}$$

- The nuclear (n) kinetic energy;

$$\hat{T}_n = -\sum_{j=1}^{N_n}\frac{1}{2M_j}\nabla_j^2 \tag{2.5}$$

• The electron-electron (ee) repulsion;

$$\hat{V}_{ee} = +\frac{1}{2} \sum_{i,k=1,i\neq k}^{N_e} \frac{1}{\mid \vec{r}_i - \vec{r}_k \mid} \tag{2.6}$$

• The electron-nuclear (en) attraction;

$$\hat{V}_{en} = -\sum_{i,j=1}^{N_n,N_e} \frac{Z_j}{\mid \vec{r}_i - \vec{R}_j \mid} \tag{2.7}$$

• The nuclear-nuclear (nn) repulsion.

$$\hat{V}_{nn} = +\frac{1}{2} \sum_{j,l=1,j\neq l}^{N_n} \frac{Z_j Z_l}{\mid \vec{R}_j - \vec{R}_l \mid} \tag{2.8}$$

Solving equation 2.1 by using the Hamiltonian given in equation 2.2 is practically very difficult for any system with more particles than the hydrogen atom. So to make the problem solvable it is necessary to use some approximations.

2.2 Born-Oppenheimer approximation

In general the total Hamiltonian for a system including N_e electrons and N_n nuclei is just the sum of the terms 2.4 – 2.8 as in equation 2.2. The Schrödinger equation obtained by using the Hamiltonian in equation 2.2 is then impossible to solve exactly. So, to approximate the solution the *Born-Oppenheimer approximation* states that the nuclei are very heavy as compared to the electrons, hence the electrons are assumed to move instantaneously on the time scale of the movement

of the nuclei. By this assumption the nuclear kinetic energy becomes zero and equation 2.2 becomes;

$$\hat{H} = -\frac{1}{2}\sum_{i}^{N_e} \bigtriangledown_i^2 + \frac{1}{2}\sum_{i,k=1,i\neq k}^{N_e} \frac{1}{\mid \vec{r}_i - \vec{r}_k \mid} - \sum_{i,j=1}^{N_n,N_e} \frac{Z_j}{\mid \vec{r}_i - \vec{R}_j \mid} + \frac{1}{2}\sum_{j,l=1,j\neq l}^{N_n} \frac{Z_j Z_l}{\mid \vec{R}_j - \vec{R}_l \mid} \tag{2.9}$$

The nuclear configuration is then fixed, at some value $\vec{R}_A$, and we solve for the electronic wavefunction $\Psi(\vec{r}, \vec{R}_A)$, which depends only parametrically on $\vec{R}$. If we do this for a range of $\vec{R}$, we obtain the potential energy surface along which the nuclei move, with the electronic Hamiltonian for the fixed nuclear configuration becoming;

$$\hat{H}^e = \hat{T}_e(\vec{r}) + \hat{V}_{ee}(\vec{r}) + \hat{V}_{en}(\vec{r}; \vec{R}) + \hat{V}_{nn}(\vec{R}) \tag{2.10}$$

2.3 Hartree-Fock Method

We need to make some further approximations to solve the electronic Schrödinger equation;

$$H^{\text{eff}}\Psi^{\text{eff}}(\vec{r}, \vec{R}) = E^{\text{eff}}(\vec{R})\psi^{\text{eff}}(\vec{r}, \vec{R}) \tag{2.11}$$

Using H_2 as an example, we start by decomposing Ψ^{eff} into a combination of molecular orbitals (MOs) where each MO is a one-electron wavefunction (ϕ_n)

$$\Psi^e(\vec{r}) = \phi_1(\vec{r_1})\phi_2(\vec{r_2}) \tag{2.12}$$

But this is not a physically correct wavefunction, as it is required to be antisymmetric: *swapping the coordinates of two electrons should lead to a sign change.* A wave function which is antisymmetric can be written in the form;

$$\Psi^e(\vec{r}) = \phi_1(\vec{r_1})\phi_2(\vec{r_2}) - \phi_1(\vec{r_2})\phi_2(\vec{r_1}) \tag{2.13}$$

More generally, the antisymmetry of the wavefunction can be obtained by constructing the wavefunction as a Slater determinant [51] as below;

$$\Psi^e = \frac{1}{\sqrt{(N!)}} \begin{vmatrix} \phi_1(1) & \phi_2(1) & \dots & \phi_N(1) \\ \phi_1(2) & \phi_2(2) & \dots & \phi_N(2) \\ \dots & \dots & \dots & \dots \\ \phi_1(N) & \phi_2(N) & \dots & \phi_N(N) \end{vmatrix} \tag{2.14}$$

where the orbital (ϕ_i), contains also the spin of the electron.

The MOs (ϕ_i) are often written as linear combinations of pre-defined one-electron functions (basis functions or atomic orbitals (AOs))

$$\phi_i = \sum_{k,i}^{N} \mathrm{C}_{ki}\chi_k \tag{2.15}$$

where, C_{ki} the expansion coefficients and χ_ks are the basis functions or AOs.

This form of wavefunction depends on the coefficients C_{ki}. The Hartree-Fock equations which can be solved by the self-consistent field (SCF) [51] method, can be derived by finding the coefficients C_{ki} in equation 2.15 that give the lowest energy consistent with a wavefunction of the form 2.14.

2.4 Density Functional Theory (DFT)

Density functional theory (DFT) is a computational method that derives properties of solids based on a determination of the *electron density* (ρ) of the system, instead of the wavefunction. Unlike the wavefunction, which is sometimes argued to be a mathematical construct instead of a physical reality, the electron density is a measurable physical quantity. In DFT, the total energy of the non-degenerate ground state is a functional[1] of the ground-state density only, and all ground state properties can be expressed as a functional of this density (Hohenberg and Kohn [52]), such as its energy E. For a given (non-degenerate) ground state density (ρ) there is a unique external potential V_{ext} that can produce the density (ρ) as its ground state. Therefore there is a unique one to one correspondence between the potential V_{ext}, the many-body ground state $\psi(\vec{r}_1, \vec{r}_2, \vec{r}_3, ..., \vec{r}_N)$ and the ground state charge density (ρ). Thus the energy of the system must be a functional of this density;

$$E[\rho] = \int V_{ext}(r)\rho(\vec{r}) + F[\rho] \tag{2.16}$$

[1] a fanction of a function

where the functional F describes the kinetic energy of the electrons T and the Coulomb interaction between them V.

$$F[\rho] = \langle \psi(\rho) | T(\rho) + V(\rho) | \psi(\rho) \rangle \tag{2.17}$$

While the Hohenberg-Kohn theory shows that the energy can be calculated from the electron density, in practice the Kohn-Sham equations, which expand the density as a set of single-particle wavefunctions, are used for real calculations. The density is then given by sum of the densities of the single-particle states;

$$\rho(r) = \sum_{i=1}^{N} |\psi_i(\vec{r})|^2 \tag{2.18}$$

As these are single-particle wavefunctions, to include many electron effects in the interacting $T[\rho]$ and $V[\rho]$, we have to include the exchange-correlation functional $E_{xc}[\rho]$ and $E[\rho]$ becomes;

$$E[\rho] = T_0[\rho] + \int V(\vec{r})\rho(\vec{r})d^3\vec{r} + E_{xc}[\rho] \tag{2.19}$$

where

$$T_0[\rho] = \left\langle \psi(\vec{r}) \right| - \frac{\nabla^2}{2} \left| \psi(\vec{r}) \right\rangle \tag{2.20}$$

The Kohn-Sham equations can be written as:

$$\left[-\frac{\nabla^2}{2} + V_{\text{eff}}[\rho(\vec{r})] \right] \psi_i(\vec{r}) = \varepsilon_i \psi_i(\vec{r}) \tag{2.21}$$

for Kohn-Sham states, ψ_i and eigenvalues ε_i, where V_{eff} is the effective potential and is given by:

$$V_{\text{eff}}[\rho(\vec{r})] = V_{\text{ext}}(\vec{r}) + \int \frac{\rho(\vec{r'})}{|\vec{r} - \vec{r'}|} d^3\vec{r'} + \underbrace{\frac{\delta E_{xc}[\rho(\vec{r})]}{\delta\rho(\vec{r})}}_{V_{xc}} \tag{2.22}$$

Equation 2.21 must be solved self-consistently due to the dependence of V_{eff} on its solutions though Equations 2.18 and 2.22.

2.5 Density Functional Based Tight Binding (DFTB)

The total energy in density functional theory of a system of N_e electrons in the field of N_n nuclei at positions $\vec{R}$ can be expressed as unique functional of charge density $\rho(\vec{r})$ as given in equation 2.21.

Equation 2.21 can be approximated, to give the density functional based tight binding DFTB method, where the energy of a density ρ is expanded around a reference density $\rho_0(\vec{r})$ to second order, where $\delta\rho \equiv \delta\rho(\vec{r}) = \rho - \rho_0$ [53];

$$\begin{aligned} E[\rho] = &\sum_{i=1}^{\text{occ.}} \langle \psi_i(\vec{r}) \mid H^0 \mid \psi_i(\vec{r}) \rangle - \frac{1}{2} \int\int \frac{\rho_0' \rho_0}{\mid \vec{r} - \vec{r'} \mid} d^3\vec{r'} d^3\vec{r} + \\ &E_{xc}[\rho_0] - \int V_{xc}[\rho_0]\rho_0 d^3\vec{r} + V_{nn} + \frac{1}{2} \int\int \left(\frac{1}{\mid \vec{r} - \vec{r'} \mid} + \frac{\delta^2 E_{xc}}{\delta\rho\delta\rho'} \right) \delta\rho\delta\rho' \end{aligned} \tag{2.23}$$

Here, the sum is over the occupied single-particle energies ε_i and $\rho_0' = \rho_0(\vec{r'})$

In equation 2.23, the linear terms in $\delta\rho$ cancel each other at any arbitray input density ρ_0 [54, 55]. The total energy corrected to second order in the density fluctuations by simple transformation is

$$E_{\mathrm{DFTB}} = \langle\psi(\vec{r}) \mid H^0[\rho(\vec{r})] \mid \psi(\vec{r})\rangle + E_{\mathrm{rep}}[\rho_0] + E^2[\delta\rho(\vec{r}), \rho_0(\vec{r})] + \ldots \tag{2.24}$$

where

- H^0 is the Hamilton operator for the reference system, given by

$$H^0 = -\frac{\nabla^2}{2} + V_{\mathrm{ext}} + \int \frac{\rho_0'}{\mid \vec{r} - \vec{r'} \mid} d^3\vec{r'} + V_{xc}(\rho_0) \tag{2.25}$$

- V_{eff} is the effective potential and given by

$$V_{\mathrm{eff}}[\rho_0] = V_{\mathrm{ext}}(\vec{r}) + \int \frac{\rho_0(\vec{r'})}{|\vec{r} - \vec{r'}|} d^3\vec{r'} + \overbrace{\frac{\delta E_{xc}[\rho_0(\vec{r})]}{\delta\rho_0(\vec{r})}}^{V_{xc}[\rho_0]} \tag{2.26}$$

- E_{rep} is the repulsive energy contribution containing the double counting terms of equation 2.23 and given by

$$E_{\mathrm{rep}}[\rho_0] = -\frac{1}{2}\int\int \frac{\rho_0'\rho_0}{\mid \vec{r} - \vec{r'} \mid} d^3\vec{r'} d^3\vec{r} + E_{xc}[\rho_0] - \int V_{xc}[\rho_0]\rho_0 d^3\vec{r} + V_{nn} \tag{2.27}$$

• E^2 is the second order in the energy with respect to density fluctuation and given by

$$E^2[\delta\rho, \rho_0] = \frac{1}{2}\int\int\left(\frac{1}{\mid \vec{r} - \vec{r'} \mid} + \frac{\delta^2 E_{xc}}{\delta\rho\delta\rho'}\right)\delta\rho\delta\rho' \tag{2.28}$$

2.5.1 Zeroth Order Non-SCC Approach, Standard DFTB

In the standard DFTB scheme, the second-order correction term, E^2 in equation 2.24, is neglected. Therefore, the calculation of the total energy does not depend on the electronic density fluctuations $\delta\rho$ but only on the input density ρ_0. The core-core repulsion, E_{rep} is taken to be a sum of two-body potentials [53], and accordingly, it does not have to be solved iteratively. The total energy becomes;

$$E^0_{\mathrm{DFTB}} = \langle\psi(\vec{r}) \mid H^0[\rho(\vec{r})] \mid \psi(\vec{r})\rangle + E_{rep}[\rho_0] \tag{2.29}$$

In DFTB the Kohn-Sham wave function Ψ_i are expanded as a suitable set of linear combinations of atomic orbitals (LCAO), χ_ν, centred on the nuclei.

$$\psi_i = \sum_\nu C_{\nu i}\chi_\nu(\vec{r} - \vec{R}_\alpha); \tag{2.30}$$

Where, $\mathrm{C}_{\nu i}$ are the expansion coefficients of the wavefunctions consisting of atomic orbitals on the atomic sites α.

This LCAO model leads to the following secular problem;

$$\sum_\nu \mathrm{C}_{\mu\nu}(H^0_{\mu\nu} - \varepsilon_i S_{\mu\nu}) = 0, \qquad \forall\mu, i \tag{2.31}$$

where;

$$H^0_{\mu\nu} = \langle \chi_\mu \mid H^0 \mid \chi_\nu \rangle; \qquad S_{\mu\nu} = \langle \chi_\mu \mid \chi_\nu \rangle \quad \forall \mu \in \alpha, \nu \in \beta. \tag{2.32}$$

The first term of equation 2.29 can be transformed, with equations 2.26 and 2.30, into

$$\begin{aligned} \sum_i^{\text{occ.}} \langle \Psi_i \mid H^0 \mid \Psi_i \rangle &= \sum_i^{\text{occ.}} \sum_{\mu\nu} \mathrm{C}^i_\mu \mathrm{C}^i_\nu \langle \chi_\mu \mid T + V_{eff}[\rho_0] \mid \chi_\nu \rangle \\ &\equiv \sum_i^{\text{occ.}} \sum_{\mu\nu} \mathrm{C}^i_\mu \mathrm{C}^i_\nu H^0_{\mu\nu} \end{aligned} \tag{2.33}$$

The potential can be decomposed into atomic-like contributions as [56];

$$V_{\text{eff}}[\rho_0] = \sum_\alpha V_\alpha(\vec{r_\alpha}) \quad with \quad \vec{r_\alpha} = \vec{r} - \vec{R_\alpha} \tag{2.34}$$

The Hamiltonian $H^0_{\mu\nu}$ can be separated into;

$$H_{\mu\nu} = \langle \chi_\nu \mid \hat{T} + V_\alpha(\vec{r_\alpha}) \mid \chi_\mu \rangle + \sum_{\alpha \neq \beta} \langle \chi_\nu \mid V_\beta(\vec{r_\beta}) \mid \chi_\mu \rangle \quad \mu, \nu \in \{\alpha\} \tag{2.35}$$

and

$$\begin{aligned} H_{\mu\nu} =& \langle \chi_\nu \mid \hat{T} + V_\alpha(\vec{r_\alpha}) + V_\beta(\vec{r_\beta}) \mid \chi_\mu \rangle \\ &+ \sum_{\gamma \neq \alpha, \gamma \neq \beta} \langle \chi_\nu \mid V_\gamma(\vec{r_\gamma}) \mid \chi_\mu \rangle \quad \nu \in \{\alpha\}, \mu \in \{\beta\} \end{aligned} \tag{2.36}$$

where $\{\alpha\}$ denotes the atomic orbitals at α. The orthogonality of the basis functions with respect to the core basis-functions of the remaining atoms should be assured in order to restrict the LCAO to valence orbitals only.[2] The orthogonalized basis function can be written as;

$$\mid \tilde{\chi_\mu}\rangle = \mid \chi_\mu\rangle - \sum_{\beta\neq\alpha}\sum_{c\beta} \mid \chi_c^\beta\rangle\langle\chi_c^\beta \mid \chi_\mu\rangle \qquad \mu \in \{\alpha\} \tag{2.37}$$

where, $\mid \chi\rangle$ is a non-orthogonalized basis-function and $\mid \chi_c^\beta\rangle$ are the core basis-functions of atom β.

By applying this orthogonalization we can make the following modification in equation 2.35;

$$\langle\tilde{\chi_\nu} \mid V_\beta(\vec{r_\beta})\mid \tilde{\chi_\mu}\rangle \Rightarrow \rangle\chi_\mu \mid \left[V(\vec{r_\beta}) - \sum_{c\beta} \mid \chi_c^\beta\rangle\varepsilon_c^\beta\langle\chi_c^\beta \mid\right] \mid \chi_\nu\rangle \quad \alpha \neq \beta \tag{2.38}$$

where ε_c^β is the eigenvalue of the core state c in atom β. Similar expressions can be obtained for the potential contributions in equation 2.35 [57].

The effective potential V_{eff} and the core correction in equation 2.38 can be used as pseudopotentials [56, 57], V_{pp}. Writing V_{eff} as sum of potentials V_l centred on the atoms;

$$V_{eff}[\rho_0] = \sum_{l}^{N_n} V_l(\vec{r_l}) \qquad \vec{r_l} = \vec{r} - \vec{R_l}. \tag{2.39}$$

By substiting equation 2.39 into 2.38, the effective potential becomes a pseudopotential for all atoms except for the atoms on which χ_μ and χ_ν are centred. The

[2] This can be done by using atomic orbitals as basis functions, lead to orthogonality between the core and valence functions within the same atom.

Hamiltonian matrix elements are defined as;

$$H^0_{\mu\nu} = \langle \chi_\mu \mid \hat{T}_\nu + V_\alpha + (1 - \delta_{\alpha\beta})V_\beta \mid \chi_\nu \rangle, \qquad \mu \in \{\alpha\}, \quad \nu \in \{\beta\}. \tag{2.40}$$

where, $\delta_{\alpha\beta}$ is the Kronecker's delta.

The pseudopotential appears in the three-centre terms and in the two-centre terms where valence orbitals belong to the same atom (so called crystal-field terms[3]). The pseudopotential contributions are much smaller than the full potentials contributions, so are neglected [56]. Another method has been presented by Elstner *et al.* [55] to derive DFTB, where the Hamiltonian matrix elements are calculated as a functional of charge density superpositions, which is identical to equation 2.40 except for the contribution of the exchange correlation potential. Due to the nonlinear behaviour of $V_{xc}[\rho]$ we cannot exactly substitute $V_\alpha(\vec{r_\beta}) + V_\beta(\vec{r_\beta}) = V^0_\alpha(\vec{r}_\alpha) + V^0_\beta(\vec{r_\beta})$, so, instead write:

$$V_\alpha(\vec{r_\alpha}) + V_\beta(\vec{r_\beta}) = V[\rho^0_\alpha + \rho^0_\beta]$$

This means the atomic densities have been used for calculating the potential contribution. and the Hamiltonian matrix elements $H^0_{\mu\nu}$ can be written as;

$$H^0_{\mu\nu} = \langle \chi_\mu \mid \hat{T} + V_{eff}[\rho^0_\alpha + \rho^0_\beta] \mid \chi_\nu \rangle, \quad \mu \in \{\alpha\}, \nu \in \{\beta\} \tag{2.41}$$

[3]This case occurs, when the basis-functions both come from the same atomic site, but the potential is on a different site. This category shares features with both the two-centre and three-centre integrals but is actually a local environment or crystal field correction to the on-site terms [58].
The crystal-field terms are normally omitted, except when charge transfer is significant, in which case they have a Coulomb-like 1/R dependence [59] which is short ranged.

Within the density superposition approach the Hamiltonian $H^0_{\mu\nu}$ is written as;

$$H^0_{\mu\nu} = \begin{cases} \epsilon_\mu^{\text{for free atom}}, & \mu = \nu. \\ \langle \chi_\mu \mid \hat{T} + V_{eff}[\rho^0_\alpha + \rho^0_\beta] \mid \chi_\nu \rangle, & \mu \in \{\alpha\}, \nu \in \{\beta\} \\ 0 & \text{otherwise.} \end{cases} \tag{2.42}$$

i.e. a two-centre Hamiltonian that reduces to atomic states in the limit of dissociation. In both approaches the equations (2.40 and 2.41) have similar results, with the potential superposition being more popular for standard DFTB calculations, and the density superposition more widely used for SCC-DFTB [57]. The χ_ν basis functions and the reference atom-like densities ρ^α_0 are obtained by solving an atomic Schrödinger equation:

$$\left[\hat{T} + V_{\text{eff}}[\rho^\alpha_0] + \left(\frac{r}{r_0}\right)^2\right] \chi_\nu(\vec{r}) = \varepsilon_\nu \chi_\nu(\vec{r}) \tag{2.43}$$

2.5.2 Second-Order Self Consistent Charge, SCC-DFTB

In order to include charge density fluctuations, $\delta\rho$ is decomposed into the superposition of atom-like contributions, $\delta\rho_\alpha$, which decay rapidly as the distance from the corresponding atomic centre increases.

$$\delta\rho = \sum_{\alpha}^{N_n} \delta\rho_\alpha \tag{2.44}$$

The second order term of equation 2.28 then becomes;

$$E^2[\rho,\rho_0] = \frac{1}{2}\sum_{\alpha\beta}\int\int'\left(\frac{1}{\mid \vec{r}-\vec{r'} \mid} + \frac{\delta^2 E_{xc}[\rho]}{\delta\rho\delta\rho'}\right)\delta\rho_\alpha(\vec{r})\delta\rho_\beta(\vec{r'}) \tag{2.45}$$

The $\delta\rho_\alpha$ are expanded in a series of radial and angular functions. This is simplified by a monopole approximation;

$$\delta\rho_\alpha(\vec{r}) = \sum_{lm} K_{ml}F^\alpha_{ml}(\mid \vec{r}-\vec{R}_\alpha \mid)Y_{lm}\left(\frac{\vec{r}-\vec{R}_\alpha}{\mid \vec{r}-\vec{R}_\alpha \mid}\right) \approx \triangle q_\alpha F^\alpha_{00}(\mid \vec{r}-\vec{R}_\alpha \mid)Y_{00} \tag{2.46}$$

where $\triangle q_\alpha$, is the fluctuation Mulliken charge (the difference between the atomic Mulliken population q_α (see equation 2.60) and the number of valence electrons of the neutral free atom $q^0_\alpha : \triangle q = q_\alpha - q^0_\alpha$). F^α_{00} is normalized radial dependence of the density fluctuation in atom α, approximated as spherical by the angular function Y_{00}.

By substituting equation 2.46 into 2.28, the final expression for the second order energy term becomes;

$$E^2 = \frac{1}{2}\sum_{\alpha\beta}^{N_n} \triangle q_\alpha \triangle q_\beta \gamma_{\alpha\beta} \qquad \text{where} \quad \underbrace{\sum_\alpha \triangle q_\alpha = \int \delta\rho(\vec{r})d^3\vec{r}}_{\text{the total charge in the system}} \tag{2.47}$$

with;

$$\gamma_{\alpha\beta} = \int\int' \Gamma[\vec{r},\vec{r'},\rho_0]\frac{F_{00}^{\alpha}(\mid \vec{r}-\vec{R}_{\alpha}\mid)F_{00}^{\beta}(\mid \vec{r'}-\vec{R}_{\beta}\mid)}{4\pi}d^3\vec{r'}d^3\vec{r} \tag{2.48}$$

In order to obtain useful expression, Slater type orbitals are used as a basis set to solve the Kohn-Sham like equations (2.30). Then, assuming an exponential decay of the normalized spherical charge density with spread $\propto\ \tau$ [54];

$$\rho_{\alpha}(\vec{r}) = \frac{\tau_{\alpha}^3}{8\pi}exp\left(-\tau_{\alpha}\mid \vec{r}-\vec{R}_{\alpha}\mid\right) \tag{2.49}$$

and neglecting the second order contribution of E_{xc} in equation 2.45, $\gamma_{\alpha\beta}$ becomes;

$$\gamma_{\alpha\beta} = \int\int' \frac{1}{\mid \vec{r}-\vec{r'}\mid}\frac{\tau_{\alpha}^3}{8\pi}e^{-\tau_{\alpha}|\vec{r'}-\vec{R}_{\alpha}|}\ \frac{\tau_{\beta}^3}{8\pi}e^{-\tau_{\beta}|\vec{r}-\vec{R}_{\beta}|}d^3\vec{r'}d^3\vec{r} \tag{2.50}$$

After integrating over r' we get;

$$\gamma_{\alpha\beta} = \int\left[\frac{1}{\mid \vec{r}-\vec{R}_{\alpha}\mid} - \left(\frac{\tau_{\alpha}}{2}+\frac{1}{\mid \vec{r}-\vec{R}_{\alpha}\mid}\right)e^{-\tau_{\alpha}|\vec{r}-\vec{R}_{\alpha}|}\right]\frac{\tau_{\beta}^3}{8\pi}e^{-\tau_{\beta}|\vec{r}-\vec{R}_{\beta}|} \tag{2.51}$$

By putting $R = \mid \vec{R}_{\alpha}-\vec{R}_{\beta}\mid$, and after some coordinate transformations, γ becomes [54].

$$\gamma_{\alpha\beta} = \frac{1}{\vec{R}} - S(\tau_{\alpha},\tau_{\beta},R) \tag{2.52}$$

where S is a short-range function with exponential decay, having limiting values of;

$$\lim_{R\to 0} S(\tau_\alpha, \tau_\beta, R) = \frac{5}{16}\tau_\alpha + \frac{1}{R} \tag{2.53}$$

when the interatomic distance goes to zero ($R \to 0$), $\gamma_{\alpha\beta} \to \gamma_{\alpha\alpha}$ describes the electron-electron interaction within the atom α, and is related to the chemical hardness η_α or Hubbard parameter U_α by [57];

$$\gamma_{\alpha\alpha} = 2\eta_\alpha = U_\alpha \tag{2.54}$$

where the atomic hardness can be calculated as the difference between ionization potential I_α and electron affinity A_α of atom α;

$$\eta_\alpha = \frac{I_\alpha - A_\alpha}{2} \tag{2.55}$$

U_α can be calculated for any atom type within DFT as the second derivative of the total energy of atom type α with respect to the atomic charge.

In this approximation, the influence of the enviroment on the intra-atomic electron-electron interaction, represented by U_α, is neglected. The second derivative with respect to the atomic charge may be rewritten as a first derivative with respect to the atomic occupation number [54, 57]:

$$U_\alpha = \eta_\alpha = \frac{\delta\varepsilon_{\text{homo}}}{\delta n_{\text{homo}}} \Rightarrow \frac{1}{2}U_\alpha \triangle q_\alpha^2 \tag{2.56}$$

So, E^2 can be written as function in U_α as [57]

$$E^2[\rho, \rho_0] \approx \frac{1}{2}\frac{\delta^2 E[\rho_0]}{\delta^2 q_\alpha} \triangle q_\alpha^2 = \frac{1}{2} U_\alpha \triangle q_\alpha^2 \tag{2.57}$$

According to equation 2.57 and 2.53 we can write τ_α as [54, 57];

$$\tau_\alpha = \frac{16}{5} U_\alpha \tag{2.58}$$

The total energy within SCC–DFTB is then written as;

$$E^2_{\mathrm{DFTB}} = \sum_i^{N_e} \langle \psi_i \mid H^0 \mid \psi_i \rangle + \frac{1}{2} \sum_{\alpha,\beta}^{N_n} \gamma_{\alpha\beta} \triangle q_\alpha \triangle q_\beta + E_{rep} \tag{2.59}$$

where $\gamma_{\alpha\beta} = \gamma_{\alpha\beta}(U_\alpha, U_\beta, R)$, and the Hamiltonian H^0 is exactly the same as in the standard DFTB equation 2.25.

Here again the Kohn-Sham like wave functions ψ_i are expanded as atomic orbitals, as in equation 2.30.

The charge fluctuations are calculated by using Mulliken charge analysis [54];

$$q_\alpha = \frac{1}{2} \sum_i^{occ} \rho_i \sum_{\mu\in\alpha}^{N_n} \sum_\nu^{N_n} \left(C^*_{\mu i} C_{\nu i} S_{\mu\nu} + C^*_{\nu i} C_{\mu i} S_{\nu\mu} \right) \tag{2.60}$$

By applying the variational principle to 2.59, the Hamilton matrix elements become;

$$\begin{aligned} H_{\mu\nu} =& \langle \chi_\mu \mid H^0 \mid \chi_\nu \rangle + \frac{1}{2} S_{\mu\nu} \sum_l^{N_n} (\gamma_{\alpha l} + \gamma_{\beta l}) \triangle q_l \\ =& H^0_{\mu\nu} + H^1_{\mu\nu} \quad \forall\, \mu \in \alpha, \nu \in \beta. \end{aligned} \tag{2.61}$$

2.5.3 Spin-Orbit Coupling

Taking spin interaction into account leads to double the number of energy levels, $\varepsilon(k)$, because each k state can then be occupied twice. For atoms with large enough atomic numbers (greater than thirty [60]) the Russell-Saunders description of atomic states becomes appropriate due to relativistic corrections to the Schrödinger equation. Scalar relativistic effects can be included in the atomic calculations of ε_μ (equations 2.42 and 2.43) but to include spin orbit interactions, the Hamiltonian should supplemented with a spin-orbit coupling term [61];

$$O_s = \frac{\hbar^2}{4im^2c^2}(\bigtriangledown V \times \bigtriangledown) \cdot \sigma \tag{2.62}$$

where O_s operates on spinors $\psi(\vec{r}, s)$, with the gradient in the parentheses operating on the space component and the spin operator σ on the spin component.

$$\psi(\vec{r}, s) = \begin{vmatrix} \psi_\uparrow(\vec{r}) \\ \psi_\downarrow(\vec{r}) \end{vmatrix} \tag{2.63}$$

where $\psi_\uparrow(\vec{r})$ and $\psi_\downarrow(\vec{r})$ are Pauli two component wavefunctions (spin up and spin down respectively), σ are Pauli's matrices and given by;

$$\sigma_x = \begin{pmatrix} 0 & 1 \\ 1 & 0 \end{pmatrix}, \qquad \sigma_y = \begin{pmatrix} 0 & -i \\ i & 0 \end{pmatrix}, \qquad \sigma_z = \begin{pmatrix} 1 & 0 \\ 0 & -1 \end{pmatrix} \tag{2.64}$$

The wavefunction then takes the form of equation 2.63. The spin-orbit contribution to the tight binding Hamiltonian is given by[62].

$$H_{so} = \xi(r)\vec{L}.\vec{\sigma} \quad \equiv \quad \frac{\hbar^2}{4m^2c^2}(\bigtriangledown V \times \vec{p}) \cdot \sigma \tag{2.65}$$

where p and σ are the momentum and spin operators of the electron in the electric potential V and $\xi(r) = \frac{1}{2m^2c^2}\frac{dV}{dr}$. For the central field approximation ($V(\vec{r}) = V(r)$) we can write H_{so} as [63];

$$H_{so} = \xi(r)\vec{L}.\vec{\sigma} = \xi(r)\left[\frac{L_+\sigma_- + L_-\sigma_+}{2} + L_z\sigma_z\right] \tag{2.66}$$

and the general form of tight-binding Hamiltonians become;

$$H_{TB} = \frac{p^2}{2m} + \sum_i V(\vec{r_i} - \vec{R_i}) + \sum_i \xi(\vec{r_i} - \vec{R_i})\vec{L}.\vec{\sigma} \tag{2.67}$$

where the sum is over all lattice sites R_j. This final term can similarly be added to equation 2.61.

2.6 Periodic Boundary Conditions

In order to deal with periodic systems such as a crystal, we can work directly with the wave functions by using Bloch's theorem [64], where the wavefunction of an electron in periodic potential $V(\vec{r}) = V(\vec{r} + \vec{R})$ can be written as the product of

functions with the same periodicity of the potential and phase term;

$$\psi_k(r) = e^{i.\vec{k}.\vec{r}} u_k(\vec{r}) \tag{2.68}$$

where $\vec{k}$ is a wave vector, $u_k(\vec{r}) = u_k(\vec{r} + \vec{R})$ and $\vec{R}$ is a lattice translations vector and written as;

$$\vec{R} = n_1\vec{a}_1 + n_2\vec{a}_2 + n_3\vec{a}_3 \tag{2.69}$$

where n, an real integer number and $\vec{a}_i$ are the lattice vectors defined by the symmetry of the crystal. The reciprocal lattice vectors are [65];

$$\begin{aligned} \vec{b}_1 &= 2\pi \frac{\vec{a}_2 \times \vec{a}_3}{\Omega} \\ \vec{b}_2 &= 2\pi \frac{\vec{a}_3 \times \vec{a}_1}{\Omega} \\ \vec{b}_3 &= 2\pi \frac{\vec{a}_1 \times \vec{a}_2}{\Omega} \end{aligned} \tag{2.70}$$

where Ω is the cell volume and a_i and b_i are orthogonal ($a_i.b_j = \delta_{ij}$).

As Bloch waves extend throughout the whole crystal, the basis functions 2.15 can be written as [66]

$$\phi_i(\vec{k}, \vec{r}) = \frac{1}{\sqrt{N}} \sum_R e^{i.\vec{k}.\vec{R}} \phi_i(\vec{r} - \vec{R}) \tag{2.71}$$

where N is a number of unit cells in the crystal, and then the eigenfunctions become;

$$\psi(\vec{k}, \vec{r}) = \sum_i C_i \phi_i(\vec{k}, \vec{r}) \tag{2.72}$$

that means that the charge density follows the periodicity as the wavefunction i.e. $\rho(\vec{r}) = \rho(\vec{r} - \vec{R})$. The expression for the electric charge density becomes;

$$\rho(\vec{r}) = \int_{k\epsilon BZ} \omega_k \left|\psi_k(\vec{r})\right|^2 \tag{2.73}$$

Where the integral is over all $\vec{k}$-vectors in the Brillouin zone of the unit cell and ω_k are weight factors that depend on the symmetry of the unit cell.

Also we can find the density of states (DOS), $D(\omega)$ (the number of electronic states per unit volume with an energy E) by applying the periodic boundary condition over N^3 primitive cells within a cube of side L, so that $\vec{k}$ is determined by the condition;

$$e^{i.(k_x x + k_y y + k_z z)} \equiv e^{i.(k_x (x+L) + k_y y + k_z z)} \equiv e^{i.(k_x x + k_y (y+L) + k_z z)} \equiv e^{i.(k_x x + k_y y + k_z (z+L))} \tag{2.74}$$

So, the allowed values of $\vec{k}$ are;

$$\vec{k}_x, \vec{k}_y, \vec{k}_z = 0, \pm\frac{2\pi}{L}, \pm\frac{4\pi}{L}, \ldots, \pm\frac{N\pi}{L} \tag{2.75}$$

Therefore there is one allowed value of $\vec{k}$ per volume $(2\pi/L)$ in momentum space. The total number of modes with wavevector is $(L/2\pi)^3$ times the volume of sphere of radius k [40];

$$N = \frac{L}{(2\pi)^3}\frac{4\pi k^3}{3} \tag{2.76}$$

Thus, the density of state can be written as [40];

$$D(\omega) = \frac{N}{d\omega} = \frac{L^3 k^2}{2\pi^2} \frac{dk}{d\omega} \tag{2.77}$$

In this work the calculation has been done by using Monkhorst and Pack sampling scheme [67], where the special k-point are grid of $I \times J \times K$ points in reciprocal space given by;

$$\vec{k}_{ijk} = u_i \vec{b}_1 + u_j \vec{b}_2 + u_k \vec{b}_3 \tag{2.78}$$

where $\vec{b}_1, \vec{b}_2$ and $\vec{b}_3$ are the reciprocal space lattice unit vectors and u_i, u_j and u_3 are given by;

$$\begin{aligned} u_i &= \tfrac{(2i-I-1)}{2I} \\ u_j &= \tfrac{(2j-J-1)}{2J} \\ u_k &= \tfrac{(2k-K-1)}{2k} \end{aligned} \tag{2.79}$$

where I, J and $K \geq 1$. The energies are then broadened to to convert the discrete energies at the sampled K-point into a continuous DOS, in this work a Gaussian with a standard deviation of 0.1 eV is used for the broadening.

2.7 Geometry Optimization

The geometry optimization is usually a first step in the calculation, where the total energy is minimized in order to find equilibrium structures of system. In this thesis the conjugate gradients (CG) method has been used for optimizing

geometry where, using the conjugate gradients method enable to calculate a local minimum of an arbitrary smooth function depending on a number of variables [68]. In the CG we need the steepest descent direction for initial configuration d_1 and calculate the gradient for the potential energy for this geometry g_1. The gradient vector defines the direction in which the potential energy is changing most rapidly in the region of d_1 [69]. So, the search taking step along the vector $d_1 - \lambda g_1$ in $-g_1$ direction where the length of step is given by λ, if the energy decreases at first step and then for other steps, increases λ until the energy starts to increases. At this point the step size is reduced and the search continued until the minimum energy in this direction is found. Then when minimum energy is found in the position $d_1 - \alpha g_1$ (where α is the value of λ at the minimum) moves to configuration $d_2 = d_1 - \lambda g_1$ and repeats the procedure for the vector $d_2 - \lambda g_2$. Then the search is made along direction $d_3 = -g_2 + \beta d_2$ where β is given by $\beta = |g_2|^2 / |g_1|^2$ (in Fletcher -Reevesmethod) or $\beta = (g_2 - g_1)g_2 / |g_1|^2$ (in Polak-Ribiere method). Thus the direction of search d_2 is not along the direction $-g_2$ but along a direction which is a linear combination of the new gradient g_2 and the previous direction of search d_1. In general we can write d_k as [69];

$$d_k = -g_k + \beta d_{k+1} \tag{2.80}$$

where β is

$$\beta = \frac{|g_k|^2}{|g_{k-1}|^2} \qquad (\text{Fletcher} - \text{Reeves} \quad \text{method}) \tag{2.81}$$

or

$$\beta = \frac{(g_k - g_{k-1})g_k}{|g_{k-1}|^2} \qquad (\text{Polak} - \text{Ribiere} \quad \text{method}) \tag{2.82}$$

Chapter 3

Results for Bulk InN and GaN

3.1 Introduction

The group III-nitride compounds AlN, GaN, InN and their alloys such as InGaN and AlGaN have in the last few years received a lot of attention due to their possible applications in optoelectronic devices. E.g. GaN based semiconductors have applications not only to light sources of short wavelength, but also high-speed and high-power electron devices [70]. This chapter will focus particularly on GaN and InN. The major advantage for these materials is their direct energy gap (E_g), which leads to high efficiency in optoelectronic devices. GaN as a wide band gap material, where the value of its energy gap (WZ-GaN) is around $\sim$3.4 eV [6]. Previous research indicated that the value of the energy gap of WZ-indium nitride is about 1.9 eV [25], But, a smaller value ($<$ 1 eV) of energy gap became accepted for WZ-InN, measured and calculated by Ref [28, 31, 71] and Ref [72] respectively. Thus, now InN is considered to be narrow band gap material on energy gap value

of <0.7 eV [20]. Other accepted values of properties such as lattice constants, effective masses and elastic constants, will be presented in comparison with results of this work later in this chapter.

3.2 Band Structure

The calculated single particle band structures for the primitive unit cells of wurtzite and zincblende GaN and InN are shown in Figure 3.1. These results use the DFTB+ [73] code, which self-consistently solves equation 2.24. The parameters for GaN are based on Ref. [74], while the InN parameters are based on unpublished parameters, of Dr. Simone Sanna, University of Paderborn. These parametrization has been developed for (In,Ga)N using the density functional based tight binding method (DFTB). The on-site energy terms in the parameterization are empirically adjusted to reproduce the band gaps of InN and GaN accurately, i.e. the band gaps of InN and GaN have been corrected to reproduce experiment by adjusting the energy of nitrogen-2s state, 5s, 5p, 4d states for indium and 4s, 4p, and 3d states for gallium. While the repulsive energy is chosen to decay exponentially to re-produce the lattice constants of the WZ polytype. The performance of this method has been demonstrated by calculating a range of properties for the two materials, including elastic constants and carrier effective masses. Converged self-consistency and k-point sampling [67] ($12 \times 12 \times 12$ points used to integrate equation 2.24 over the first Brillouin zone) are applied (self consistency to a maximum differences of 10^{-10} electron charges between input and output Mulliken charges is obtained).

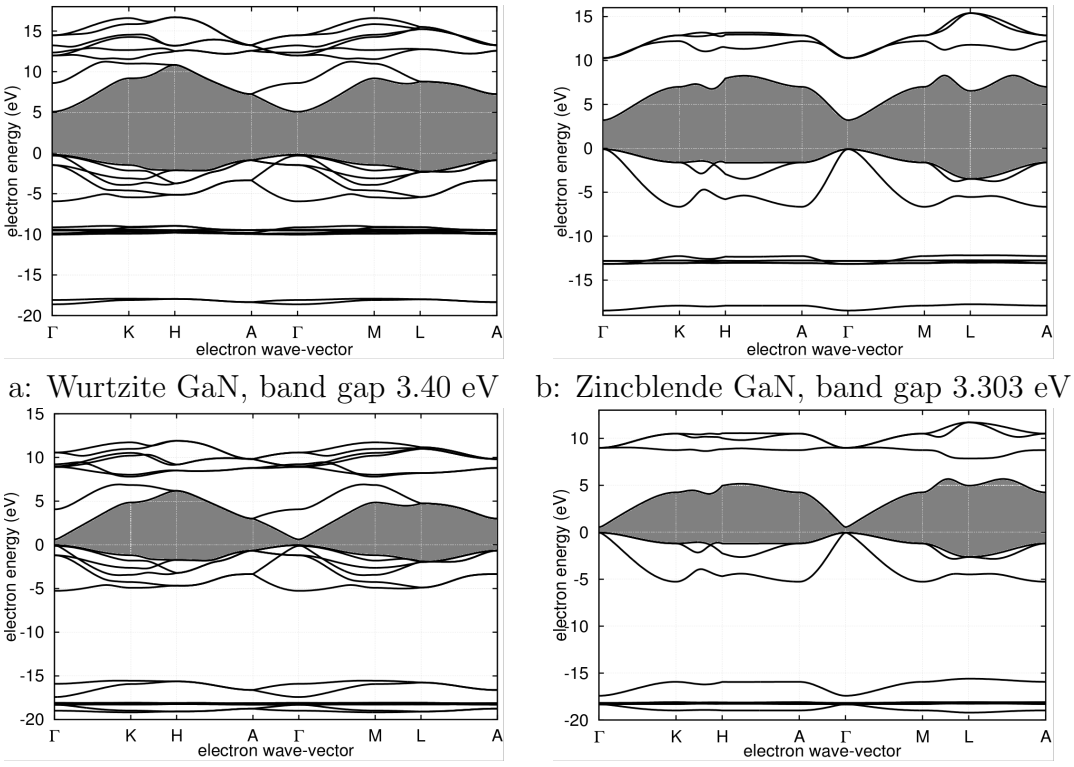

a: Wurtzite GaN, band gap 3.40 eV b: Zincblende GaN, band gap 3.303 eV

c: Wurtzite InN, band gap 0.68 eV d: Zincblende InN, band gap 0.591 eV

FIGURE 3.1: The band structure of WZ and ZB InN and GaN, with the energy shifted so that the uppermost valence band is at zero and the forbidden band gap area labelled as grey colour. This also shows a second band gap between the valence and deeper d-state bands.

3.3 Energy Gap and Lattice Constants

Figure 3.1-a and 3.1-c show single particle band structures for the primitive unit cells of wurtzite GaN and InN. The minimum energy (relaxed) lattice constants for these parameters are $a^{\mathrm{GaN}} = 3.191$ Å, $c^{\mathrm{GaN}} = 5.233$ Å, $a^{\mathrm{InN}} = 3.544$ Å and $c^{\mathrm{InN}} = 5.786$ Å. These values are compared with experimental values in table 3.1. The deviation from the experimental values found to be, for GaN 0.06% for a and 0.93 % for c respectively compared to current accepted value (e.g. Ref. [75], where a and c valuse are given to a precision of $< 5{\times}10^{-5}$ Å). In the InN case a lattice constant found to be 0.10 % smaller while the value of c is 1.36 % larger. The band gap value obtained for wurtzite InN is 0.68 eV and for GaN 3.40 eV, again close to

	a^{WZ}	c^{WZ}	a_0^{ZB}		a^{WZ}	c^{WZ}	a_0^{ZB}
GaN				InN			
This work	3.191	5.233	4.520	This work	3.544	5.786	5.01
Experimental				Experimental			
[21]	3.189	5.185	4.50	[21]	3.545	5.703	4.98
[75]	3.189	5.185	4.531 [76]	[77]	3.545	5.703	4.98
[78]	3.188	5.185	4.501 [79]				
Calculated				Calculated			
[80]	3.20	5.22	4.55 [81]	[72]	3.523	5.688	4.967
[82]	3.181	5.166	4.50	[80]	3.48	5.64	4.96 [81]
[20]	3.158	5.145	4.465	[82]	3.533	5.693	4.98
				[20]	3.517	5.685	4.959

TABLE 3.1: The lattice constants for wurtzite (and zincblende) GaN and InN (Å) compared with experimental and calculated data from the literature references given in brackets

	GaN	Method	InN	Method
WZ				
This work	3.40	DFTB	0.68	DFTB
	3.474 [83]	AB	2.050 [84]	AB
	3.503 [85]	PL	1.890 [25]	AB
	3.390 [86]	AB	0.71.0 [87]	PL
	3.503 [88]	PL	0.690 [71]	PL
	3.41 [22]	PL	0.685 [29]	PL
	3.847 [20]	DFT-LDA	0.765 [20]	DFT-LDA
ZB				
This work	3.303	DFTB	0.591	DFTB
	3.350 [89]	PL	1.94 [90]	CED
	3.302 [91]	PL	0.560 [26]	PL
	3.270 [92]	PL	0.636 [93]	PL
	3.609 [20]	DFT-LDA	0.540 [20]	DFT-LDA

TABLE 3.2: The Energy gap (E_g)values in (eV) for wurtzite and zincblende GaN and InN compared with experimental data and theoretical calculations references in brackets.

AB: Absorption
CED: Collection of Experimental Data
DFT-LDA: Density Functional Theory-Local Density Approximation

the accepted values (see table 3.2). Figure 3.1-b and 3.1-d show the single particle band structures for the primitive unit cells of zincblende GaN and InN. The direct band gap value obtained for InN is 0.59 eV and for GaN 3.30 eV (Table 3.2). The lattice constants for the zincblende polytype are found to be $a_0^{\mathrm{GaN}} = 4.52$ Å which is close to experimental values, being 0.21 % larger than the average value of the experimental data of table 3.1. $a_0^{\mathrm{InN}} = 5.01$ Å is 0.60 % larger compared to experimental results for Ref [21] and Ref [77] (at room temperature, table 3.1).

3.4 Effective Masses

Table 3.3 shown the effective masses of wurtzite GaN and InN for electrons, heavy and light holes and the crystal field split-off holes[1] along the Γ-A (parallel to c direction and labelled as ${}^{\|}m^{\star}$) line and average[2] values over the Γ-K and Γ-M directions (the perpendicular to directions c and labelled as ${}^{\perp}m^{\star}$) in units of m_0. The uncertainty is estimated by varying the size of the numerical step used in calculating the effective masses, giving a limition the error in the masses. The typical variation was $\sim \pm 6\times10^{-3}$ m_0 was found on average, however in the case of the light holes, a substantial error of $\pm$ 0.5 m_0 was found. The spin-orbit constants used in this calculation are taken from Ref. [94]. The effective mass value are calculated by using equation 3.1. A very small range[3] in the in Brillouin

[1] The holes effective mass of the bands which split due to crystal field which produced from a static electric field produced by a surrounding charge distribution (anion neighbors) [40].

[2] The averaging is made to compare against values in the literature where the mass is assumed to be isotropic in this plane.

[3] The ranges used for calculations along the high symmetry directions in the BZ are: 2.8×10^{-3}, 4.9×10^{-3} and 3.4×10^{-3} of the paths Γ-X, Γ-K/U and Γ-L respectively for the zincblende and 1.0×10^{-2}, 1.4×10^{-2} and 1.0×10^{-2} of the paths Γ-A, Γ-K and Γ-M respectively for wurtzite.

zone close to Γ was used, as the use of a large number of k points outside the range leads to obtaining incorrect values for the effective mass, because the dispersion curve away from the Γ point becomes nonparabolic and in this case equation 3.1 is no longer suitable for the calculation.

$$\frac{1}{m^*} = \frac{1}{\hbar^2}\frac{d^2\varepsilon}{dk^2} \tag{3.1}$$

	$^{\parallel}m_e^\star$	$^{\parallel}m_{hh}^\star$	$^{\parallel}m_{lh}^\star$	$^{\parallel}m_{ch}^\star$	$^{\perp}m_e^\star$	$^{\perp}m_{hh}^\star$	$^{\perp}m_{lh}^\star$	$^{\perp}m_{ch}^\star$
WZ-GaN								
This work	0.244	1.09	0.732	0.200	0.311	0.373	0.300	0.341
Ref [95]	0.19	1.76	1.76	0.14	0.17	1.69	0.14	1.76
Ref [20]	0.21	2.00	1.22	0.20	0.21	0.57	0.31	0.92
Ref [96]	0.35	2.00	1.19	0.17	0.35	0.34	0.35	1.27
Ref [97]	0.20	1.85	0.55	0.20	0.22	0.69	0.50	0.80
Ref [38]	...	1.76	0.419	0.299	...	0.349	0.512	0.676
Ref [21]^{exp}	0.20	...	...	...	0.20	...	...	...
WZ-InN								
This work	0.086	1.797	0.180	0.120	0.105	0.142	0.232	0.21
Ref [20]	0.06	1.98	1.02	0.08	0.06	0.44	0.09	0.18
Ref [95]	0.11	1.56	1.56	0.10	0.10	1.68	0.11	1.39
Ref [97]	0.09	2.00	1.86	0.06	0.09	0.15	0.14	1.26
Ref [21]^{exp}	0.07	...	...	...	0.07	...	...	...

TABLE 3.3: The Γ-A and average Γ-K and Γ-M directions, the effective masses values for wurtzite GaN and InN for electrons, heavy and light holes and the crystal field split-off holes in units of m_0.

Note: The experimental values for hole effective masses are rare in literature, only reference [38] estimates values for GaN based on experimental data, while experimentally derived values for InN seems to be unavailable.

The results shown for the Γ-A direction for InN are acceptable for electron and heavy hole effective masses, where the deviation from literature values are found to be between 4 % larger and 3 % smaller respectively, than the results of other

references (shown in table 3.3). A larger deviation is found for light hole mass, of about 88 % smaller, and for the crystal split-off mass which is 50 % larger as compared with the average of the data of the references shown in table 3.3. This fluctuation in effective masses values could be due to the parameter set used in this calculation: the atomic calculations used to create these parameters does not include spin-orbit coupling, so for example different J states can be artificially degenerate and this may be the origin of the discrepancy in the masses. For GaN along the same direction, the values for electron and crystal split-off mass are acceptable and very close to Ref. [20] $\sim$ 14 % and 0 % respectively, but values for light and heavy holes are rather small compared with other results, e. g. heavy and light holes are $\sim$ 45.5 % and $\sim$ 40.0 % smaller compared to Ref [20]. Table 3.3 shows the average effective mass values along the Γ-K and Γ-M directions, the values shown in this table are the average over the Γ-K and Γ-M directions. The results for GaN electrons masses are reasonably accurate when compared with Ref. [96], where the deviation found to be only about 11 % smaller, while light and heavy and crystal field split-off hole masses are rather small compared with some results, but those of Refs. [96] and [97] are in a good agreement with these results, for the light and heavy holes. For InN, the values of light holes are larger compared with the literature results while the heavy hole masses are smaller, here the crystal field split-off holes are in a good agreement with Ref [20]. Again the electron effective masses have acceptable values compared with other references. DFTB is usually considered to be more accurate for valence band states, due to its minimal basis [56] and [98].

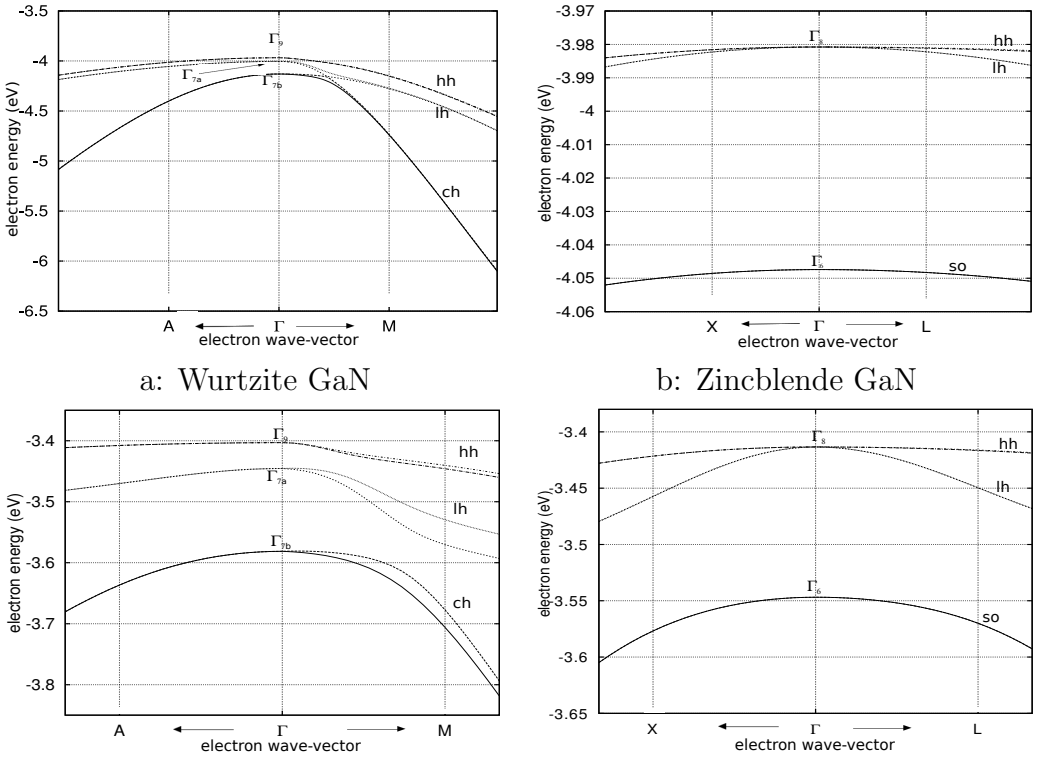

a: Wurtzite GaN b: Zincblende GaN

c: Wurtzite InN d: Zincblende InN

FIGURE 3.2: The uppermost valence bands of WZ and ZB InN and GaN, the WZ data are shown along two high symmetry directions in the Brillouin zone, Γ-A and Γ-M and the ZB dispersion is shown along Γ-X and Γ-L.

Table 3.4 shows the effective mass results for zincblende GaN and InN along the [100], [110] and [111] directions from the Γ point. The electron and spin orbit split-off masses are large compared to other calculated and experimental values, while light holes for all directions have acceptable values compared to other calculated values in this table, but the values of heavy holes have smaller values for all directions compared to other calculated data in the table with maximum difference of about 34 % smaller than the average heavy holes data used in table 3.4 along the [110] directions for GaN, while the maximum difference for InN is found along the [100] direction, with the best agreement found for the [111] direction. This volatility in the results likely due to the parameters used in the calculations and the choice of atomic spin orbit splitting energy values. As shown in Fig 3.2 the

splitting between curves can hardly be seen, as compared to Figures shown in Ref [20]. In general these parameters agree better for InN than GaN.

	$m_{hh}^{[100]}$	$m_{lh}^{[100]}$	$m_{hh}^{[110]}$	$m_{lh}^{[110]}$	$m_{hh}^{[111]}$	$m_{lh}^{[111]}$	$m_{so}^{\star}$	$m_{e}^{\star}$
ZB-GaN								
This work	0.590	0.309	1.022	0.257	1.399	0.246	0.411	0.275
Ref [20]	0.83	0.28	1.59	0.25	1.95	0.23	0.34	0.19
Ref [99]	0.86	0.21	1.65	0.19	2.09	0.19	0.30	0.14
Ref [27]	0.81	0.265	1.38	0.23	1.81	0.22	...	0.19
Ref [21]^{exp}	...	...	...	...	...	...	...	0.15
ZB-InN								
This work	0.662	0.098	1.135	0.093	1.705	0.091	0.208	0.074
Ref [20]	0.91	0.079	1.55	0.065	1.89	0.07	0.11	0.052
Ref [27]	0.835	0.08	1.368	0.078	1.738	0.077	...	0.054
Ref [21]^{exp}	...	...	...	...	...	...	...	0.07
Ref [100]^{exp}	...	...	...	...	...	...	...	0.041

TABLE 3.4: The effective masses of zincblende GaN and InN for electrons, heavy and light holes and the crystal field split-off holes in units of free electron mass m_0. The heavy and light holes masses along the [100], [110], and [111] directions compared with other calculated and experimental results.

3.5 Density of States

Figure 3.3, shows the total and partial density of state for (a) WZ-GaN and (b) WZ-InN for the minimal basis set used in DFTB (this leads to the upper cut-off in the energy shown for conduction band states). In the valence band, we found in both cases that, the major contribution in total DOS comes from nitrogen-2p then gallium/indium-4/5p, then lesser contribution from gallium/indium 4/5-s, then nitrogen-s and finally gallium/indium-3/4d. While in the conduction band near the band gap, gallium/indium-s has a major contribution, then gallium/indium-4/5p, and then other states. Figure 3.4, shows the total and partial density of state

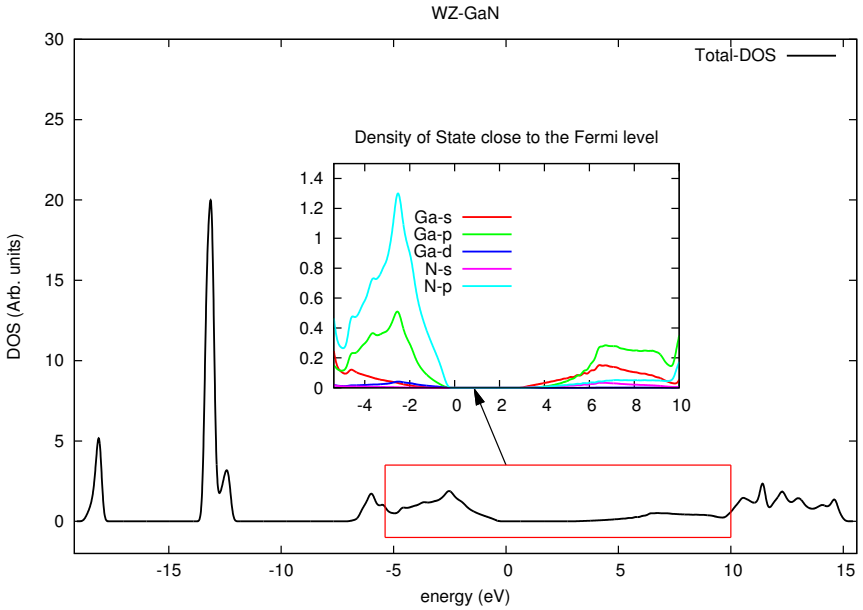

a: Wurtzite GaN, DOS

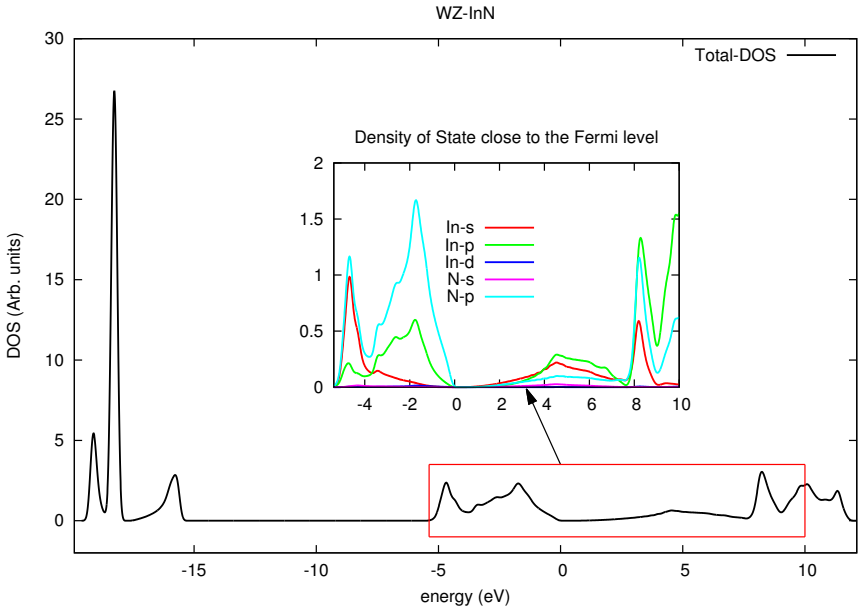

b: Wurtzite InN, DOS

FIGURE 3.3: The electron density of states for (a) WZ-GaN and (b) WZ-InN. The region close to the valence conduction band extrema are shown inset (with the energy shifted such that the uppermost valence band is at zero).

for (a) ZB-GaN and (b) ZB-InN, as seen in inset figures. There are no differences in the relative contributions of s, p, and d states for indium and gallium, and s/p states for nitrogen, between zincblende and wurtzite.

Figures 3.5 and 3.6 shown the density of states for each type of atom (i.e. Ga, In,

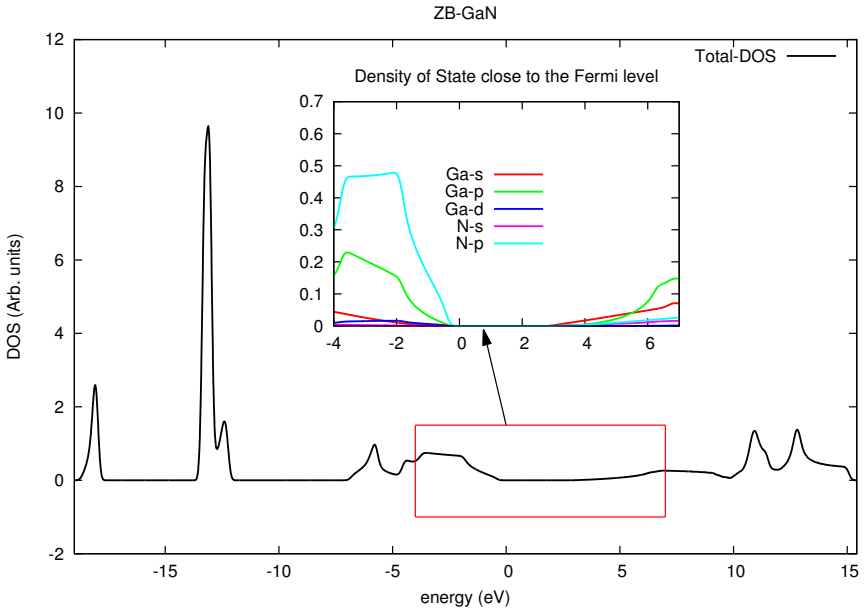

a: Zincblende GaN, DOS

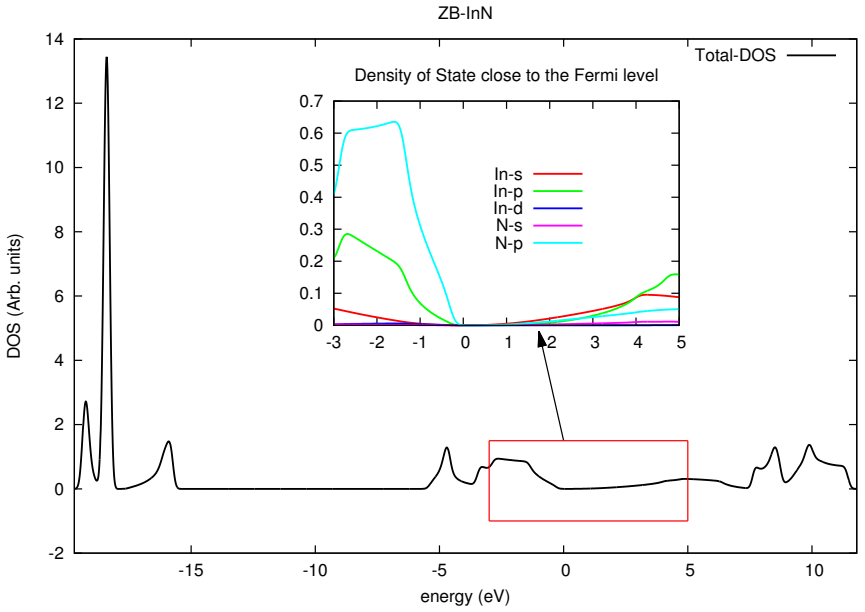

b: Zincblende InN, DOS

FIGURE 3.4: The electron density of state for (a) ZB-GaN and (b) ZB-InN. The region close to the valence conduction band extrema are shown inset (with the energy shifted such that the uppermost valence band is at zero).

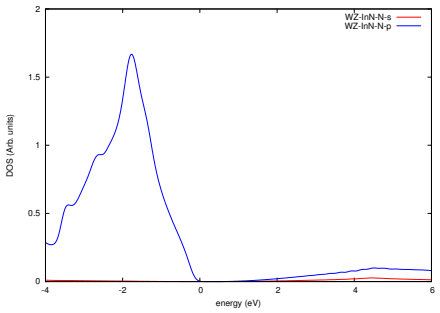

a: N in Wurtzite InN, DOS

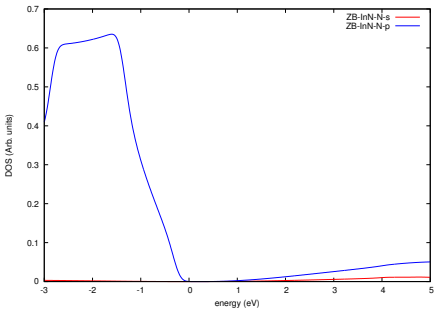

b: N in Zincblende InN, DOS

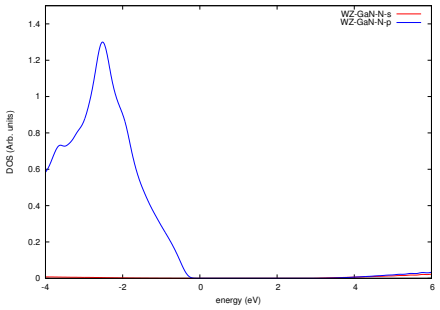

c: N in Wurtzite GaN, DOS

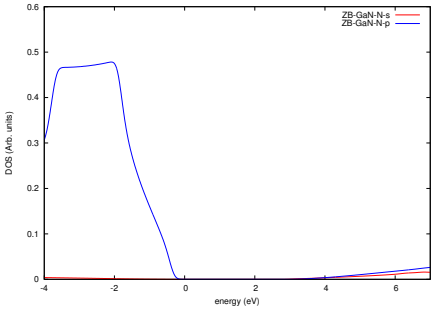

d: N in Zincblende GaN, DOS

FIGURE 3.5: The density of state for the nitrogen atoms within WZ and ZB-(In/Ga)N.(with the energy shifted such that the uppermost valence band is at zero)

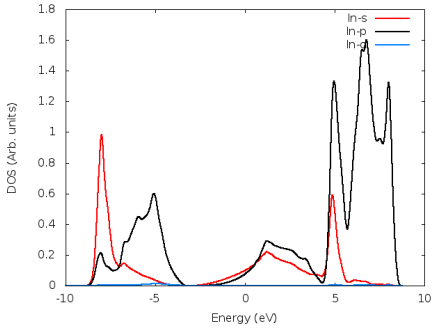

a: In in Wurtzite InN, DOS

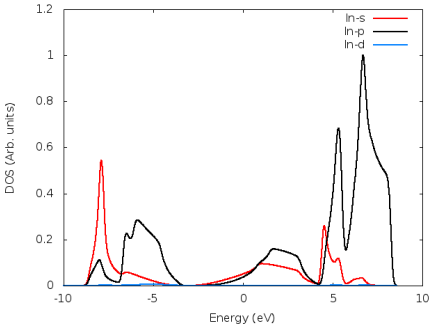

b: In in Zincblende InN, DOS

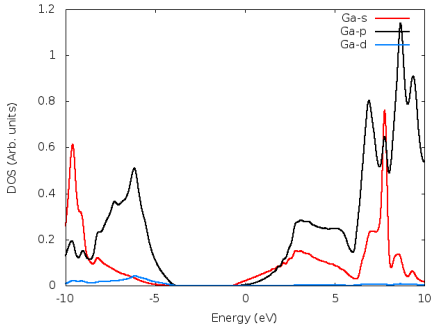

c: Ga in Wurtzite GaN, DOS

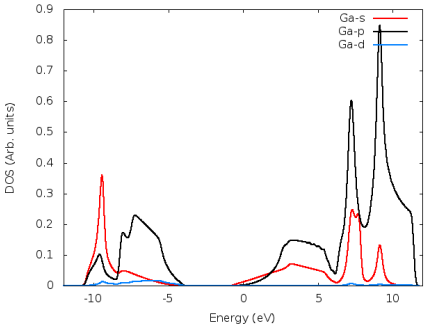

d: Ga in Zincblende GaN, DOS

FIGURE 3.6: The Density of State for In and Ga atoms around the band gap within WZ and ZB- (In/Ga)N.

and N) for both WZ and ZB. These figures illustrated the previous description for the states contributions in the total DOS and show the dominant state. These results agree with the nature of the DOS features as described by K. Lawniczak-Jablonska *et al.* [101].

3.6 Elastic Constants

Table 3.5 shown the elastic constant and bulk modulus calculated by finite difference second derivatives of the energy with respect to strain (the DFTB method for semiconductors elastic constants gives a typical error of about 10 %, however the estimated error for C_{12} is about 50 % see Ref. [102]) , compared to other calculated and experimental values for WZ InN and WZ GaN. The results obtained for GaN have acceptable values when compared with the data from literature (see table 3.5). For example the WZ elastic constants have deviations of about 2.0 % smaller, 2.0 % smaller, 6.0 % larger, 9.0 % larger, 4.0 % smaller, 2.0 %1 smaller and 3.0 % larger compared to the experimental value of Ref. [103] and about 3.0 % smaller, 1.5 % smaller, 12 % larger, 11.0 % larger, 11.0 % larger, 4.0 %1 smaller and 4.0 % smaller compared to the calculated data from Ref. [45], for C_{11}, C_{12}, C_{13}, C_{33}, C_{44}, C_{66} and B respectively. For InN the deviation compared with the average value of the calculated data shown in table 3.5 found to be somewhat higher than GaN case, where the deviation values are about 5.0 % larger for C_{11}, 16.0 % larger for C_{12}, 24.0 % larger for C_{13}, 23.0 % larger for C_{33}, 11.0 % larger C_{44}, 14.0 %1 smaller for C_{66} and 15.0 % larger for B. The C_{33}, C_{13} for both InN

and GaN bulk modulus (B) for InN found to be have significantly higher values compared with the rest of the coefficients.

	C_{11}	C_{12}	C_{13}	C_{33}	C_{44}	C_{66}	B
WZ-GaN							
This work	383	142	112	435	101	121	215
Ref [103]^{exp}	390±15	145±20	106±20	398±20	105±10	123±10	210±10
Ref [104]^{exp}	315	118	96	324	88	99	...
Ref [45]	396	144	100	392	91	126	207
Ref [105]	367	135	103	405	95	...	202
Ref [106]	366	139	98	403	97	...	200.6
Ref [107]	367	135	98	409	98	116	207
WZ-InN							
This work	250	137	117	275	54	57	169
Ref [45]	271	124	94	200	46	74	147
Ref [105]	223	115	92	224	48	...	141
Ref [106]	229	120	95	234	49	...	145.6
Ref [107]	232	115	96	239	52	59	151

TABLE 3.5: The Elastic constants and bulk modulus (GPa) for wurtzite GaN and InN, as compared to literature data for other calculated (DFT-LDA) and experimental (exp-Refs. [103] and [104] using Brillouin scattering and Raman-scattering respectively) results.

	C_{11}	C_{12}	C_{44}	B
ZB-GaN				
This work	325	162	182	216
Ref [45]	296	154	206	201
Ref [105]	296	145	206	...
Ref [106]	287	158	159	201
ZB-InN				
This work	219	141	75	167
Ref [45]	184	116	177	139
Ref [105]	187	125	86	...
Ref [106]	183	124	86	143.7

TABLE 3.6: The Elastic constants and bulk modulus (GPa) for zincblende GaN and InN are compared to literature data for other calculated (DFT-LDA) results.

Table 3.6 shows the elastic constants and bulk modulus compared to other calculated and experimental values for ZB InN and ZB GaN. The results obtained in this case have significantly higher values for C_{11} for InN and GaN and somewhat high values compared to other references for C_{12} and in InN case.

3.7 The Rocksalt Phases of InN and GaN

The variation of lattice constants, energy gaps and transition pressure between wurtzite and rocksalt phases under the external pressure have been studied for InN and GaN by optimizing Gibbs free energy as a function of pressure,

$$E^G = U + PV - TS \tag{3.2}$$

where E^G is Gibbs free energy, T is the temperature, U is the internal energy, P is pressure, V is volume and S is the entropy. Here only the electric entropy is included, other contributions such as vibrational entropy have been neglected. The obtained values of the lattice constants as a function of pressure are shown in figure 3.7. All the lattice constants for both InN and GaN decrease as the external pressure increases, the equilibrium lattice constants for wurtzite InN and GaN (at T= 0 ° K, P=0 Pa and neglecting zero point motion) are shown in table 3.1. For the rocksalt structural the lattice constant at zero external pressure are found to be 4.737 Å for InN which is close to a_r^{InN} =4.712 Å of Ref [12] about (0.53 % larger). For higher pressure the obtained value of a_r^{InN} at 12 GPa is 4.665 Å, about 0.54 % larger than 4.16 Å for Ref [108] and at 20 GPa is 4.623 Å is in a

good agreement with the 4.562 Å value of Ref [12] (only 1.34 % larger). For GaN the rocksalt lattice constant at zero pressure is 4.406 Å. For higher pressure at 50 GPa a_r^{GaN} is 4.19 Å close to 4.1 Å for [109] ($\sim$ 2.20 % larger) and at 44.1 GPa is $a_r^{GaN} = 4.21$ Å $\sim$ 1.20 % large than 4.16 Å for Ref. [108]. In general the results for lattice constants match literature values to within < 2.2 %.

Figure 3.8-a shows the variation of Gibbs free energy (equation 3.2) with the external pressure for InN. The phase transition pressure P_t for InN found to be about 24.7 GPa which is about 84 % higher than the value reported in Ref [12] for generalized gradient approximation (GGA) (13.4 GPA) and about 104 % higher than 12.1 GPa the value of Ref [110]. For GaN (fig. 3.8-b) the phase transition pressure P_t does not occur despite the increased pressure until 270 GPa which is very high value compared to both theoretical [111] and experimental [112] literature values, where its around 50 GPa.

Figure 3.9 shows the band structure of the wurtzite InN and GaN (a and c) and rocksalt InN and GaN (b and d) under 0 GPa and 25 GPa external pressure and 0 GPa and 50 GPa for wurtzite GaN. For both InN and GaN without external pressure the energy gaps are as shown previously (see table 3.2), while under high pressure the larger energy gaps can be observed at a highly symmetric Γ point with energy gaps values $\sim$1.53 eV at 25 GPa for InN and about 5.77 eV for GaN at 50 GPa. For the rocksalt case an indirect band gap is clearly observed which agree with literature (e.g. Refs. [109] for GaN and [12] for InN) where the minimum conduction bands occur at the Γ point while the maximum in the valence bands appears at the L point for both cases InN and GaN. The energy gap value of

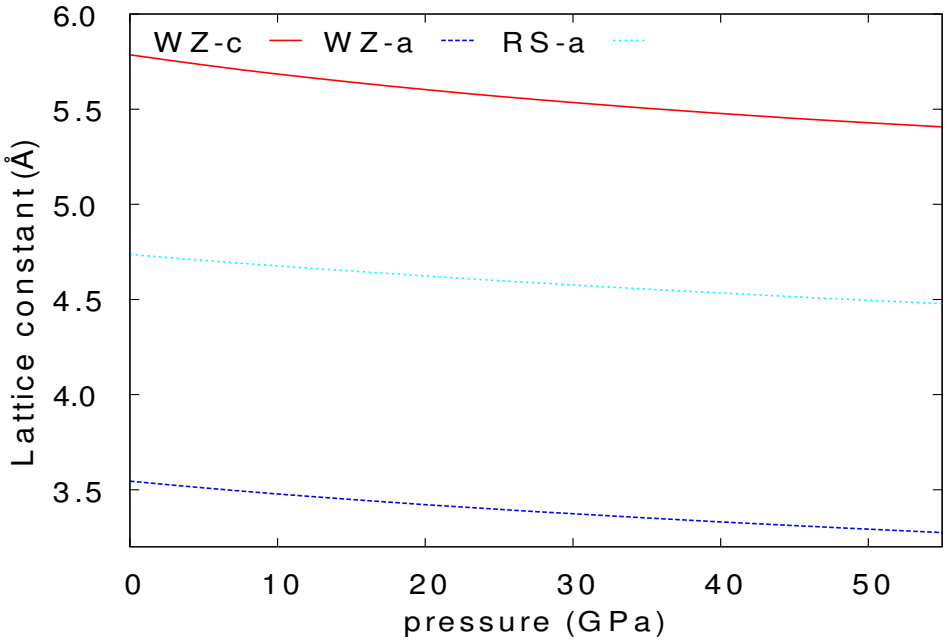

a: InN

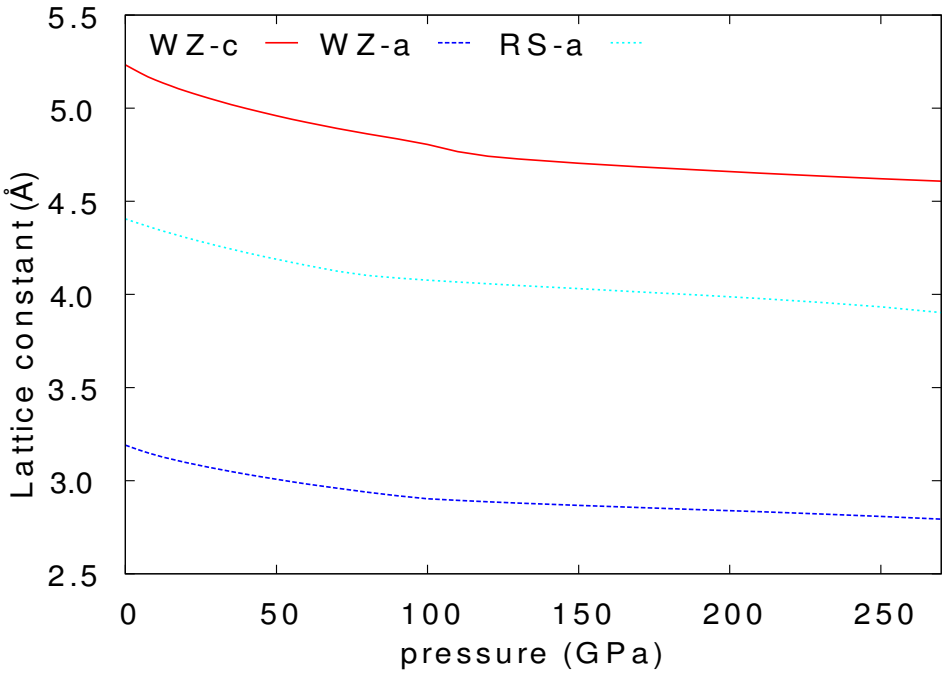

b:GaN

FIGURE 3.7: The variation in the lattice constants with external pressure for wurtzite and rocksalt (a) InN and (b) GaN

RS-InN is found to be zero at zero external pressure and begins to widen with increasing pressure which agrees with references [12] and [111], but as shown in figure 3.9-b the value of valence band maximum at L point higher than the value

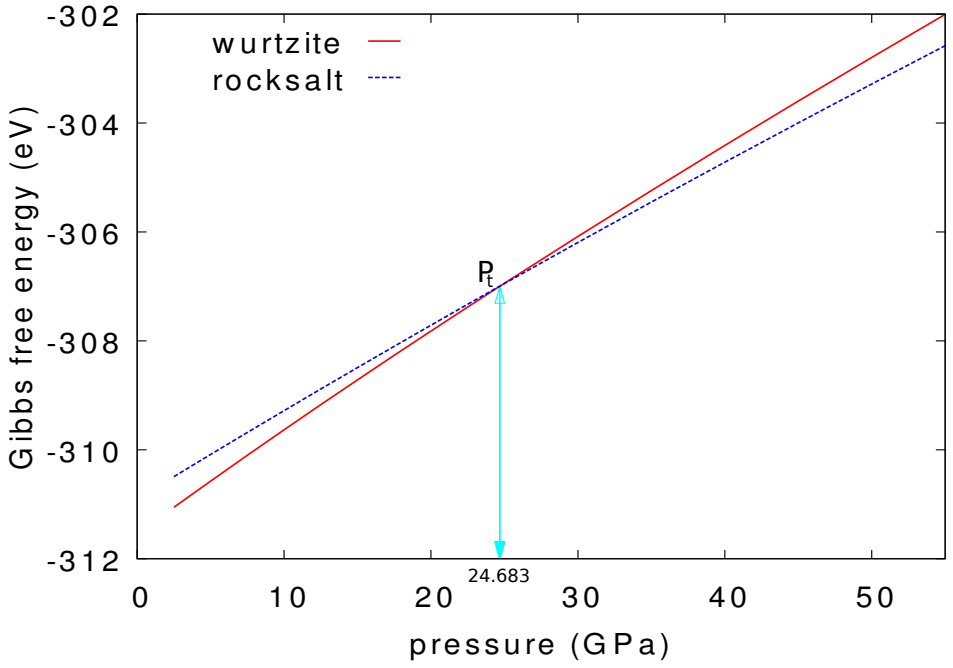

a: InN

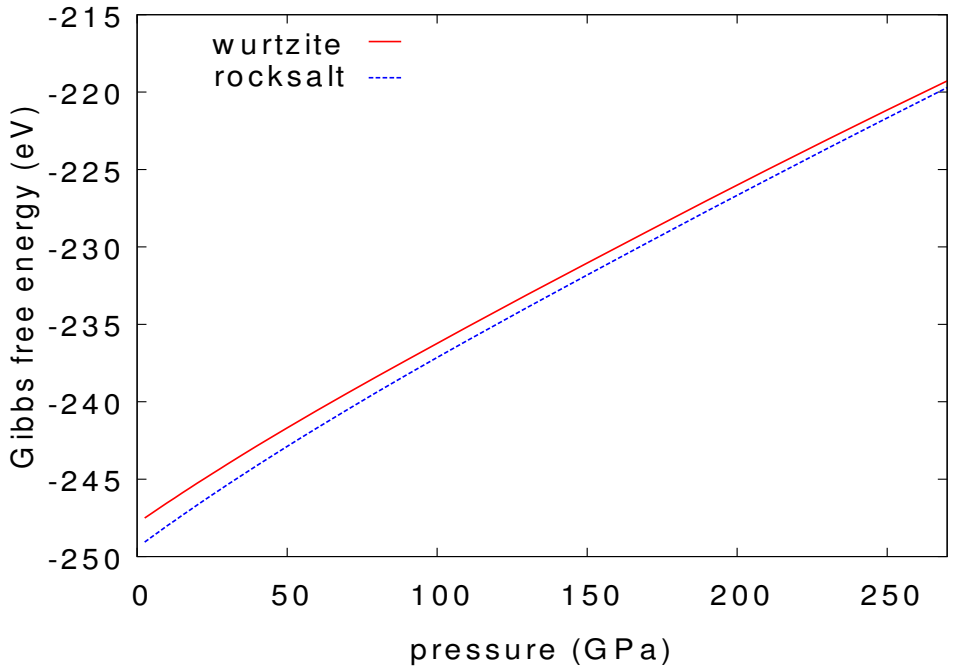

b:GaN

FIGURE 3.8: The Gibbs free energy as a function pressure for both wurtzite and rocksalt structural phases of (a) InN and (b) GaN

of conduction band minimum at Γ (a metallic behaviour). The energy gap value 1.7 eV has been mentioned in Refs. [112] and [109] associated with different values of pressure (69 GPa and 52 GPa respectively) for rocksalt GaN. To compare with

the literature the energy gap of GaN is calculated over a range of pressures, the value 1.7 eV found at about 60.6 GPa which is $\sim$ 16.53 % higher than the pressure value of [112] and 12.1 % smaller than the pressure value of ref [109], instead the energy gaps values at 52 GPa and 69 GPa are found to be $\sim$ 1.40 eV and 1.98 eV which are 17.38 % smaller and 16.59 % larger than 1.7 eV, the value 1.98 eV at 69 GPa, very close to 2.0 eV for [111] at about 43 GPa. In general the rocksalt results a show good agreement with literature except for the value of the transitional pressure.

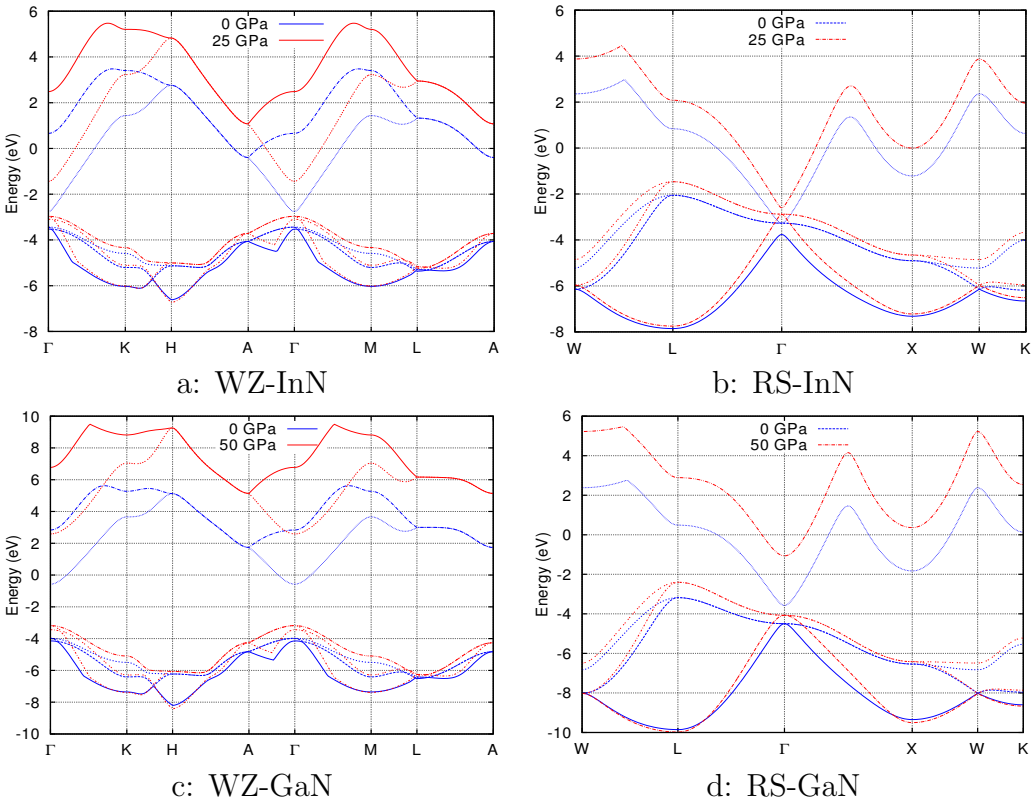

FIGURE 3.9: The band structure under different external pressures for wurtzite and rocksalt InN (a and b) and GaN (c and d)

3.8 Summary

The properties of bulk InN and GaN have been calculated by using the DFTB method. For bulk wurtzite and zincblende InN and GaN these include band gaps, equilibrium lattice constants, elastic constants, bulk moduli, effective masses and density of states. Additionally, the variation of lattice constants and energy gaps with external pressure and the transition pressure between the wurtzite and rock-salt crystal structures have been investigate for both InN and GaN. A good agreement has been obtained for these properties in comparision with previous experimental and also theoretical studies, with the exception of the value of transition pressure between polytypes, especially in the GaN case. For example the lattice constants for wurtzite case were found to be $a^{\mathrm{GaN}} = 3.191$ Å, $c^{\mathrm{GaN}} = 5.233$ Å, $a^{\mathrm{InN}} = 3.544$ Å and $c^{\mathrm{InN}} = 5.786$ Å. The deviation from the experimental values was found to be, for GaN <0.1% for a and <1 % for c respectively compared to current accepted values (e.g. Ref. [75], where a and c valuse are given to a precision of $< 5\times10^{-5}$ Å). For the InN case the a lattice constant was found to be 0.10 % smaller while the value of c is 1.36 % larger. Also the energy gap values were found to be close to the literature values, for wurtzite GaN the obtained value was 3.4 eV, only about 2.0 % and 0.30 % smaller than the experimental values of Refs. [83] and [22] respectively. The energy gap deviation for wurtzite InN is <0.5 % and 1.0 % smaller compared to the experimental values of Refs. [29] and [71] respectively. The results obtained for effective masses shows larger range of deviation in comparision with literature values in some cases, for example for the electron and heavy hole effective masses for the Γ-A direction for wurtzite InN are found

to be between 4 % larger and 3 % smaller respectively than the results of other references (shown in table 3.3). While a larger deviation is found for light hole mass, of about 88 % smaller, and for the crystal split-off mass which is 50 % larger as compared with the average of the data from the references shown in table 3.3. This fluctuation in effective mass values could be due to the parameter set used in this calculation: the atomic calculations used to create these parameters does not include spin-orbit coupling, so for example different J states can be artificially degenerate and this may be the origin of the discrepancy in the masses.

Chapter 4

The Virtual Crystal Approximation (VCA)

This chapter will show the results obtained for $In_xGa_{1-x}N$ alloys, by using the virtual crystal approximation(VCA) together with the DFTB+ code [73]. Here the semi-empirical parametrisation developed for (In,Ga) N, as discussed in chapter 3, is then averaged according to Vegard's law (equation 4.1 [113]) and has been applied to study $In_xGa_{1-x}N$ alloys. The performance of this method has been demonstrated by calculating a range of properties for $In_xGa_{1-x}N$, including energy gaps, elastic constants, carrier effective masses and the bowing parameter b. Later in this chapter will show the results obtained by using VCA and compare the results obtained for InN (x=0 case) and GaN (x=1 case) with DFTB from chapter 3 (for bulk InN and GaN) which have been already compared to other calculated and experimental results. The magnitude of the errors in the obtained properties

are expected to be similar to these calculated in chapter 3. The VCA results will then be compared with others groups work on the properties of InGaN alloys.

4.1 Introduction

In this approximation, the crystal potential is assumed to be separable into a primitive unit cell periodic part (the virtual crystal potential V_v) represented by the average potential of the constituent atoms, and a fluctuating part (V), representing the difference between the actual and virtual crystal potentials at a given point in the lattice [114]. If the role of V is secondary then electronic structure and other properties of an alloy can be calculated by standard methods of band theory developed for systems with translational symmetry, and the effect of V included separately as a perturbation. The effect of this perturbation is often referred to as the alloy scattering effect [114].

In order to set up a band structure calculation in this virtual crystal approximation (VCA), it is necessary to construct a suitably weighted (average) potential as a function of the alloy composition x. Here the semiconductor alloys are assumed to to be a weighted average of the pure compounds at $x = 0$ and $x = 1$ constituents. This approximation is usually applied by taking the actual potential in a periodic crystal to be an average of the atomic potentials of the constituents from the pure cases. For three element compound semiconductors of the form $A_xB_{1-x}C$, the crystal is usually assumed to consist of a linear mixture of $(AC)_x$ and $(BC)_{1-x}$. Under this assumption, the electron energy band structure of $A_xB_{1-x}C$ is calculated with the average lattice constant and average pseudopotentials (used to remove the core

electrons from the calculation [115]) estimated at the ratio x:$(1-x)$. The results of this approximation has been shown to agree very well with experimental observation for many systems [116], and is based on the assumption that the atoms of A and B types are distributed uniformly around the atoms of type C [116]. However, the VCA cannot correctly account for one important effect observed in almost every alloy, which is the bowing parameter. For example Ref. [117] applies virtual crystal combined within an envelope function approximation, to demonstrate that the character of the direct to indirect band gap changes in $\mathrm{A1}_x\mathrm{Ga}_{1-x}\mathrm{As}$ do not agree quantitatively with explicit large unit cell models of these alloys. Similarly Lee *et al.* [118] find that VCA cannot correctly describe the bowing parameters of ternary III-V alloys, which require an additional disorder potential. These discrepancies can be ascribed to the incorrect level of localisation of band edge states in simple schemes like VCA [119], and arise since the potential is a linear function of composition. More realistic alloy the alloy behaviour is at least quadratic in its composition;

$$P^{A_xB_{1-x}C} = \underbrace{xP^{AC} + (1-x)P^{BC}}_{\text{Vegard's law}} - x(1-x)b \tag{4.1}$$

where, P here can be any parameter, e.g E_g, lattice constant, ..., etc., with b depending on the nature of this parameter.

The form of this relationship, equation 4.1, is valid not only for the principal band gap (E_g), but also for other energy gaps (or energy differences) within the band structure, each having its own distinct value of b [120]. The applicability of this form is due to the neglect of fluctuations in the local environment, similar to the difference between the clustered and uniform cases calculated by Gorczyca *et*

al. [8]. To apply the virtual crystal to a tight-binding method, such as DFTB, we construct parameters using weighted averages of both the hopping equation 2.41 and on-site equation 2.42 integrals of the pure GaN and InN cases (which are tabulated on radial grids as a function of atomic separation). The lattice constants and, where appropriate, the internal coordinate, u, of the wurtzite lattice are also averaged. Additionally, since the SCC-DFTB method is a self-consistent approach, the atomic Hubbard U values [54] are also averaged.

4.2 Energy Gap and Lattice Constants

Figure 4.1 shows the variation of the VC energy gap with indium composition, x, for both wurtzite and zincblende $In_{1-x}Ga_xN$. Fitting Vegard-law like curves to this data by equation 4.1 gives bowing parameters b of -1.77 eV for wurtzite and -1.76 eV for zincblende. The presence of bowing in the band gaps for this form of the VCA approach is due to the self-consistent nature of the DFTB calculations, since there is a change in the charge transfer between anions and cations on moving from Ga to In, due to differences in the relative electronegativities of their atomic shells, and the resulting quadratic coulomb energy then introduces bowing.[1] [114]. The virtual crystal band-gap values for pure InN and GaN show slight discrepancies by about 0.04 eV for WZ GaN compared to the band structures calculation of DFTB, while increase for WZ-InN and ZB values (see table 4.1). This numerical artefact is due to the requirement of processing the parameters of

[1] This effect does not occur for non-SCC-DFTB or conventional tight binding methods

chapter 3 for both In and Ga to give a common grid spacing for their respective hopping integrals.

	WZ	GaN	InN	ZB	GaN	InN
VCA		3.36	0.81		3.27	0.74
DFTB		3.40	0.68		3.03	0.59

TABLE 4.1: The Energy gap (E_g) values in (eV) for wurtzite (and zincblende) GaN and InN obtained by using VCA, compared with DFTB data

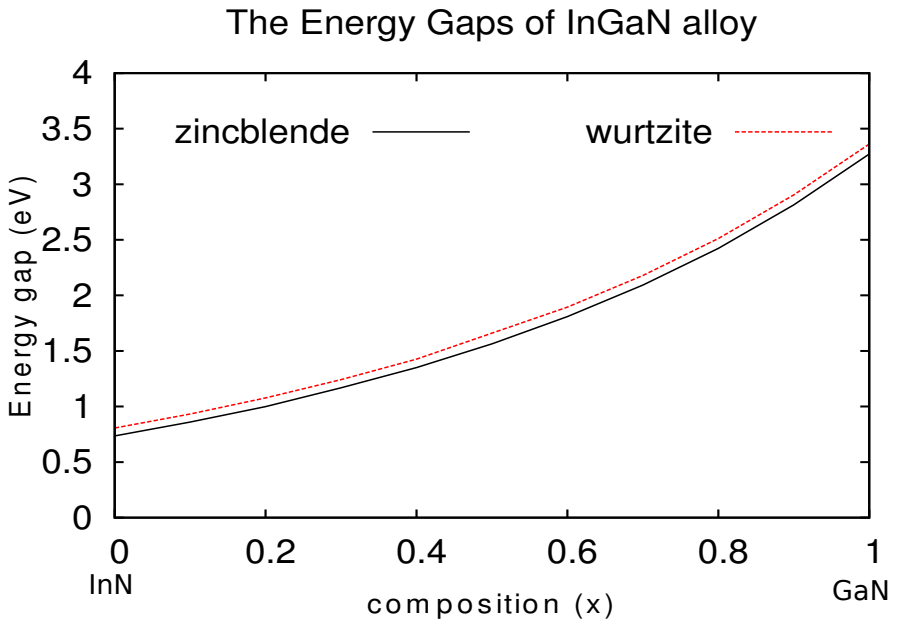

FIGURE 4.1: The variation of energy gap for zincblende and wurtzite $In_{1-x}Ga_xN$, calculated with the VCA.

Figure 4.2 shows the variation of energy gap for zincblende and wurtzite $In_xGa_{1-x}N$ compared with other calculated and experimental data from the literature, (bowing parameters and methods used to obtain these data are shown in table 4.2) the zincblende case is in good agreement with cited references, theoretical points labeled data shown as except Ref. c [121], the wurtzite results also in a good agreement with all references used in the figure except Ref. [122] (points-f_2) which is clearly an underestimate of the energy gap value, and the experimental data from Ref. k [123] at x $>$ 0.7. In general comparing to this result we can say

that VCA with charge self-consistency seems to be a good method to simulate the energy gaps in this system.

Ref.	Ref. no.	Method	b (eV)
ZB			
	This work	VCA-DFTB	1.76
	[a]Ref. [124]	DFT-LDA	1.857 ±0.093
	[b]Ref. [125]	DFT-LDA	2.08
	[c]Ref. [121]	DFT-FP-LAPW	2.68 at x = 0.5
	[d]Ref. [126]	DFT	1.62
	[e]Ref. [128]	PLE	
WZ			
	This work	VCA-DFTB	1.77
	[f]Ref [122]	DFT-LDA-1/2	1.3
	[f2]Ref [122]	DFT-LDA	1.4
	[g]Ref [129]	PL	1.4
	[h]Ref [127]	DFT- HSE06	1.36
	[i]Ref [8]	DFT-LDA+C	2.1 at x =0.5 (uniform)
	[j]Ref [130]	PL	1.43
	[k]Ref [123]	PL	2.8

TABLE 4.2: The bowing parameter for wurtzite and zincblende GaN and InN (in eV) obtained by using VCA, compared with other calculated and experimental data using in Fig. 4.2

DFT-LDA: Density Functional Theory-Local Density Approximation
FP-LAPW: Full Potential Linearized Augmented Plane Wave
PLE: Photoluminescence Excitation
HSE: Heyd-Scuseria-Ernzerhof
DFT-LDA+C: Density Functional Theory-Local Density Approximation + correction
PL: Photoluminescence

Table 4.3 shows the lattice constants for wurtzite and zincblende GaN and InN obtained by using VCA, compared with the results of chapter 3, the values of GaN lattice constant are exactly same for both WZ and ZB, but for the InN case the VCA values are slightly smaller than the original DFTB values, again this likely due to processing parameters for both elements to give a common numerical

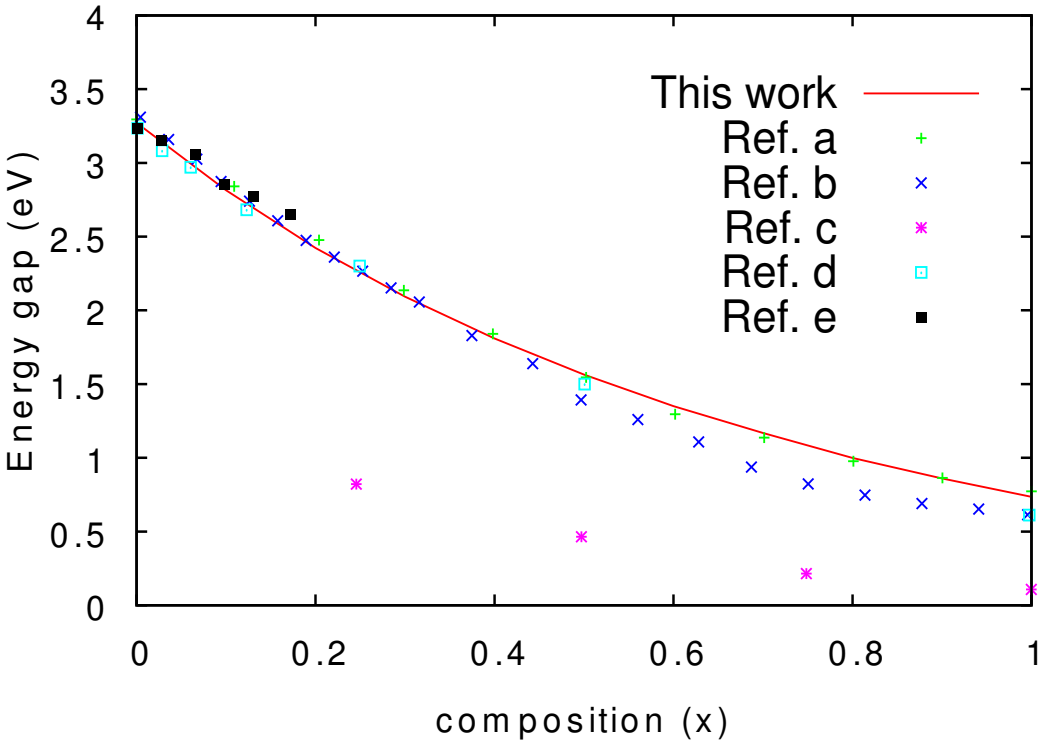

a: zincblende

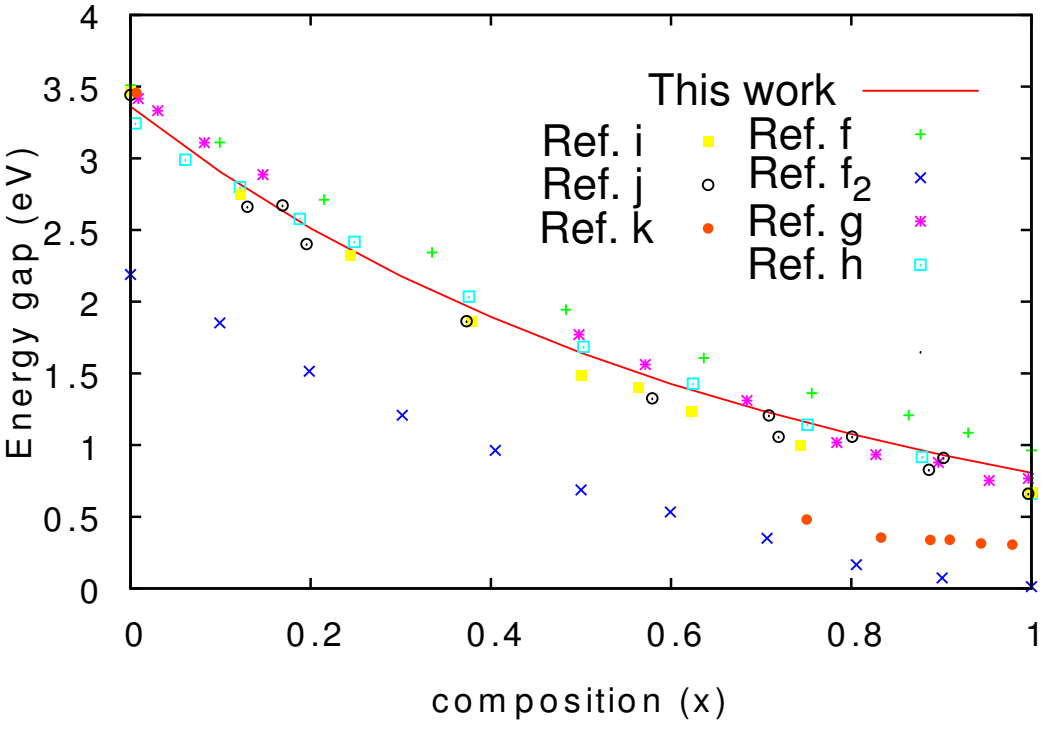

b: wurtzite

FIGURE 4.2: The variation of energy gap for zincblende and wurtzite $In_xGa_{1-x}N$, calculated with the VCA, compared with other calculated ([a]Ref. [124], [b]Ref. [125], [c]Ref. [121],[d]Ref. [126],[f,f2]Ref [122],[h]Ref [127] and [i]Ref [8]) and experimental ([e]Ref. [128], [g]Ref [129], [j]Ref [130] and[k]Ref [123]) data (for method used in these refs. see table 4.2).

grid spacing. The variation of lattice constants from GaN to InN (Fig 4.3) are approximately linear, with a small bowing of −0.074 Å, −0.123 Å and −0.105 Å for lattice constants a, c and a_0 respectively.

	a^{WZ}	c^{WZ}	a_0^{ZB}		a^{WZ}	c^{WZ}	a_0^{ZB}
GaN				InN			
VCA	3.191	5.233	4.520	VCA	3.499	5.715	4.950
DFTB	3.191	5.233	4.520	DFTB	3.545	5.787	5.01

TABLE 4.3: The lattice constants for wurtzite and zincblende GaN and InN (Å) obtained by using VCA, compared with DFTB data

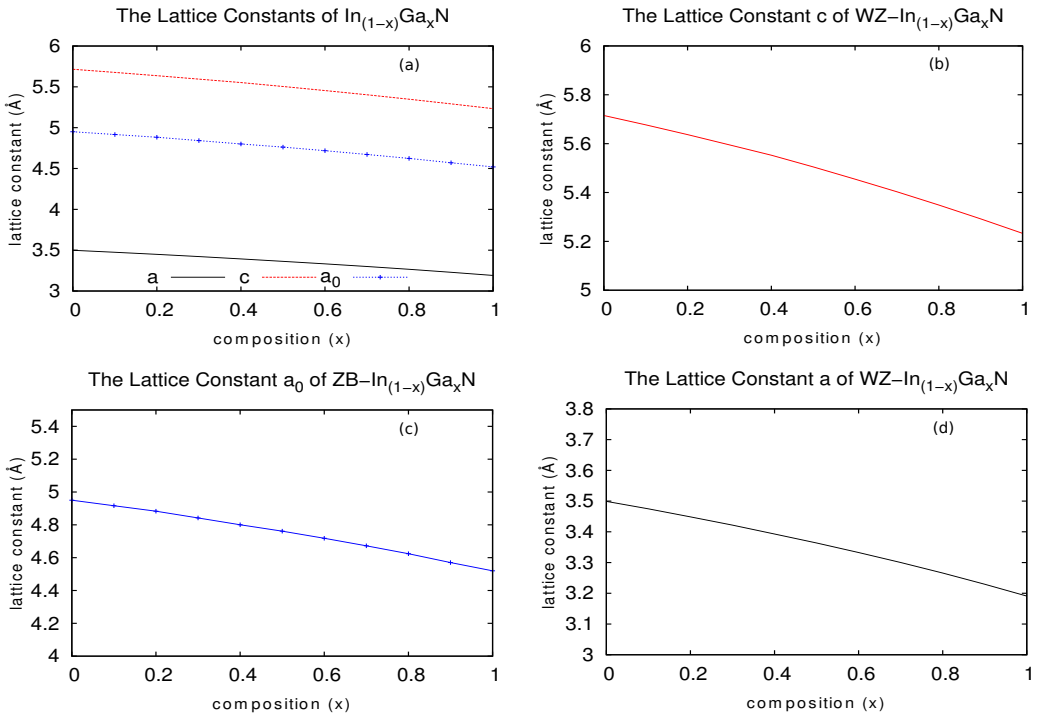

FIGURE 4.3: The variation of lattice constants a and c for wurtzite $In_{1-x}Ga_xN$ alloy and a_0 for zincblende $In_{1-x}Ga_xN$ alloy alloy with composition (x), calculated by using the VCA.

4.3 Effective Masses

Table 4.4 shows effective masses results for VCA for GaN case (x=1) and for InN case (x=0) for zincblende case, compared to DFTB results from chapter 3. The

VCA results shown are for the anisotropic spin orbit split-off hole (m_{so}) and electrons effective masses m_e which is unexpected compared to the results obtained in previous chapter and the results from literature (see table 3.4), where the values shown in the table for these two masses are the averaged values over three directions ([100], [110], and [111]). The nearest values to the DFTB InN and GaN results are found for the [100] direction in ZB, where the electrons effective masses found to be 0.278 m_0 for GaN, 0.086 m_0 for InN and the spin orbit split-off hole effective masses are 0.413 m_0 (GaN) and 0.230 m_0 (InN). The GaN electrons effective masses for other directions are found to be about 0.13 m_0 when averaging over [110] and [111], which are smaller than DFTB and other calculated and experimental results from table 3.4. The electrons effective masses for InN are in a good agreement with experimental value Ref [100]. However, the spin orbit split-off hole effective masses for the [110] and [111] directions have smaller values for GaN compared to the results from table 3.4, while the InN result are in good agreement with Ref [20]. The heavy and light holes look acceptable for the [100] direction but are worse for both the [110] and [111] directions. Figure 4.4 shows the variation of effective masses with Ga composition by using Vegard's law for zincblende case. The results obtained have acceptable behavior, but the values at the ends(x=0 and x=1) are found to be different from bulk InN and GaN DFTB calculation.

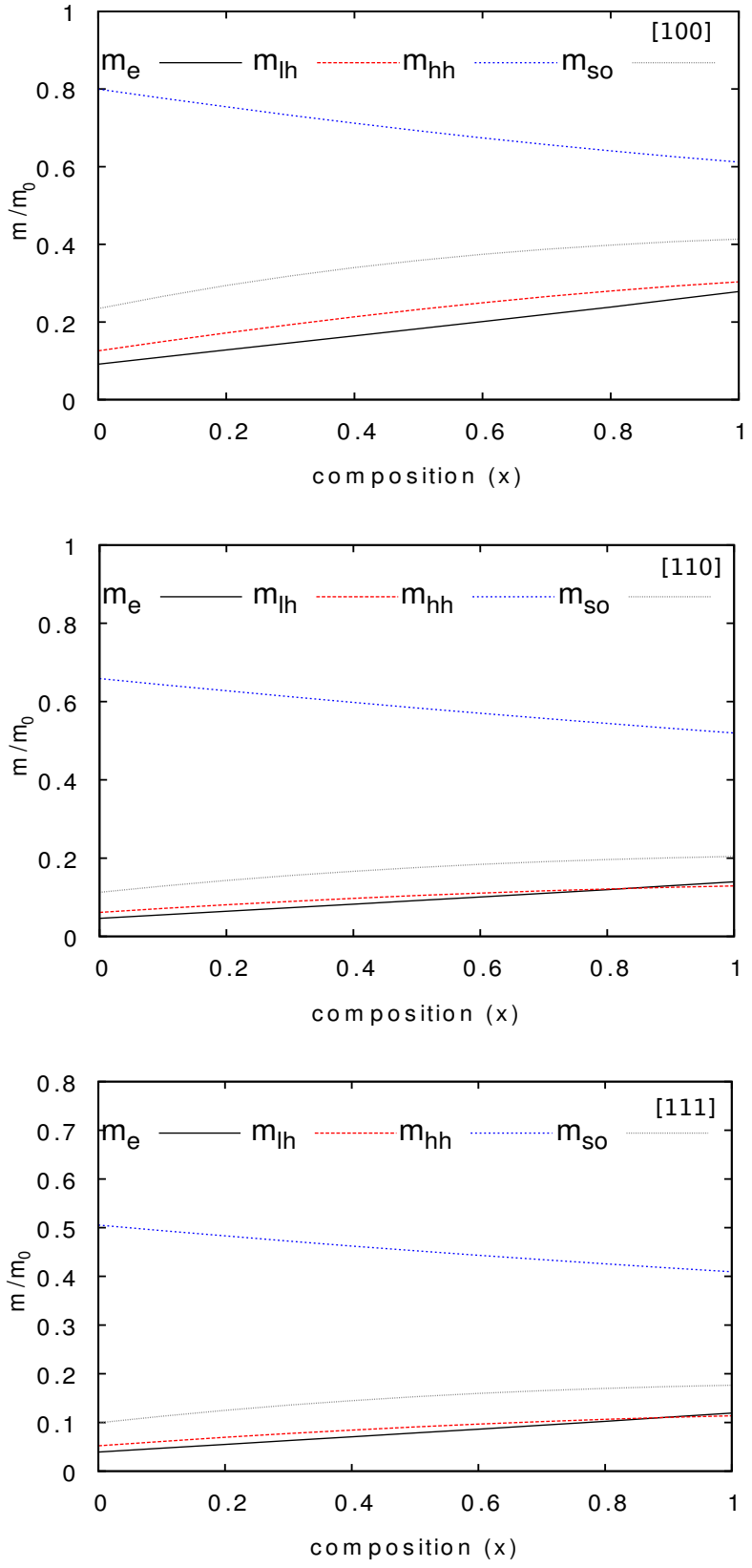

FIGURE 4.4: The variation of effective masses of electrons (m_e), heavy (m_{hh}) and light (m_{lh}) holes and spin orbit split-off holes (m_{so}) for zincblende $In_{1-x}Ga_xN$ alloy along the [100], [110], and [111] directions in units of free electron mass m_0, calculated by using VCA

	$m_{hh}^{[100]}$	$m_{lh}^{[100]}$	$m_{hh}^{[110]}$	$m_{lh}^{[110]}$	$m_{hh}^{[111]}$	$m_{lh}^{[111]}$	$m_{so}^{\star}$	$m_{e}^{\star}$
ZB-GaN								
VCA	0.612	0.304	0.520	0.129	0.409	0.114	0.265	0.179
DFTB	0.590	0.309	1.022	0.257	1.399	0.246	0.411	0.275
ZB-InN								
VCA	0.800	0.126	0.659	0.061	0.505	0.052	0.149	0.059
DFTB	0.662	0.098	1.135	0.093	1.705	0.091	0.208	0.074

TABLE 4.4: The effective masses of zincblende GaN and InN for electrons, heavy and light holes and the spin orbit split-off holes in units of free electron mass m_0. The heavy and light holes masses along the [100], [110], and [111] directions compared with DFTB data (chapter 3).

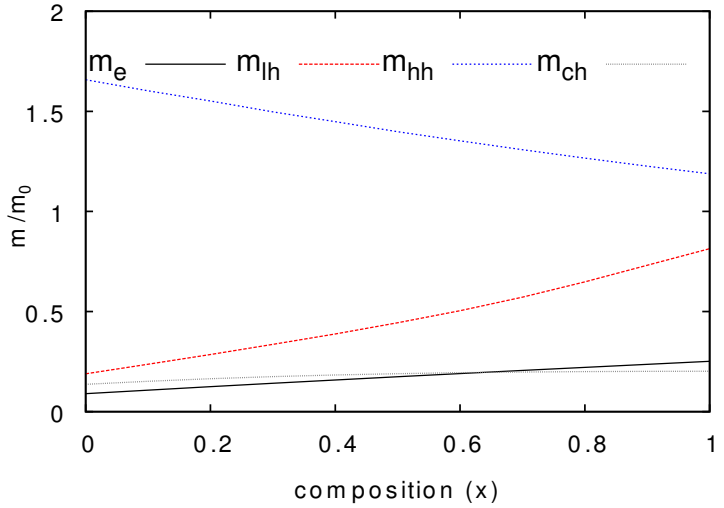

FIGURE 4.5: The variation of effective masses for electrons (m_e), heavy (m_{hh}) and light (m_{lh}) holes and crystal field split-off holes (m_{ch}) for wurtzite $In_{1-x}Ga_xN$ along the Γ-A, Γ-K and Γ-M directions in units of the free electron mass m_0, calculated by using VCA.

Figure 4.5 shows the effective masses variation of wurtzite $In_{1-x}Ga_xN$ along the path Γ-A, Γ-K and Γ-M in the Brillouin zone. These results showed that the effective masses in all directions have the same values, the bowing parameters, calculated by fitting the curves by using equation 4.1 are found to be 0.0152, -0.095, -0.232 and 0.083 (in units of m_0) for electrons, heavy, light and crystal split-off holes respectively. A large bowing is found for both the light holes curves in these cases. The values of InN and GaN effective masses as compared to the

DFTB results of chapter 3 are shown in table 4.5. All VCA GaN values along the Γ-A direction are a little bit larger than the DFTB results, except for the crystal split-off holes which remain almost the same. But for the Γ-K and Γ-M directions, the electron and crystal split-off hole effective masses have smaller values compared to DFTB result for bulk GaN (chapter 3), also crystal split-off hole masses are getting worse when comparing to the literature values in table 3.3. The light and heavy holes in these directions are also not in a good agreement with table 3.3. In the InN case, the obtained VCA results look close to DFTB and the other values in table 3.3.

	$^{\parallel}m_e^\star$	$^{\parallel}m_{hh}^\star$	$^{\parallel}m_{lh}^\star$	$^{\parallel}m_{ch}^\star$	$^{\perp}m_e^\star$	$^{\perp}m_{hh}^\star$	$^{\perp}m_{lh}^\star$	$^{\perp}m_{ch}^\star$
WZ-GaN								
VCA	0.251	1.188	0.814	0.202	0.251	1.188	0.814	0.202
DFTB	0.244	1.09	0.732	0.200	0.311	0.373	0.300	0.341
WZ-InN								
VCA	0.090	1.658	0.189	0.137	0.090	1.658	0.189	0.137
DFTB	0.086	1.797	0.180	0.120	0.105	0.142	0.232	0.21

TABLE 4.5: The Γ-A, Γ-K and Γ-M directions effective masses values for wurtzite GaN and InN for electrons, heavy and light holes and the crystal field split-off holes in units of m_0.

4.4 Density of States

Figure 4.6 shows electron DOS for $In_{1-x}Ga_xN$ alloy (over the full energy range Figs. 4.6-a and b, around the band gap Figs. 4.6-c and -d), the width of highest valence band (primarily comes from nitrogen $2p$ (see chapter 3)) increases with Ga fraction which agrees with the fact that the charge carrier has small effective mass in wide bands and a large effective mass in narrow bands [131], which true for

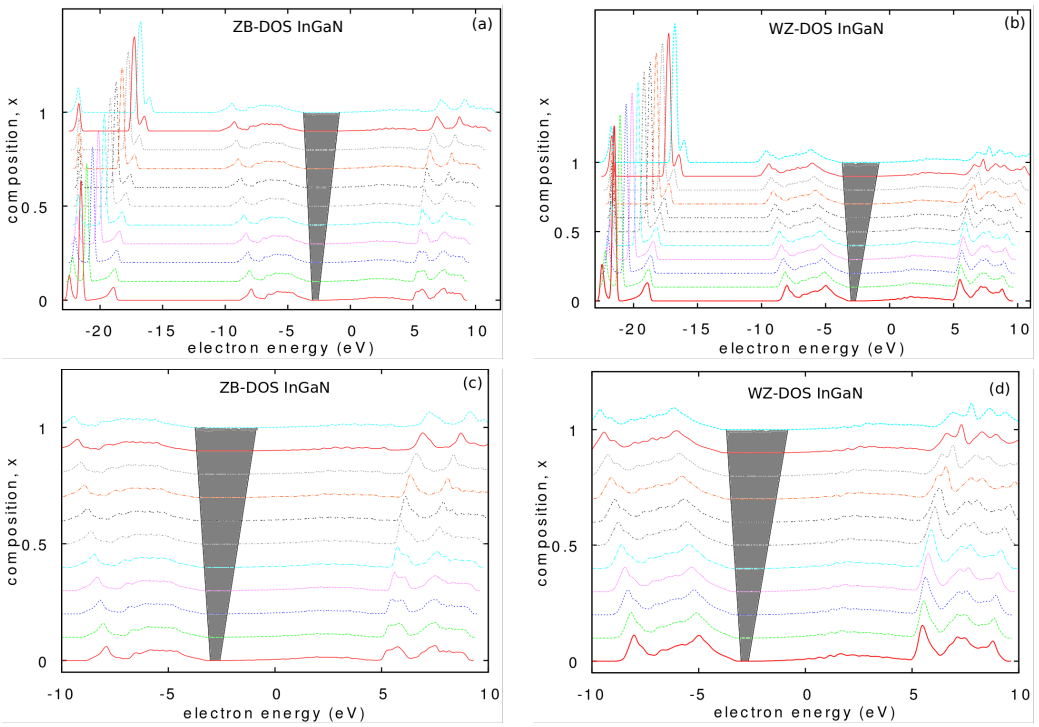

FIGURE 4.6: The variation density of states for wurtzite and zincblende $In_{1-x}Ga_xN$ alloy with composition (x), calculated by using VCA for the full range of energy in (a & b) and the energy range around the band gap (c & d). The forbidden band gap area labelled as grey colour, where the Fermi level lies somewhere in this area. The energy gap values compared to Fig. 4.2 are underestimated values, due to the broadening used to plot the DOS (see section 2.6).

heavy hole effective mass values see tables 4.4 and 4.5 for zincblende and wurtzite respectively. The value obtained for ZB-InN is 6.07 eV which in a good agreement with the value of 6.042 eV from Ref. [125] and 6.0 eV for the self-interaction and relaxation corrections (SIRC) calculations of Ref. [132]. For ZB-GaN the value found is 7.17 eV, again reasonably agreeing with 7.335 eV [125] and 7.1 eV for SIRC [132]. For the wurtzite case the GaN value is found to be 7.27 eV, close to the 7.337 eV of Ref. [133], and 7.331 eV from [134], while the obtained InN valence band width is 6.11 eV which is close to 5.735 $\pm$ 0.024 and 6.018 $\pm$ 0.095 eV estimated from the DOS figures of Ref [135] and Ref [20] respectively.

4.5 Elastic Constants

Figure 4.7 shows the variation elastic constants and bulk modulus for (a) wurtzite and (b) zincblende $In_{1-x}Ga_xN$ alloy. The variation of all constants and bulk modulus is found to be almost linear between InN and GaN for both cases. Table 4.6 shows the elastic constant and bulk modulus for wurtzite GaN and InN compared to DFTB results from section 3.6, The results obtained for the C_{11}, C_{12}, C_{13} and C_{33} elastic consistent and the bulk modulus B, for the GaN case have smaller values than GaN-DFTB, and become closer to the other references in table 3.5, except for the B value. In the InN case, C_{11}, C_{33}, C_{44}, C_{66} and B are all larger than DFTB and other data in Table 3.5, while C_{12} and C_{13} have values smaller than the DFTB original parameters by about 20 % and 32 % respectively.

In the zincblende case, in general VCA at x=1 (for GaN) have smaller values for all constant and bulk modulus, and all values become worse compared to table 4.7, except for C_{11} where the VCA result matches more closely to the other references. In the InN case all values are larger than the chapter 3 results and other data in table 4.7. This change in the values compared to the DFTB results of chapter 3, as noted earlier is due to the requirement of processing the parameters for both elements to give a common grid numerical spacing for their respective hopping integrals.

	C_{11}	C_{12}	C_{13}	C_{33}	C_{44}	C_{66}	B
WZ-GaN							
VCA	363	101	77	399	102	131	182
DFTB	383	142	112	435	101	121	215
WZ-InN							
VCA	335	109	79	371	74	113	175
DFTB	250	137	117	275	54	57	169

TABLE 4.6: The Elastic constants and Bulk modulus (GPa) for wurtzite GaN and InN are compared to the DFTB results of chapter 3 for InN and GaN parameters.

	C_{11}	C_{12}	C_{44}	B
ZB-GaN				
VCA	291	128	149	183
DFTB	325	162	182	216
ZB-InN				
VCA	231	147	141	175
DFTB	219	141	75	167

TABLE 4.7: The Elastic constants and Bulk modulus (GPa) for zincblende GaN and InN are compared to results for the InN and GaN parameters of chapter 3.

4.6 Summary

The properties of wurtzite and zincblende InGaN have been explored by using the virtual crystal approximation. The variation of energy gaps, bowing parameter, lattice constants, elastic constant, bulk modulus and effective masses with indium composition have been studied for full optimized structure for the full range of x (except for effective masses). The obtained results found to be in acceptable agreement compared with the calculated and experimental results from literature for this alloy especially for energy gaps e.g the energy gap value for zincblende $In_xGa_{1-x}N$ was found to be about 4.0% larger compared to estimated value of Ref[126] at x=0.5 and only 1.5% smaller than the estimated experimental value

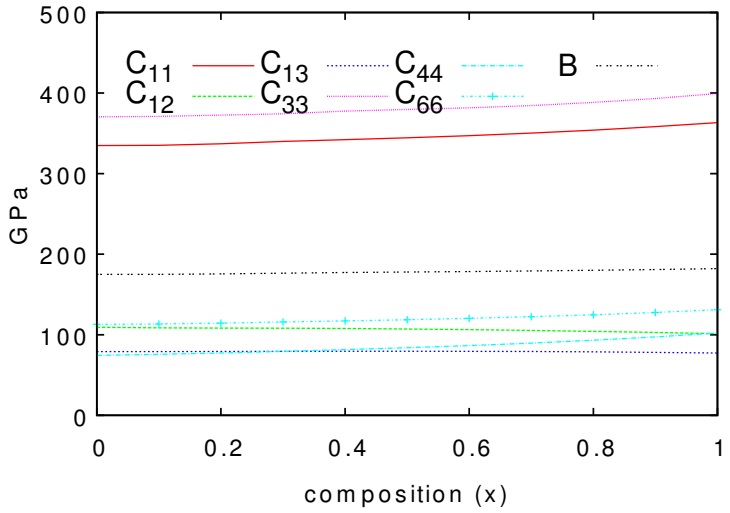

a: wurtzite

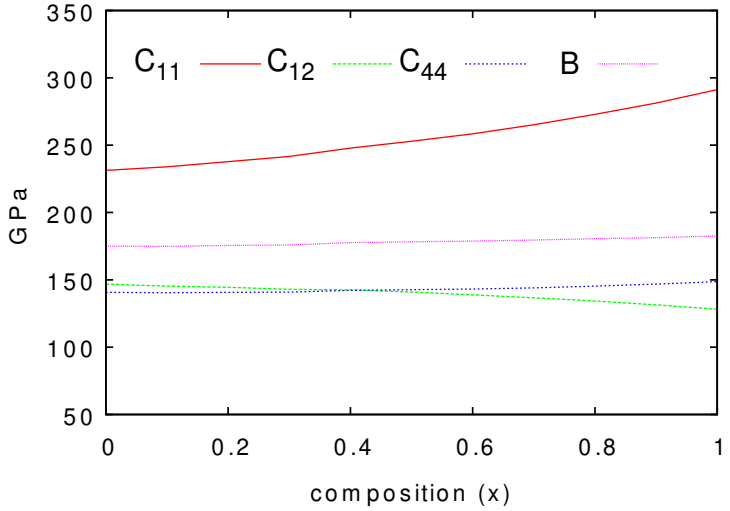

b: zincblende

FIGURE 4.7: The variation elastic constants and bulk modulus for (a) wurtzite and (b) zincblende $In_{1-x}Ga_xN$ alloy with composition (x), calculated by using VCA.

of Ref [128] at x= 0.1. Suggesting that VCA with charge self-consistency seems to be a good method to simulate the energy gaps in this system. Fitting Vegard-law like curves to this data gives bowing parameters b of -1.77 eV for wurtzite and -1.76 eV for zincblende. The variation of lattice constants from GaN to InN found to be approximately linear, with a small bowing of -0.074 Å, -0.123 Å and -0.105 Å for lattice constants a, c and a_0 respectively. The VCA effective results shown an anisotropic spin orbit split-off hole and electrons effective masses

which is unexpected compared to the results obtained in previous chapter and the results from literature for bulk InN and GaN. The density of states results showed qualitative agreement with literature, also the highest valence band width matches well: the deviation comparing literature values was found to be between about 0.50% for ZB-InN and 2.25% compared to referance [125]. A larger differnce of about 6.50% was found for WZ-InN compared to Ref. [135]. The virtual crystal values for pure InN and GaN found to be slight different compared to the previous chapter DFTB calculations, e.g. the band-gap value differs by about 0.04 eV for WZ-GaN and 0.24 eV ZB-GaN, while it increases by about 0.13 eV for WZ-InN and 0.15 eV ZB-InN values. This numerical artefact is due to the requirement of processing the parameters of chapter 3 for both In and Ga to give a common numerical grid spacing for their respective hopping integrals.

Chapter 5

The Cluster Expansion Method (CEM)

In this chapter InGaN alloy has been studied by using cluster expansion methods (CEMs) together with DFTB by expanding the alloy in series of all of the atomic geometries for a given size unit cell of a chosen crystal structures. The total energies and the optimised atomic geometries for 8, 16, 32 atom cells[1] (with 7, 22 and 995 unique structures for wurtzite and 6, 16 and 990 unique structures for zincblende[2]), the energy gaps for all cases and the variation of effective masses, elastic constant, lattice constant, density of states as a function of In composition, and as either free standing (relaxed) or grown on GaN substrate (pseudomorphically strained) have been studied for the 16-atom case. Once again the magnitude

[1]The conventional 4 atom cell, used for wurtzite were repeated as 2×2×2, 2×2×1 and 2×1×1 superclls for the 32, 16 and 8 atom unit cells respectively. For the zincblende case the 2 atom fcc primitive cell has bee repeated as 2×2×4, 2×2×2 and 2×2×1 super cells for the 32, 16 and 8 atom unit cell respectively.

[2]For example in the zincblende 8-atom case, there is one unique structure for each of the pure InN and GaN cells, one case for one indium atom, two for equal indium and gallium and structure for three indium atom case.

of the errors in the obtained properties are expected to be similar to these calculated in chapter 3. Later in this chapter will show the results obtained by using CEM and compare them with the results obtained by VCA for InGaN alloy from chapter 4 and other calculated and experimental results from the literature.

5.1 Introduction

In binary alloys such as A_xB_{1-x}, the configuration of the crystalline lattice can have several local environments according to the ratio x between its constituent atoms. For example, in the case of an alloy with a unit cell consisting of four atoms, the composition possibilities are as follows 4A, 3AB, 2A2B, A3B and 4B.[3] Ternary alloys such as $In_xGa_{1-x}N$ consist of 2ρ atoms (ρ anions, In or Ga, and ρ cations N) [24] where the anions atoms are arbitrarily distributed on one sublattice, and the N atoms occupy the other sublattice positions. In the cluster expansion method, the alloy is divided into M clusters, each of them consisting of 2ρ atoms (ρ anions and ρ cations) [136], due to the symmetry of the primitive (or supercell) unit cell of the crystal lattice, the number of possible local environments (structures) can be reduced from M to $J+1$ different classes. Each class j (where $j = 0, 1, \ldots, J$) has its own degeneracy factor g_j (g_j gives the number of clusters with the same total energy ε_j). The sum of the clusters of each degenerate class gives the total number of clusters in the alloy, M;

$$M = \sum_j g_j \tag{5.1}$$

[3] there are five types of local environment in this model of the alloy.

and the composition weight of each cluster given by;

$$x_j = \frac{g_j}{M} \tag{5.2}$$

From 5.1 and 5.2, x_j is required to obey

$$\sum_j x_j = 1 \tag{5.3}$$

The clusters can be discerned by the number of A sites n_j (In atoms in the present case) and the number of B sites, $n - n_j$ (here Ga), these numbers are constraints on the given average composition x given by [18, 24];

$$\sum_{j=0}^{J} n_j x_j = nx \tag{5.4}$$

By using the Connolly-Williams ([136] and [24]) formula, any property P can be calculate from a weighted average of the individual "clusters" properties as;

$$P(x,T) = \sum_{j=0}^{J} x_j P_j \tag{5.5}$$

For example, mixing energy (change in energy on mixing InN and GaN together to make an InGaN solid solution consisting equally of all M clusters) for a specified set of clusters g_j is [18];

$$\Delta U = \sum_{j=0}^{J} g_j \varepsilon_j - M\left[(1-x)\varepsilon^0_{\mathrm{GaN}}(n) + x\varepsilon^0_{\mathrm{InN}}(n)\right] \tag{5.6}$$

where $\varepsilon^0_{GaN}(n)$ and $\varepsilon^0_{InN}(n)$ are the energies of an n-atom cluster in pure GaN and InN crystals, respectively. Chosing the cluster energy $\varepsilon_0 = \varepsilon_{\mathrm{GaN}}(n)$, where, $\varepsilon_{\mathrm{GaN}} = \varepsilon_0 - \varepsilon^0_{\mathrm{GaN}}(n)$ and $\varepsilon_J = \varepsilon_{\mathrm{InN}} = \varepsilon_J - \varepsilon^0_{\mathrm{InN}}(n)$, allows equation 5.6 can to be written as

$$\Delta U = M\left[(1-x)\varepsilon_{\mathrm{GaN}} + x\varepsilon_{\mathrm{InN}}\right] + M\sum_{j=0}^{J} x_j \Delta\varepsilon_j \tag{5.7}$$

where the reduced excess energies, $\Delta\varepsilon_j$, are given by [18, 24, 136];

$$\Delta\varepsilon_j = \varepsilon_j - \frac{n-n_j}{n}\varepsilon_0 - \frac{n_j}{n}\varepsilon_J \tag{5.8}$$

The first term of ΔU (equation 5.7) does not effect the temperature dependence arising from averged statistical quantities for given x, because all temperature dependence arising from the statistical mechanics is contained in the $x_j(T)$. The mixing entropy can be calculated from [137];

$$\Delta S(x,T) = k_B \ln W \tag{5.9}$$

where K_B is Boltzmann constant and W given by [24];

$$W = \frac{N!}{N_{In}!N_{Ga}!}\frac{M!}{\prod_j g_j!}\prod_j \left(x_j^0\right)^{g_j} \tag{5.10}$$

[3] $\Delta\varepsilon_j$ excess energy compared to Vegard's law-like line interpolation

where x_j^0 is the random alloy value[4] and given by [18];

$$x_j^0 = g_j x^{n_j}(1-x)^{n-n_j} \tag{5.11}$$

From equations 5.9 and 5.10 the resulting mixing entropy is;

$$\Delta S(x,T) = -k_B N\left(x\ln x + (1-x)ln(1-x)\right) - Mk_B \sum_{j=0}^{J} \ln\left(\frac{x_j}{x_j^0}\right) \tag{5.12}$$

Using equations 5.7 and 5.12 we can find the mixing free energy expression $\Delta F = \Delta U - T\Delta S$ in terms of x_j.

5.2 Generalized Quasi-chemical Approximation (GQCA)

In this approximation, to find the equilibrium cluster probability for which the Helmholtz free energy[5] is minimized by taking the partial derivative of ΔF with respect to the cluster distribution x_j;

$$\frac{\delta \Delta F}{\delta x_j} = 0 \tag{5.13}$$

[4] corresponding to the probability of a cluster being proportional only to its degeneracy.

[5] Strain is not usually considered in this case, so the Helmholtz free energy is used instead of the Gibbs free energy.

Thus x_j^{GQCA} given by [18, 136]

$$x_j^{\mathrm{GQCA}} = \frac{g_j \eta^{n_j} e^{\beta \Delta\varepsilon_j}}{\sum_{j'}^{J} g_{j'} \eta^{n_{j'}} e^{\beta \Delta\varepsilon_{j'}}} \tag{5.14}$$

where, $g_j = \binom{n}{n_j}$ and $\sum_{j=0}^{J} g_j = 2^n$.

Here $\beta = 1/K_B T$, T the temperature $\Delta\varepsilon_j$ is the excess energy of cluster j (equation 5.8), and η is the activity, which is a consequence of minimizing equation 5.14 with respect the constraint 5.4 (i.e. a Lagrange undetermined multiplier).

5.2.1 Strict-Regular Solution model (SRS)

In strict-regular solution model or zeroth approximation [18], ΔU is not zero but the mixing entropy is still equal to the random alloy result, i. e. x_j^0 are independent of the temperature (T) and the "clusters's" excess energies ($\Delta\varepsilon$) and ideal cluster fractions are used 5.11 [138]; This approximation can be considered as a special case of the GQCA at high temperatures (to calculate x_j we need only the degeneracy factor g_j and the number of cations n_j);

$$W^{\mathrm{SRS}} = \frac{N!}{N_{\mathrm{In}}! N_{\mathrm{Ga}}!} \tag{5.15}$$

5.2.2 Microscopic Decomposition Model (MDM)

In cases where cations of the same type are more stable when close to each other (e.g. In close to In) [136, 138], the two binary components InN and GaN will occur

in the edges of the alloy (pure InN and GaN), with xM being the number of GaN clusters and $(1-x)M$ the number of InN clusters. This case gives a system of decomposed regions of pure InN and GaN between the binary end components (Vegards law 4.1). The cluster fractions for the MDM are given by;

$$x_j^{\mathrm{MDM}} = \begin{cases} 1-x & \text{for} \quad j=0 \\ x & \text{for} \quad j=J \\ 0 & \text{otherwise} \end{cases} \tag{5.16}$$

This case can be considered as a special case for GQCA at low temperatures provided that all $\Delta\varepsilon_j > 0$. The partition function for this case with only the two clusters for $j=0$ and $j=J$ (W^{MDM}) is;

$$W^{\mathrm{MDM}} = \frac{M!}{(xM)!\,((1-x)M)!} \tag{5.17}$$

5.3 Energy Gap and Lattice Constants

The variation of energy gap with indium composition for 8, 16 and 32 atom unit cells for the system have been studied for the zincblende and wurtzite $In_xGa_{1-x}N$ alloys, the results shows the energy gaps for all cases at the ends of the composition range $x=0$ (GaN) and $x=1$ (InN) are 3.406 eV and 0.682 eV for wurtzite GaN and InN respectively and 3.312 eV and 0.619 eV for zincblende GaN and InN respectively. For the range of the cell sizes, the values in between these ends are found to be vary, and as a consequence of this difference, the bowing parameters

(b) for 8, 16 and 32 atom systems are found to be different as well, showing an increase with the number of atoms. The | b | values are found to be 1.677 eV, 1.744 eV and 1.875 eV for wurtzite and 1.581 eV, 1.672 eV and 1.794 eV for zincblende for

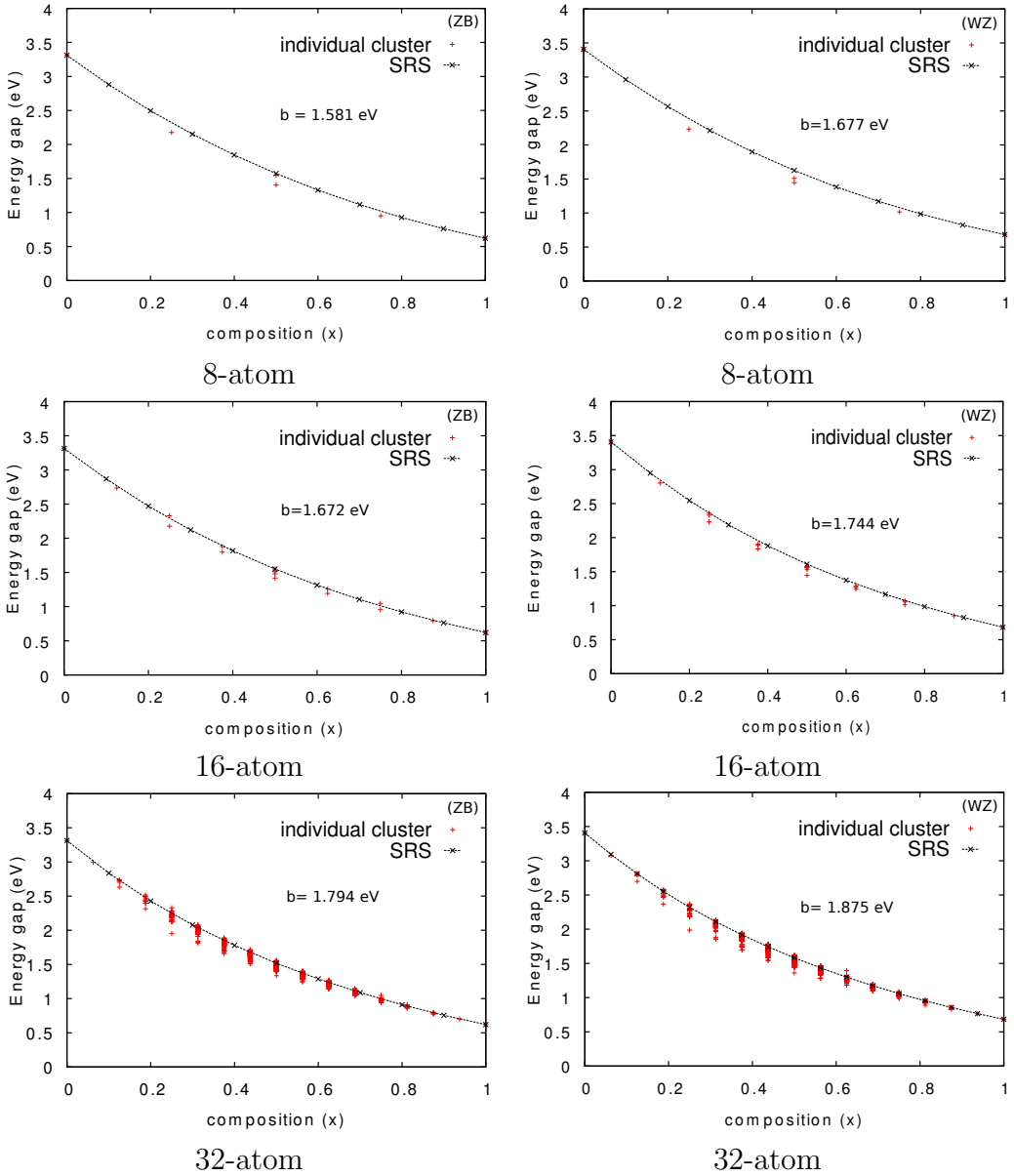

FIGURE 5.1: The variation of energy gaps for (a) zincblende and (b) wurtzite $In_xGa_{1-x}N$ alloy with composition (x), calculated by using the CEM and SRS models (solid line).

the 8, 16 and 32 atom respectively. Figs. 5.1 and Figs. 5.2 show that the difference between the 8 and 16 atom cells is smaller than the difference between the 16

and 32 cells in both the zincblende and wurtzite cases (suggesting the cluster expansion converges for sufficiently large unit cells). The greatest difference is found at $x \approx 0.4$ where the energy gap for the 16 atom case is 2.15 % larger than for 32 atoms and 1.54 % smaller than for 8 atoms of ZB, and 1.81 % $>$ 32 atoms and 1.18 % $<$ 8 atoms for WZ case. In general the three cases have a good agreement with both the VCA result from chapter 4 and with other calculated and experimental data. Figure 5.3 shows the results for the SRS ensemble in 32 atoms are closer to experiment (yellow circles for ZB case, light blue squares and yellow circles for WZ case) data than the other results, which means that simulating the crystal with small numbers of atoms can lead to somewhat misleading results. Also choosing specific configuration (e. g. work byGorczyca *et al.* [8]) can lead to poorer agreement with experimental data.

Figure 5.4 shows the variation of bowing parameter with temperature T up to 1.6x10^4 K, the shape of the curves are found to be same for zincblende and wurtzite with differences in the values. In general the bowing parameter increases with temperature, but this increase is not at a constant rate, as the curves are divided into three different regions in terms of the value of bowing parameter, and the shape of the curves (linear, nonlinear and saturation regions). For the wurtzite case, b is zero for $T \leqq 255$ K (the MDM region) then starts increasing linearly with temperature up to $T \leqq 600$ K with $0 < b \lessapprox 0.09$ eV. Then for $600 < T \leqq 6{\times}10^3$ K the curves become nonlinear with b values varying between $0.09 \lessapprox b \lessapprox 1.63$ eV, after this point the increase in the bowing parameter value slows, with b approaching $\sim$1.706 eV at $1.6{\times}10^4$ K, which is close to the value obtained by the

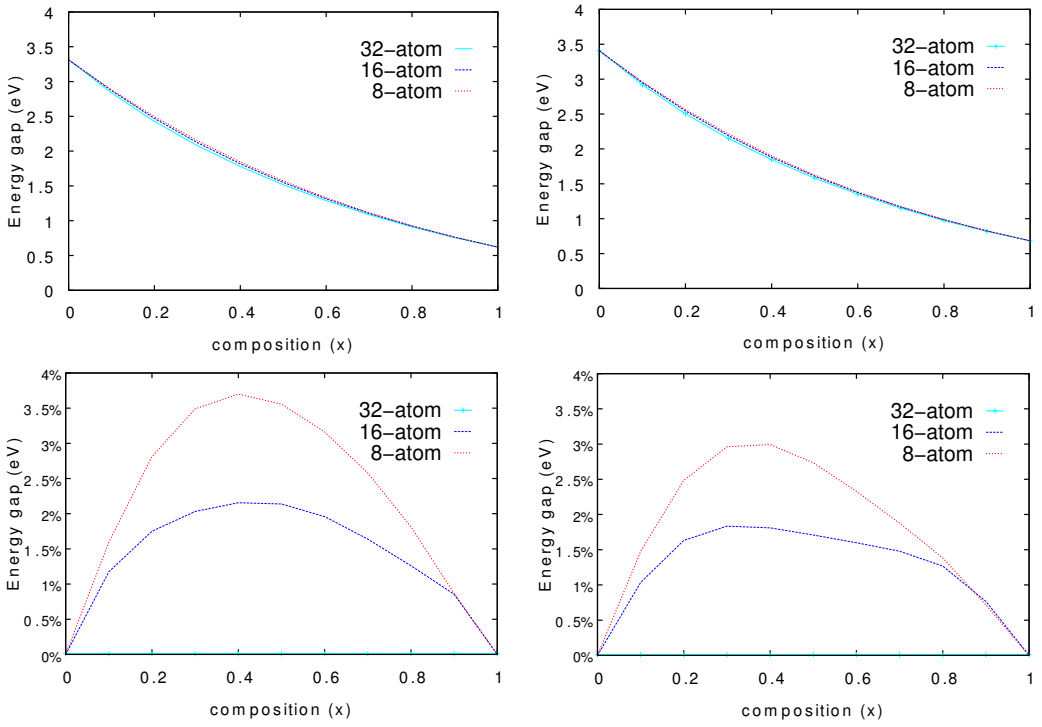

a: zincblende b: wurtzite

FIGURE 5.2: Impact of the size of unite cells used in the cluster expansion on the value of energy gaps (a) zincblende and (b) wurtzite of $In_xGa_{1-x}N$ alloy with composition (x), calculated by using CEM and SRS model.

SRS approximation (1.744 eV). For the zincblende case, the MDM region ends at about 600 K, then the linear region occurs until about 900 K, with $b \lessapprox 0.054$ eV, then the nonlinear region occurs up to $\sim 6{\times}10^3$ K, with $0.054 \lessapprox b \lessapprox 1.52$ eV; Finally as with the wurtzite case, the bowing parameter value increasing slowly with temperature to eventually be 1.672 eV at T =$1.6{\times}10^4$ K, which is exactly same as the obtained SRS value.

The recommended b value of Vurgaftman *et al.* [21] for wurtzite and zincblende (1.4 eV) occurred at $T \simeq 2.50{\times}10^3$ K and $T \simeq 3.90{\times}10^3$ K for wurtzite and zincblende respectively. The relationship between bowing parameter and the indium composition x, has been studied by fitting the energy gap values via equation 4.1, using two formulae describing bowing parameter as a function of x,

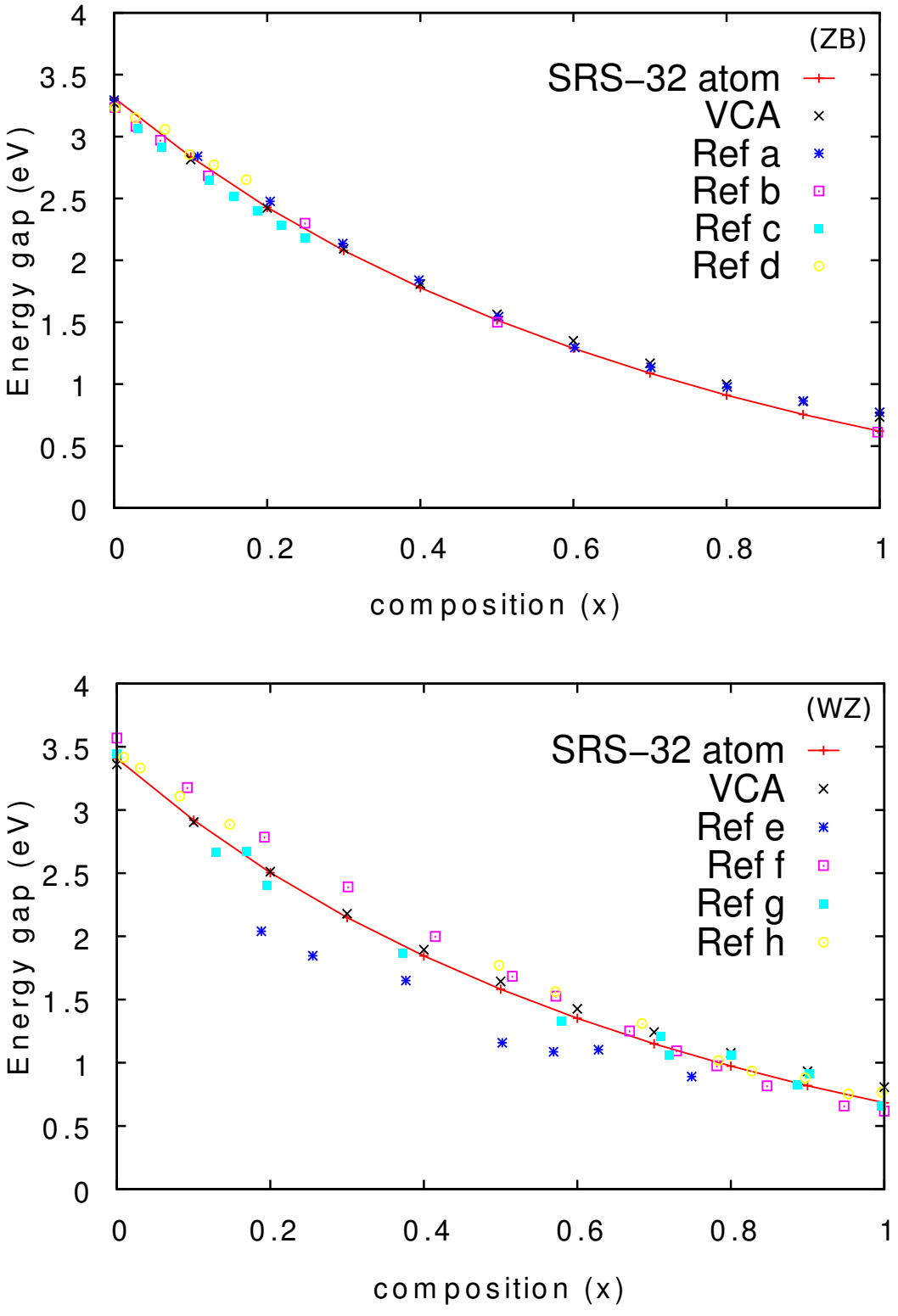

FIGURE 5.3: The variation of energy gap for zincblende and wurtzite of $In_xGa_{1-x}N$ in 32 atom cells, calculated with the CEM (SRS), compared with other calculated values ([a]Ref [124], [b]Ref [126], [c]Ref [139] and [f]Ref [136]) and experimental data ([d]Ref [128], [e]Ref [8], [g]Ref [130] and [h]Ref [129]).

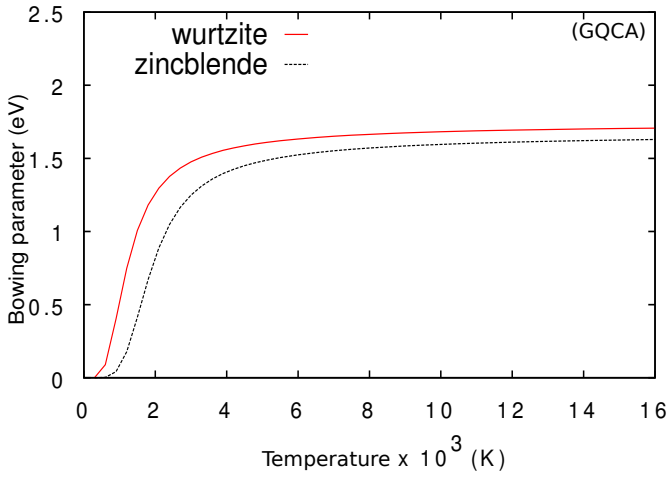

FIGURE 5.4: The variation of the energy gap bowing, b, for zincblende and wurtzite 16 atom $In_xGa_{1-x}N$ alloy cells with temperature (T). Calculated by using the the GQCA model.

namely equations 5.18 and 5.19 which were proposed by Iliopulos *et al.* [140] and Sakalauskas *et al.* [141] respectively, on the basis of their experimental data.

$$b1(x) = \frac{B_0}{1 + B_1 x} \tag{5.18}$$

$$b2(x) = \frac{B_0}{1 + B_1 x^2} \tag{5.19}$$

where, B_0 and B_1 are constants.

Both equations fit the data curves very well, with negligibly small differences between them[6], as shown in figure 5.5. The obtained bowing parameters are found to decrease as In composition increases, as shown in the inset of figure 5.5. The obtained values of $b1(x)$ range from about 2.24 eV to $\sim$ 1.43 eV for wurtzite, from $\sim$ 2.12 eV to $\sim$1.38 eV for zincblende respectively, while the bowing parameter

[6]The root mean square value in the wurtzite case found to be 2.61×10^{-3} for b1(x) and 3.82×10^{-3} for b2(x). For the zincblende the root mean square values are 1.93×10^{-3} for b1(x) and 4.75×10^{-3} for b2(x).

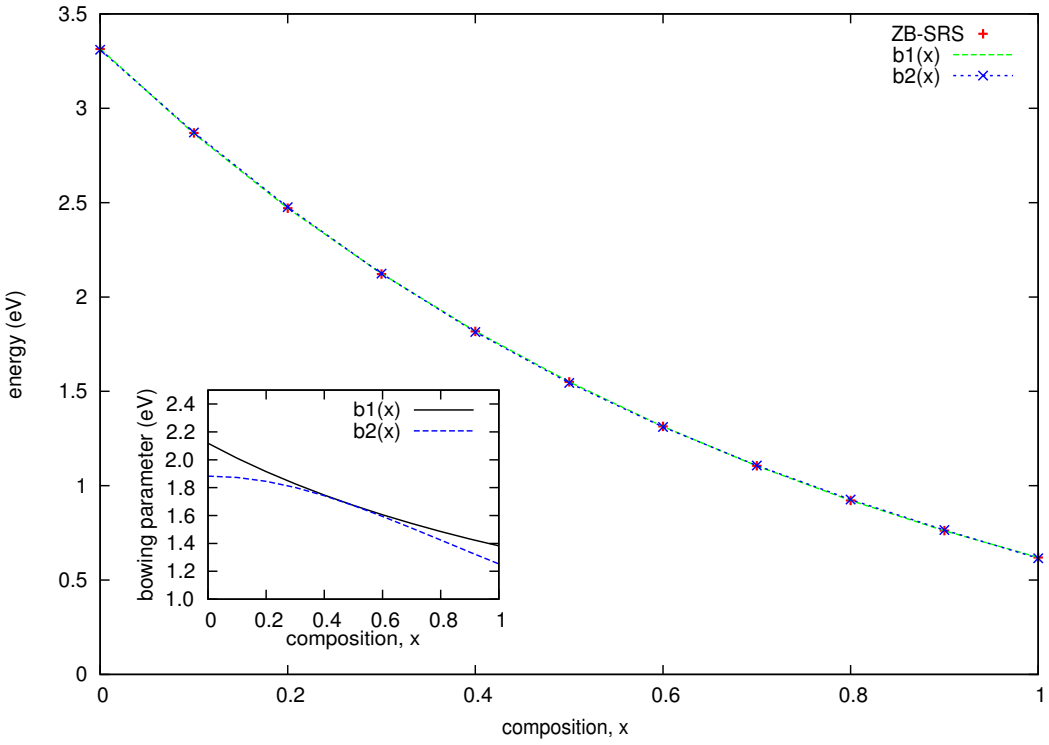

a: zincblende

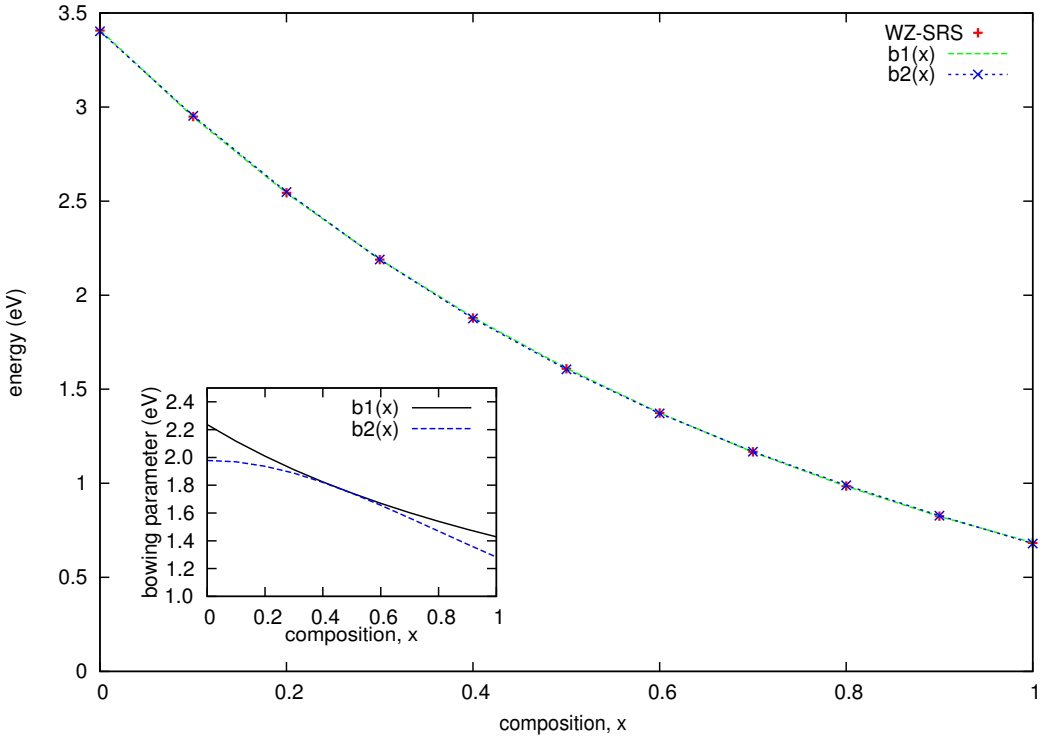

b: wurtzite

FIGURE 5.5: Fitted energy gap data with bowing parameters $b1(x)$ and $b2(x)$ from equations 5.18 and 5.19 respectively, for (a) zincblende and (b) wurtzite $In_xGa_{1-x}N$ alloy with composition (x), the inset is the variation of bowing with In composition.

$b2(x)$ is found to range from ∼1.98 eV to ∼1.28 eV for wurtzite, and from ∼ 1.88 eV to ∼ 1.25 eV for zincblende.

The variation of lattice constant for the zincblende and wurtzite $In_xGa_{1-x}N$ alloys with indium composition are shown in figure 5.6 for the 16 atom unit cell case, the values of the constant c for wurtzite are found to be 5.233 Å and 5.786 Å

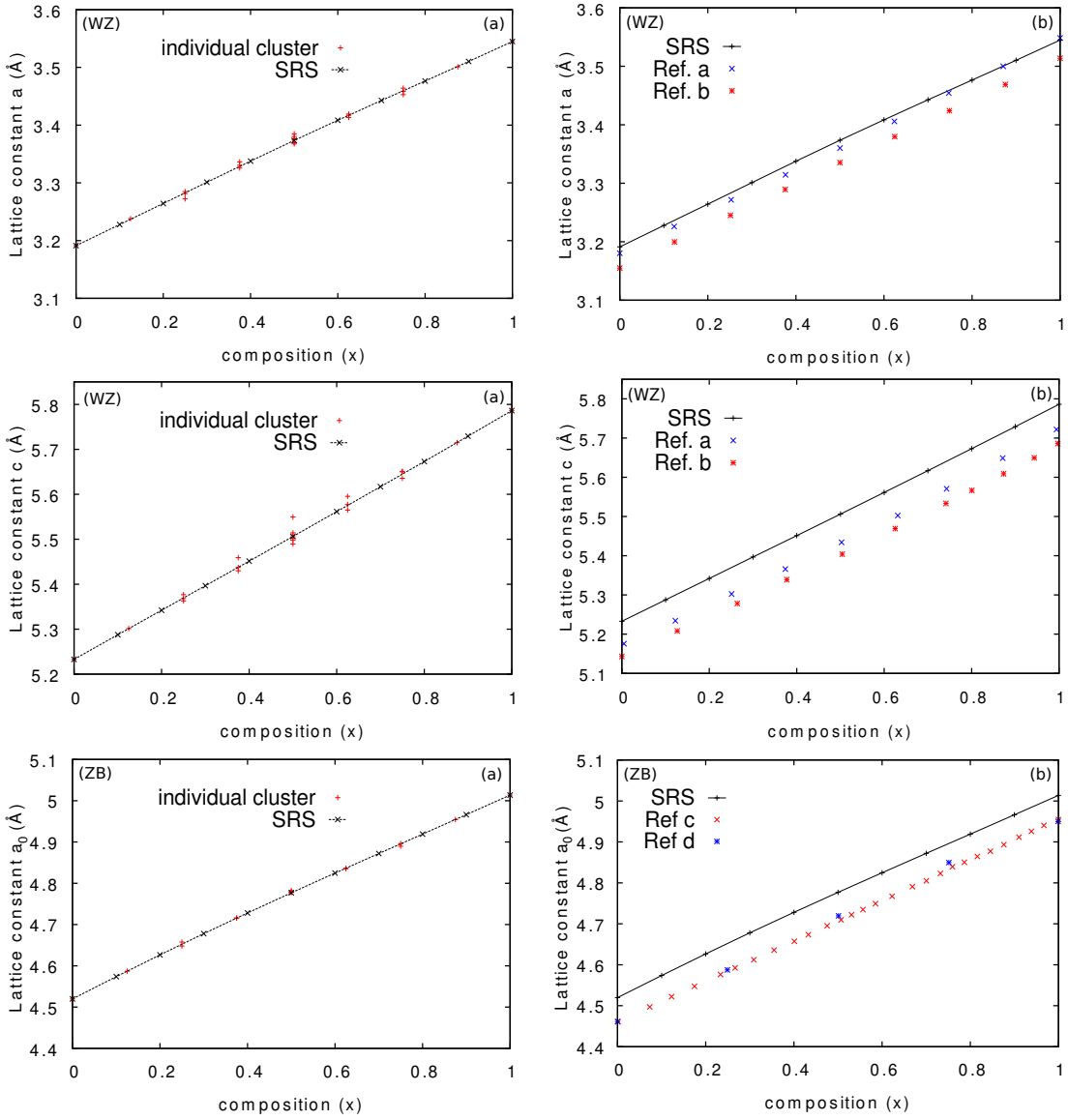

FIGURE 5.6: The variation of lattice constant (a) for zincblende and wurtzite $In_xGa_{1-x}N$ alloy with composition (x),(b) the SRS average compared to other calculations ([a]Ref [136],[b]Ref [142],[c]Ref [24],[d]Ref [143]).

for GaN and InN respectively, with nearly linear variation between the ends of the composition range ($b = -0.013$ Å). The obtained a-plane lattice constants are 3.191 Å and 3.544 Å for GaN and InN respectively, with a small bowing, where the obtained value of b is 0.02 Å (here the bowing parameters for lattice constants are calculated by fit the data by using Vegard's law equation 4.1). For the zincblende case the values of a_0 found to be 4.521 Å and 5.012 Å for GaN and InN respectively, again with a nearly linear variation with respect to x (the bowing parameter value is somewhat larger than the wurtzite case being $b = 0.04$ Å). Figure 5.6-b shows the lattice constants compared to other calculated data from the literature, the variation in behaviour with x is found to be similar compared to these references, but their values at $x = 0$ and $x = 1$ are smaller than the present values, leading to the figures showing nearly parallel lines.

Figure 5.7, shows the variation of band gap energy (a) and c lattice constant (b) for $In_xGa_{1-x}N$ grown pseudomorphically on a GaN [0001] substrate. This calculation is performed by fixing the c-plane lattice constants at the values of the GaN substrate, but allow relaxation along the c direction. The energy gap results for $In_xGa_{1-x}N$ shown that the values obtained for strained alloys are less than that of the unstrained material. This likely due to the increasing c lattice parameter (see Fig. 5.8). The energy gaps results for strained material are in a good agreement with calculated and experimental band gaps from literature, Refs. [144] and [145] respectively. On the other hand the lattice parameters c for strained alloy found to be larger than that for unstrained alloy, where the strained c lattice constant for pure InN is about 9.20 % larger than c-InN for fully relaxed

material. This behaviour agrees with experimental values from Ref. [146] and with values calculated by using equation 5.20;

$$c_{st} = \left(\frac{-Da - Da_{InGaN} + a_{InGaN}}{a_{InGaN}} \right) c_{InGaN} \tag{5.20}$$

where, a_{InGaN} and c_{InGaN} are the lattice constants of the unstrained alloy, a is substrate a lattice constant and D is Poisson's ratio, which is calculated as a function of elastic constants as [145] ($D = 2C_{13}/C_{33}$).

This expression is derived by using Vegard's law, see Ref. [145] for details. Here it is used to confirm that the increasing in c lattice parameter is a correct behaviour in these strained alloys. As with the unstrained alloy case, the values of the c lattice constants are overestimated in this work about 0.95 % at $x = 0$ and about 0.80 % at $x = 0.2$ compared to Ref [146].

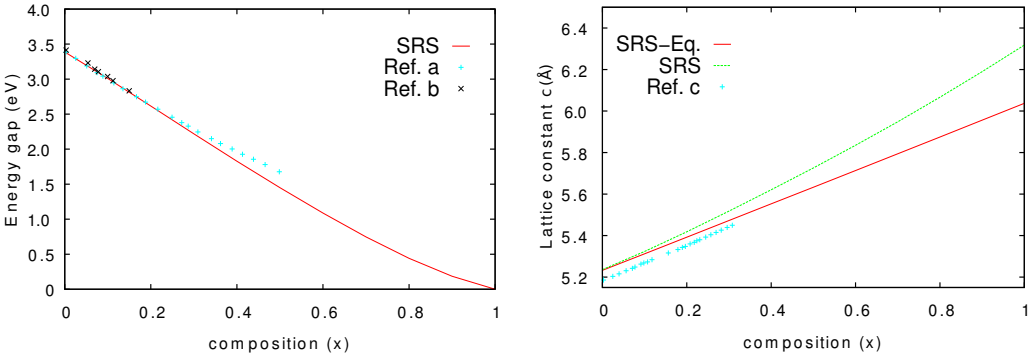

a: Energy gaps b: Lattice constant c

FIGURE 5.7: The variation of (a) band gap energy and (b) the c lattice constant for wurtzite 16 atom cells of $In_xGa_{1-x}N$ alloy on a GaN substrate with In composition (x), SRS results compared to literature values from [a]Ref [144], [b]Ref [145] and [c]Ref [146] (where SRS-Eq. is the strict-regular solution model for the data obtained by using equation 5.20 and SRS is strict-regular solution model for c lattice constant obtained in this work).

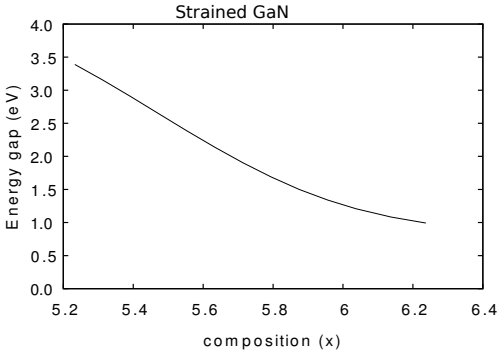

FIGURE 5.8: The effect of increasing the c lattice constant on the energy gap value for WZ-GaN.

5.4 Effective Masses

Figure 5.9 shows the effective mass for ZB $In_xGa_{1-x}N$ along the directions Γ-X, Γ-M and Γ-L. The SRS model (fig 5.9-a.) shows big fluctuations, especially for the light and heavy hole masses for all directions, due to some unusual values of effective masses for specific clusters within the expansion (and also the random nature of the resulting alloy, see below for discussion). This is due to superlattice effects, where unlike the bulk InN and GaN, some superlattice structures show strong difference between the band structures along the Γ-[010], Γ-[100] and Γ-[001] directions, as shown in Fig 5.11. When comparing with other structure of the same composition (Fig 5.11-b) it is clear that the curves in case (b) are exactly the same along these three directions. Figure 5.9-b shows the GQCA at low temperature ($T \leqq 10^3$ K), where use of the GQCA model leads material which approaches the MDM limit (the average of a linear mixture of composition), but at high temperatures GQCA approaches the SRS limit.

Around x= 0.5 composition there is strong effect from disorder on the effective masses. At low temperature, as discussed by Popescu and Zunger [147], the valence

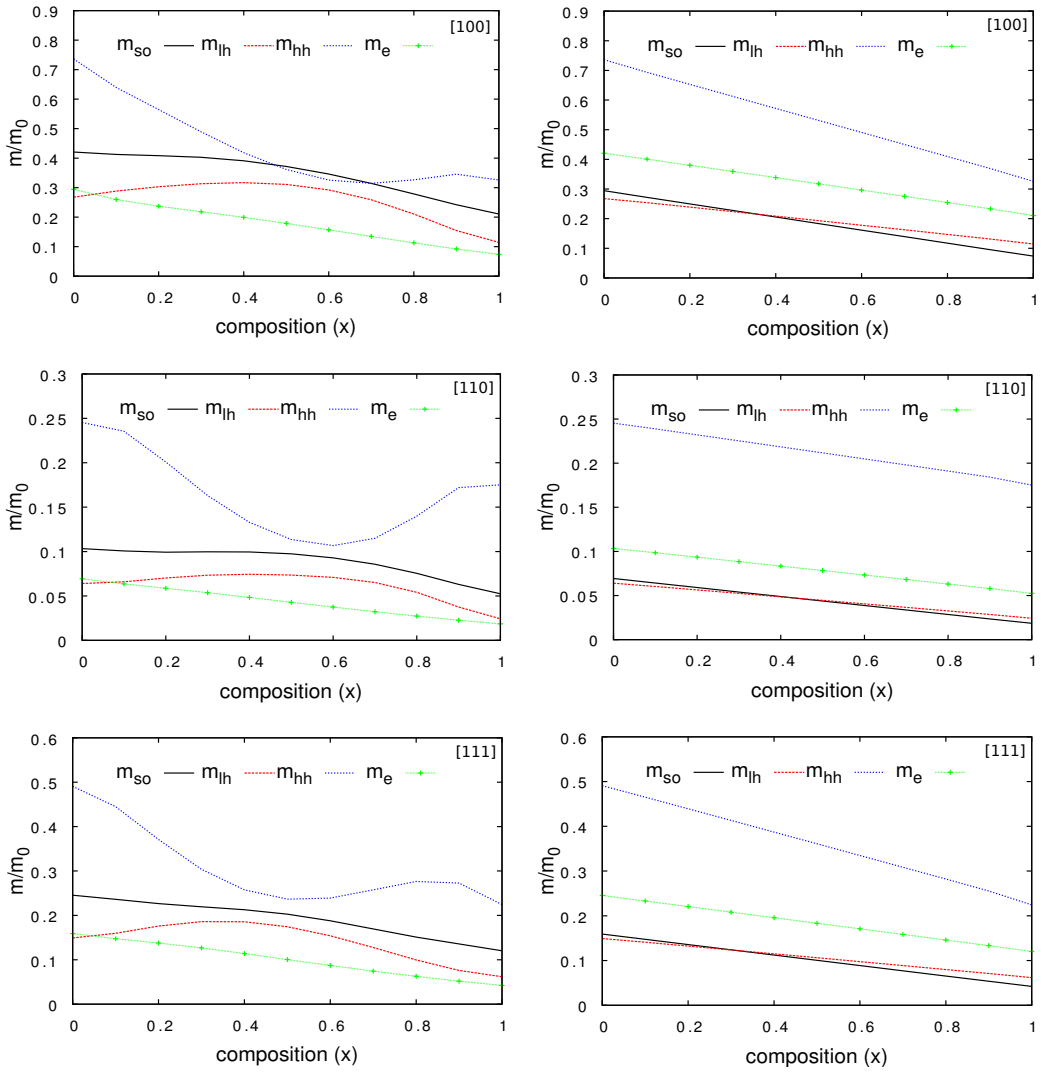

FIGURE 5.9: The variation of effective masses of electrons (m_e), heavy (m_{hh}) and light (m_{lh}) holes and spin orbit split-off holes(m_{so}) for $In_xGa_{1-x}N$ alloy along the [100], [110], and [111] directions in units of the free electron mass, m_0, calculated by using CEM in tow ensembles (a) SRS model and (b) GQCA (at $T = 10^3$ K).

band structure of random zincblende alloy unit cells shows strong disruption of the Bloch-like states. This would lead to a loss of the distinction (difference) between the light and heavy hole bands particularly in the middle of the composition range (since there are more structures contributing to the cluster expansion here). This behaviour can be seen in Fig. 5.9-a. The composition dependence obtained by using GQCA is found to be approximately linear, similar to the VCA, with a very

small bowing range of about 10^{-3} m_0 for most curves, except for heavy holes in the Γ-L direction, where the bowing parameter value was found to be 0.0124 m_0.

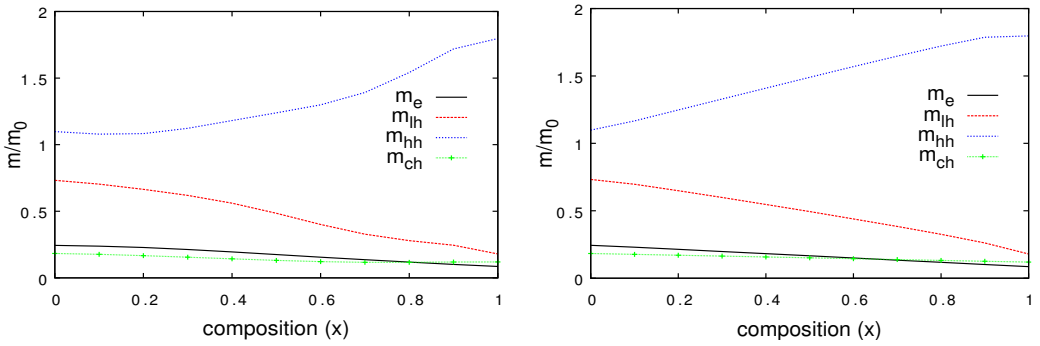

FIGURE 5.10: The variation of electrons (m_e), heavy (m_{hh}) and light (m_{lh}) holes and crystal field split-off hole (m_{ch}) effective masses for wurtzite $In_xGa_{1-x}N$ along the Γ-A, Γ-K and Γ-M directions in units of the free electron mass, m_0, calculated by using CEM, (a) SRS model and (b) GQCA (at $T = 10^3$ K).

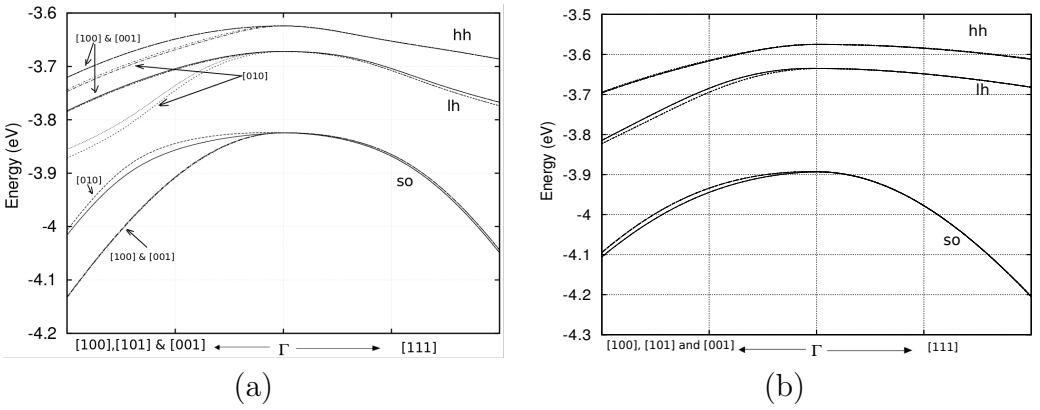

FIGURE 5.11: The uppermost valence bands of ZB $In_{0.5}Ga_{0.5}N$, shown along chosen directions in the Brillouin zone: the Γ-[100], Γ-[101], Γ-[001] and Γ-[111] for (a) a structure with asymmetry along the Γ-[100], Γ-[101], Γ-[001] and Γ-[111] and (b) a structure with symmetry along the Γ-[100], Γ-[101], Γ-[001] and Γ-[111] (The curves of the three directions are superposed on each other).

The wurtzite results are shown in Fig. 5.10, here the results obtained for wurtzite effective masses are found to be the same along the directions the Γ-A, Γ-K and Γ-M, but unlike bulk InN and GaN (see table 3.3), again as with the VCA case. In general the SRS curves for wurtzite are more continuous and uniform, unlike the

zincblende case, where the lh and hh masses are not linear, but all effective mass values lie between those of InN and GaN. The effective mass variation obtained by using GQCA is found to be linear between the InN and GaN values.

5.5 Density of State

Figure 5.12 shows the DOS of all of the different 16 atom $In_xGa_{1-x}N$ unit cells. A strong change is seen for different clusters of the same composition, especially in the conduction band states. The width of the top valence band generally decreases with In composition (Fig. 5.13), here the value obtained for ZB-InN is 5.88 eV, about 3.10 % smaller than the VCA value from chapter 4, which in reasonable agreement with the theoretical values of 6.042 eV from Ref. [125] and 6.0 eV for self-interaction and relaxation corrected (SIRC) calculations from Ref. [132]. The valence band width of ZB-GaN has a value of 7.22 eV, only about $\sim 0.70\%$ larger than the VCA value, which in a good agreement with 7.335 eV [125] and 7.1 eV for SIRC [132] as shown in the previous chapter. For the wurtzite case, the obtained value of the valence band width for GaN is 7.23 eV, $\sim 0.55\%$ smaller than VCA calculation, and close to literature values of 7.337 eV [133] and 7.331 eV [134]. The InN band width is 5.89 eV, $\sim 3.6\%$ smaller than the VCA, and also close to the 6.018 ± 0.095 eV and 5.735 ± 0.024 eV estimated from the DOS figures (Fig.2) of Ref [20] and Fig.1 from Ref [135] respectively.

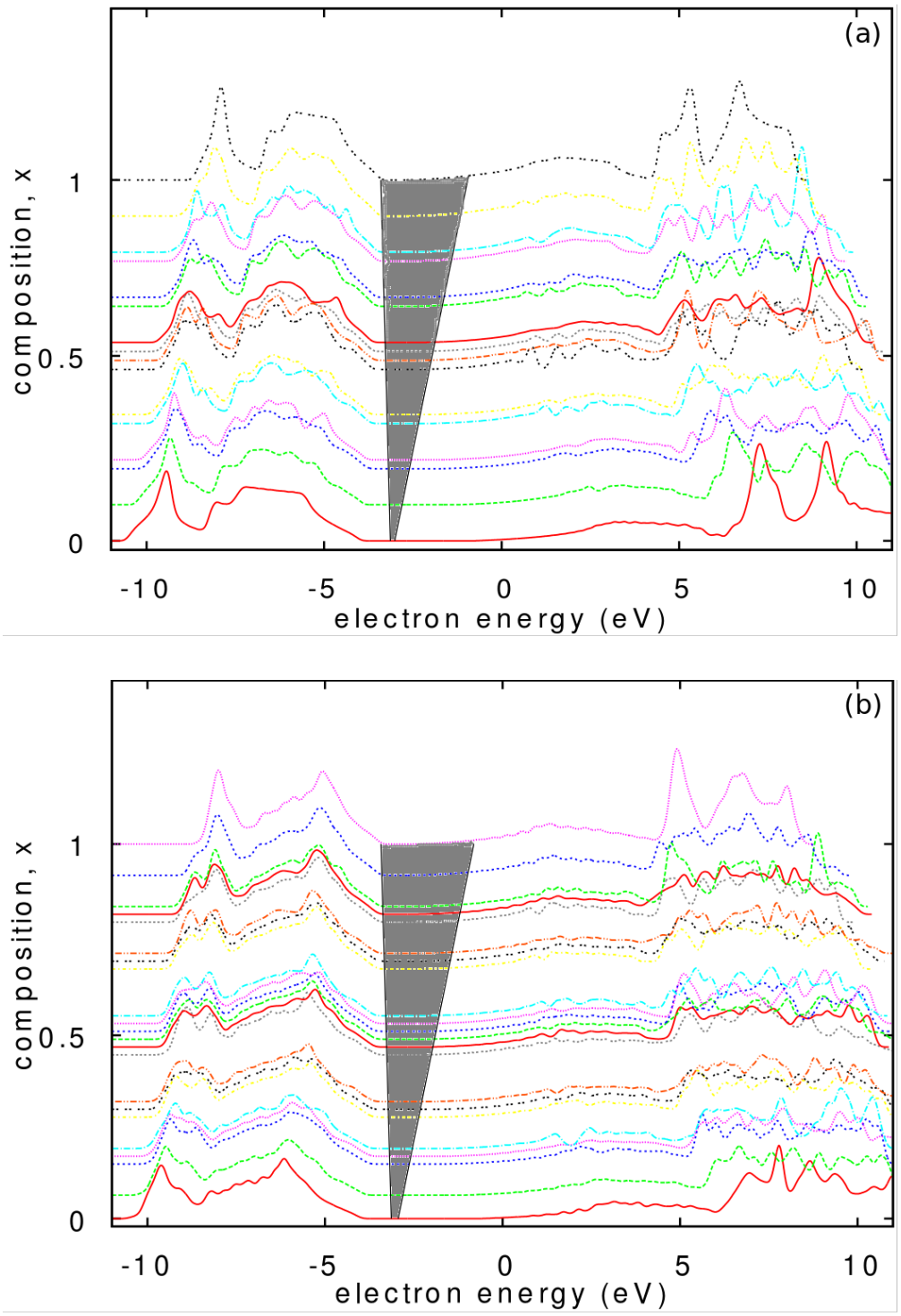

FIGURE 5.12: The variation density of states for the minimal basis set used in DFTB (see section 3.5) close to the Fermi level for for all clusters at each composition, shown together for 16 atom $In_xGa_{1-x}N$ unit cells of (a) zincblende and (b) wurtzite. The forbidden band gap area labelled as grey colour. The energy gap values shown underestimated values that's due to broadening effect.

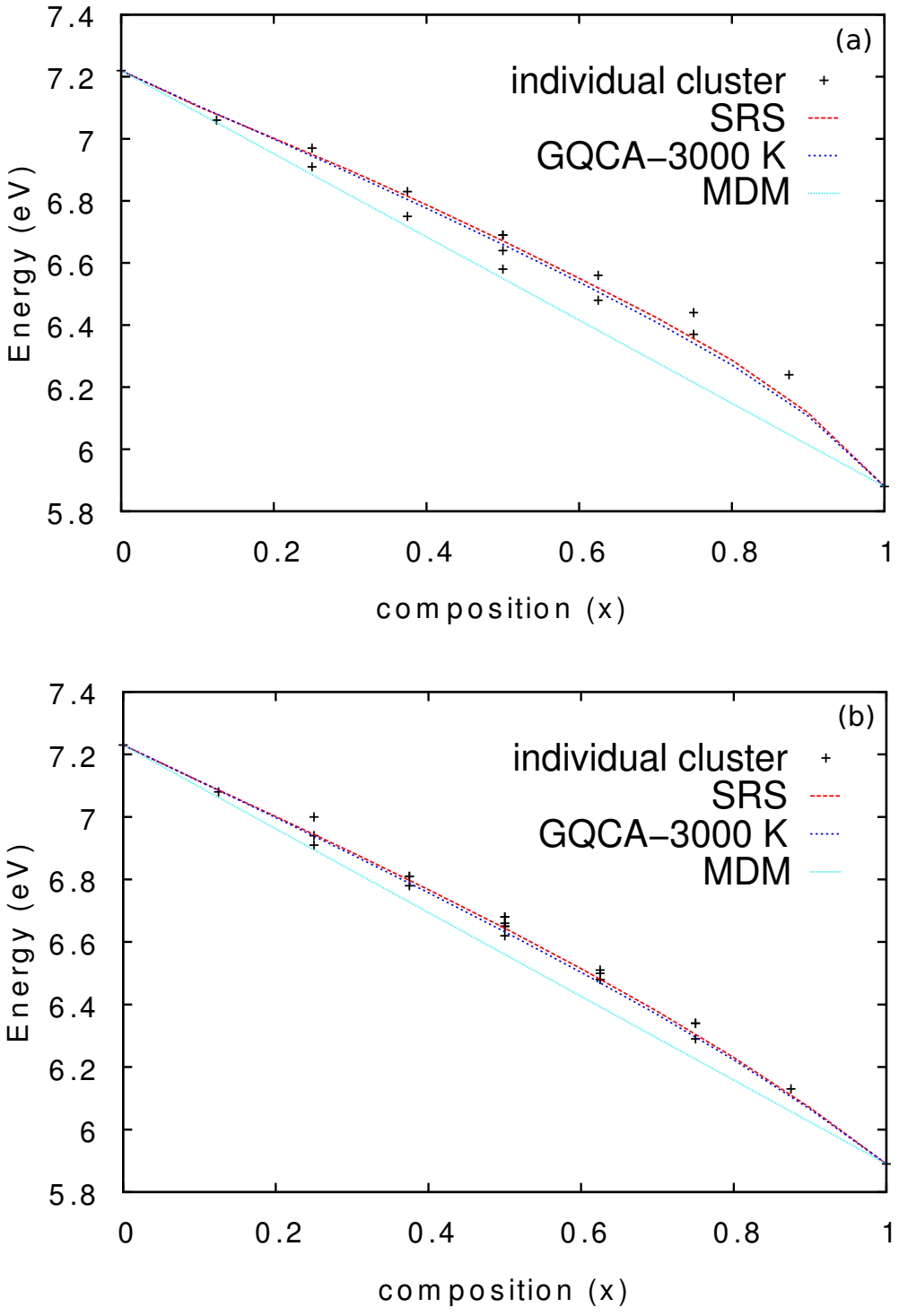

FIGURE 5.13: The variation of valence band width for 16 atom $In_xGa_{1-x}N$ unit cells of (a) zincblende and (b) wurtzite, with individual cluster valence band width also shown.

5.6 Elastic Constants

Figure 5.14 shows the variation of elastic constant for zincblende and wurtzite the values for GaN and InN (also shown in table 5.1) compared to VCA. These results show there is no difference between these results in the GaN case, but all the InN constants are smaller than the VCA results. The main difference between VCA and CEM results is that the variation between InN and GaN shows a noticeable dependence on x for some bowing parameters, where for wurtzite bowing parameter C_{11} ($b^{C_{11}}$) is about +24.61 GPa for $0 < x \leqslant 0.5$, = −42.41 GPa for $0.5 \leqslant x < 1.0$, $b^{C_{12}}$ =+7.95 GPa for $0 < x \leqslant 0.2$, −0.94 GPa $0.5 < x \leqslant 1.0$ (where the range for $0.2 \leqslant x < 0.5$ is difficult to fit), $b^{C_{13}}$ =+28.68 GPa for $0 < x \leqslant 0.3$ and +9.38 GPa for $0.3 \leqslant x < 1.0$ and there is no dependence on x for $b^{C_{33}}$, $b^{C_{44}}$, $b^{C_{66}}$, b^{B} and the bowing parameters values found are +28.22, −6.41, −14.61 and −13.27 GPa. In zincblende, the C_{11} elastic constant is well represented by the same value of bowing parameter over the whole composition range, where $b^{C_{11}}$= −33.68 GPa. But C_{12} strongly depends on x, where $b^{C_{12}}$ = +55.41 GPa for $0 < x \leqslant 0.4$, +4 GPa for $0.4 \leqslant x \leqslant 0.6$ and −8.75 GPa for $0.8 \leqslant x < 1.0$ (range between x=0.6 and x 0.8 is difficult to fit), C_{44} has negative bowing for whole range but with different values where $b^{C_{44}}$ = −152.76 GPa for $0 < x \leqslant 0.4$ and = −33.40 GPa for $0.4 \leqslant x < 1.0$ and finally the bulk modulus has two region in its bowing the b values approximately same (the difference is ≈1.4 GPa)but with different signs where b^{B} = +26.62 GPa for $0 < x \leqslant 0.5$, = −25.20 GPa for $0.5 \leqslant x < 1.0$.

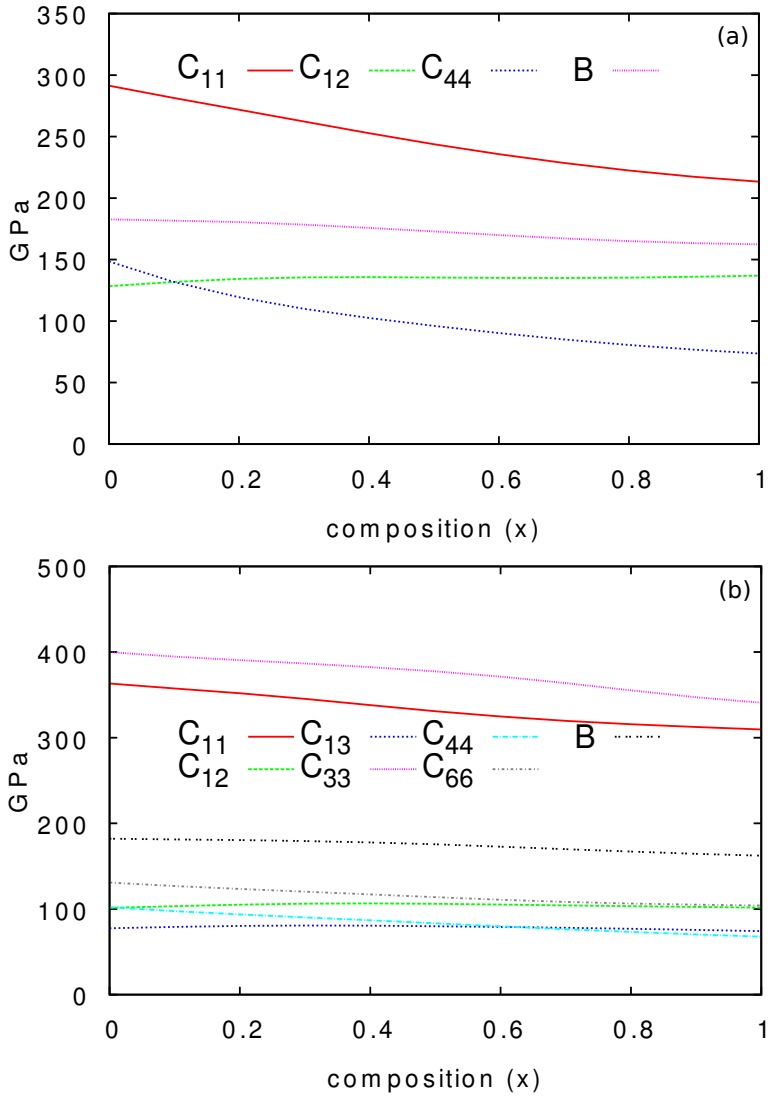

FIGURE 5.14: The variation of elastic constant for (a) zincblende and (b) wurtzite $In_xGa_{1-x}N$ alloy with composition (x) using the CEM and SRS models.

	C_{11}	C_{12}	C_{13}	C_{33}	C_{44}	C_{66}	B
WZ-GaN							
CEM	363	101	77	400	102	131	182
VCA	363	101	77	399	102	131	182
WZ-InN							
CEM	310	102	74	341	68	104	162
VCA	335	109	79	371	74	113	175

TABLE 5.1: The Elastic constants and Bulk modulus (GPa) for wurtzite GaN and InN calculated by CEM (SRS model) compared to VCA results.

5.7 Summary

The variation of energy gap and bowing parameter, lattice constants, elastic constant, bulk modulus and effective masses as a function of indium composition have been studied for fully optimized structures for the full range of x, with the cluster expansion method. This approach is a more physical method compared to VCA used in the previous chapter, as it is based on expanding the alloy in series of all atomic geometries for a given size unit cell. The total energies and the optimised atomic geometries for 8, 16 and 32 atom cells (with 7, 22 and 995 unique structures for wurtzite and 6, 16 and 990 unique structures for zincblende), the energy gaps, the energy gap bowing parameters for all cases and the variation of the effective masses, elastic constant, lattice constant and density of states were obtained for the full range of indium composition. The effect of the finite size of the simulation cells on the energy gap was investigated, showing clear evidence that the use of 8 and 16 atom cells result in an increase of the energy gap by about 2.99 % and 1.62 % respectively compared to 32 atom unit cells for wurtzite, and by 3.70 % and 1.62 % for zincblende respectively, at around x $\approx$ 0.4. Results for material grown on InGaN and GaN substrates (i.e. lattice matched or compressive pseudomorphic growth) have been studied for the 16-atom simulation cell case. The Generalized Quasi-chemical Approximation (GQCA) and its limiting cases of strict-regular solution model and Microscopic Decomposition Model have been employed for the alloy statistics.

In general all results obtained are an acceptable match to literature, but the level

of agreement varies from one parameter to another. The results obtained for energies gaps were in a good agreement with experimental results and in comparison to other calculations from literature: the deviation for wurtzite is found to be about 1% and 4.7% smaler comared to experimental data [130] at $x \backsimeq 0$ and $x \backsimeq 0.7$ respectively, and about 2.4% larger and 0.7% smaler at $x \backsimeq 0$ and $x \backsimeq 0.1$ respectively comared to experimental data [128]. The values obtained for the c lattice constants are about 1.4 % and 0.93 % for InN and GaN respectively. However, the effective masses for some specific local crystal structures have been found to have strange values. The contributions from these structures are presumably the mechanism underlying the loss of band-like character in the random InGaN alloys proposed by Popescu and Zunger [147].

Chapter 6

Conclusions and Future work

6.1 Conclusions

In this thesis, the properties of InN, GaN and their alloy InGaN have been studied using the density functional based tight binding method, using a new set of parameters for both InN and GaN, and by applying two different approaches to investigate InGaN alloys, namely the virtual crystal approximation and the cluster expansion method.

First, the properties of bulk InN and GaN have been calculated by using DFTB, for bulk wurtzite and zincblende InN and GaN these include band gaps, equilibrium lattice constants, elastic constants, bulk moduli, effective masses and density of states have been studied. Additionally, the variation of lattice constants and energy gaps with external pressure and the transition pressure between the wurtzite and rocksalt crystal structures have been investigate for both InN and GaN. A

good agreement has been obtained for these properties in comparision with previous experimental and also theoretical studies, with the exception of the value of transition pressure between polytypes especially in the GaN case.

The properties of wurtzite and zincblende InGaN have also been explored by using two different methods, the Virtual Crystal Approximation (VCA) and the Cluster Expansion Method (CEM). For the VCA, the variation of energy gaps, bowing parameter, lattice constants, elastic constant, bulk modulus and effective masses with indium composition have been studied. The obtained results found to be in acceptable agreement compared with the calculated and experimental results from literature for this alloy especially for energy gaps. Suggesting that VCA with charge self-consistency seems to be a good method to simulate the energy gaps in this system.

The same properties as above have then been recalculated with CEM which is a more physical method, based on expanding the alloy in series of all atomic geometries for a given size unit cell. The total energies and the optimised atomic geometries for 8, 16 and 32 atom cells (with 7, 22 and 995 unique structures for wurtzite and 6, 16 and 990 unique structures for zincblende), the energy gaps, the energy gap bowing parameters for all cases and the variation of the effective masses, elastic constant, lattice constant, density of states with indium composition. The effect of the finite size of the simulation cells on energy gap was investigated, showing clear evidence that 8 and 16 atom cell results increase the energy gap by about 2.99 % and 1.62 % compared to 32 atom unit cells for wurtzite, and 3.70 % and 1.62 % for zincblende respectively, at around x $\approx$ 0.4. Results for material

grown on InGaN and GaN substrates (i.e. lattice matched or compressive pseudomorphic growth) have been studied for the 16-atom simulation cell case. The generalized quasi-chemical approximation and its limiting cases of strict-regular solution model and microscopic decomposition Model have been employed for the alloy statistics.

In general all results obtained are an acceptable match to literature, but level of agreement is varies from one parameter to another, where as e.g. the results obtained for energies gaps were in a good agreement with experimental results and compared to other calculation from literature while the values obtained for c lattice constants are overestimated by about 1.4 % and 0.93 % for InN and GaN respectively, also the effective masses for some specific local crystal structures have been found to have strange values. The contributions from these structures are presumably the mechanism underlying the loss of band-like character in the random InGaN alloys proposed by Popescu and Zunger [147]. It is an open question, whether their method could be extended beyond special quasirandom structures (SQS), to investigate the (perhaps) more physical CEM methods.

6.2 Future work

There are many properties and applications of group-III nitrides and their alloys, have been investigated. But, there are still many open questions in III-group nitrides and their alloys. Here some possible paths, which can possibly inspire new projects further research, starting from the results presented here;

- Improve the parameter set, to amendment the value of c lattice constant and the value of the transition pressure between polytypes especially in the GaN case. In this case the fitting process should focusing on the transition pressure and not just the energy gap and the lattice constant.

- Investigate the piezoelectric properties, which are important where the electric fields caused by strain in devices impact their operation, for example the internal field breaks the symmetry of the quantum well, causing spatial separation of the electron and hole wave functions and hence reduces the electron-hole overlap function [148]. For this task one could start with calculating the Born effective charges[1]. Then the piezoelectric tensor can be calculated as the polarization derivative with respect to strain, when the macroscopic field is kept vanishingly small [150], alternatively the piezoelectric constants in semiconductors can be expressed in terms of the in plane strain and the Born effective charges [151].

- Study the optical properties which are important for the optoelectronic devices. For example what so called droop problem or the efficiency droop in green light emitted diodes (LEDs), which occur in optoelectronic devices based on III-nitrides material where the efficiency of the LEDs drops down when the electric power input increases. Many loss mechanisms have been suggested for this phenomenon [152]. For example the virtual crystal calculation done by Delaney *et al.* [153] for finding out which mechanism is

[1]Born effective charges give the atomic force appearing in response to a first-order change in the macroscopic electric field [149]

responsible for Auger recombination, could be recalculated by using cluster expansion methods which are more physical in nature.

Bibliography

[1] Bo-Ting Liou. *Jpn. J. Appl. Phys.*, 47:3350, 2008.

[2] Akio Yamamoto, Md.R̃. Islam, Ting-Ting Kang, and Akihiro Hashimoto. *Phys. Stat. Sol. (c)*, 7:1309, 2010.

[3] Si-Hyun Parka and Heonsu Jeon. *OPTICAL REVIEW*, 13:20, 2006.

[4] Tien-Chang Lu, Jun-Rong Chen, Shih-Wei Chen, Hao-Chung Kuo, Chien-Cheng Kuo, Cheng-Chung Lee, and Shing-Chung Wang. *IEEE Journal of selected Topics in Quantum Electroics*, 15:850, 2009.

[5] Junqiao Wu. *J. Appl. Phys.*, 106:011101, 2009.

[6] S. Strite and H. Morkoç. *J. Vac. Sci. Technol. B*, 10:1237, 1992.

[7] Mingwei Zhu, Shi You, Theeradetch Detchprohm, Tanya Paskova, and Christian Preble, Edward A.and Wetzel. *Phys. Stat. Sol. (A)*, 207:1305, 2010.

[8] I. Gorczyca, S. P. Łepkowski, T. Suski, N. E. Christensen, and A. Svane. *Phys. Rev. B*, 80:075202, 2009.

[9] Macho Anani, Christian Mathieu, Mohammed Khadraoui, Zouaoui Chama, Sara Lebid, and Youcef Amar. *Microelectronics Journal*, 40:427, 2009.

[10] T. Hanada. *Oxide and Nitride Semiconductors: Processing, Properties, and Applications*. Springer, Berlin Heidelberg, 2009.

[11] Yoshio Waseda, Eiichiro Matsubara, and Kozo Shinoda. *X-Ray Diffraction Crystallography*. Springer,Berlin Heidelberg, 2011.

[12] Man-Yi Duan, Lin He, Ming Xu, Ming-Yao Xu, Shuyan Xu, and Kostya(Ken) Ostrikov. *Phys. Rev. B*, 81:033102, 2010.

[13] Bernard Gil. *Semiconductors: Data Handbook*. Oxford University Press, 2002.

[14] Sung-Kyu Kim, Se-Young Jeong, and Chae-Ryong Cho. *Appl. Phys. Lett.*, 82:562, 2003.

[15] Priya Gopal and Nicola A. Spaldin. *Journal of Electronic Materials*, 35:538, 2006.

[16] mindat.org lonsdaleite. http://www.mindat.org/min-2431.html. Accessed: May 2013.

[17] I. Petrov, E. Mojab, R. C. Powell, J. E. Greene, L. Hultman, and J.-E. Sundgren. *Appl. Phys. Lett.*, 60:2491, 1992.

[18] A.-B. Chen and A. Sher. *Semiconductor alloys : Physics and materials engineering*. Plenum Press, 1995.

[19] S. J. Joshua. *Symmetry Principles and Magnetic Symmetry in solid State Physics*. IOP Publishing, 1991.

[20] L. C. de Carvalho, A. Schleife, and F. Bechstedt. *Phys. Rev. B*, 84:195105, 2011.

[21] I. Vurgaftman and J. R. Meyer. *J. Appl. Phys.*, 94:3675, 2003.

[22] Niladri Sarkar and Subhasis Ghosh. *Solid State Communications*, 149:1288, 2009.

[23] M. Landmann, E. Rauls, W. G. Schmidt, Marcus Röppischer, Christoph Cobet, Norbert Esser, Thorsten Schupp, Donat J. As, Martin Feneberg, and Rüdiger Goldhahn. *Phys. Rev. B*, 87:195210, 2013.

[24] L. K. Teles, J. Furthmüller, L. M. Scolfaro, J. R. Leite, and F. Bechstedt. *Phys. Rev. B*, 62:2475, 2000.

[25] T. L. Tansley and C. P. Foley. *J. Appl. Phys.*, 59:3241, 1986.

[26] J. Schörmann, D. J. As, K. Lischka, P. Schley, R. Goldhahn, S. F. Li, W. Löffler, M. Hetterich, and H. Kalt. *Appl. Phys. Lett.*, 89:261903, 2006.

[27] P. Rinke, M. Winkelnkemper, A. Qteish, D. Bimberg, J. Neugebauer, and M. Scheffler. *Phys. Rev. B*, 77:075202, 2008.

[28] J. Wu, W. Walukiewicz, K. M. Yu, J. W. Ager III, E. E. Haller, H. Lu, W. J. Schaff, Yoshiki Saito, and Yasushi Nanishi. *Appl. Phys. Lett.*, 80:3967, 2002.

[29] O. Donmez, M. Yilmaz, A. Erol, B. Ulug, M. C. Arikan, A. Ulug, A. O. Ajagunna, E. Iliopoulos, and A. Georgakilas. *Phys. Stat. Sol. (b)*, 248:1172, 2011.

[30] A. Chandolu, D. Y. Song, M. E. Holtz, I. Gherasoiu, S. A. Nikishin, A. Bernussi, and M. W. Holtz. *Journal of Electronic Materials*, 38:557, 2009.

[31] V. Yu. Davydov, A. A. Klochikhin, V. V. Emtsev, D. A. Kurdyukov, S. V. Ivanov, V. A. Vekshin, F. Bechstedt, Furthmüller J., J. Aderhold, J. Graul, A. V. Mudryi, H. Harima, A. Hashimoto, A. Yamamoto, and Haller E. E. *Phys. Stat. Sol. (b)*, 234:787, 2002.

[32] Matthew D. McCluskey and Eugene E. Haller. *Dopants and Defects in Semiconductors*. CRC Press-Taylor & Francis Group, LLc, 2012.

[33] Qi-C. Sun, Lena Yadgarov, Rita Rosentsveig, Gotthard Seifert, Reshef Tenne, and Musfeldt Janice L. *ACS Nano*, 7:3506, 2013.

[34] Peter Capper. *Narrow Gap II-VI Compounds for Optoelectronic and Electromagnetic Applications*. T. J. Press International Ltd. Padstow, Cornwall, 1997.

[35] Seoung-Hwan Park, Doyeol Ahnand, and Shun-Lien Chuang. *IEEE Journal of Quantum Electroics*, 43:1175, 2007.

[36] Chihiro Hamaguchi. *Basic Semiconductor Physics*. Springer-Verlag Berlin Hidelberg, 2010.

[37] A. Kasic, M. Schubert, S. Einfeldt, D. Hommel, and T. E. Tiwald. *Phys. Rev. B*, 62:7365, 2000.

[38] A. V. Rodina, M. Dietrich, A. Göldner, L. Eckey, A. Hoffmann, A. L. Efros, M. Rosen, and Meyer B. K. *Phys. Rev. B*, 64:115204, 2001.

[39] T. Hofmann, V. Darakchieva, B. Monemar, H. LU, W. J. Schaff, and M. Schubert. *Journal of Electronic Materials*, 37:611, 2008.

[40] Charles Kittel. *Introduction to Solide State Physics*. John Wiley & Sons, 1996.

[41] S. C. Jain, M. Willander, J. Narayan, and R. Van Overstraeten. *J. Appl. Phys.*, 87:965, 2000.

[42] Bilbao Crystallographic Server. http://www.cryst.ehu.es/. Accessed: Mar. 2013.

[43] M. E. Sherwin and T. J. Drummond. *J. Appl. Phys.*, 69:8423, 1991.

[44] Martin T. Dove. *Structure and Dynamics an atmic view of materials*. Oxford University Press, 2003.

[45] K. Kim, W. R. L. Lambrecht, and B. Segall. *Phys. Rev. B*, 53:16310, 1996.

[46] Vyacheslav Kachkanov. *Structural Properties of Luminescent Nitride semiconductors*. PhD thesis, Strathclyde University, 2006.

[47] Hadis Morkoç. *Journal of Materials Science: Materials in Electronics*, 12: 677, 2001.

[48] C. E. C. Dam, A. P. Grzegorczyk, P. R. Hageman, and P. K. Larsen. *Journal of Crystal Growth*, 290:473, 2006.

[49] Xinqiang Wang and Akihiko Yoshikawa. *Progress in Crystal Growth and Characterization of Materials*, 48/49:42, 2004.

[50] J. Elsner, R. Jones, M. I. Heggie, P. K. Sitch, M. Haugk, Th. Frauenheim, S. Öberg, and P. R. Briddon. *Phys. Rev. B*, 58:12571, 1998.

[51] Attila Szabo and Neil S. Ostlund. *Modern Quantum chemistry.* McGraw-Hill, 1989.

[52] P. Hohenberg and W. Kohn. *Phys. Rev.*, 136:B864, 1964.

[53] W. Matthew, C. Foulkes, and Roger Haydock. *Phys. Rev. B*, 39:12520, 1989.

[54] Th. Frauenheim, G. Seifert, M. Elstner, Z. Hajnal, G. Jungnickel, D. Porezag, S. Suhai, and R. Scholz. *Phys. Stat. Sol. (b)*, 217:41, 2000.

[55] M. Elstner, D. Porezag, G. Jungnickel, J. Elsner, M. Haugk, Th. Frauenheim, S. Suhai, and G Seifert. *Phys. Rev. B*, 58:7260, 1998.

[56] G Seifert. *J. Phys. Chem. A*, 111:5609, 2007.

[57] Augusto F. Oliveira, Gotthard Seifert, Thomas Heine, and Hélio A. Duarte. *J. Braz. Chem. Soc.*, 20:1193, 2009.

[58] D. A. Papaconstantopoulos and M. J. Mehl. *J. Phys.: Condens. Matter*, 15: R413, 2003.

[59] Eunan J. McEniry, Ralf Drautz, and Georg K. H. Madsen. *J. Phys.: Condens. Matter*, 25:115502, 2013.

[60] P. L. Meena, P. K. Jain, N. Kumar, and K. S. Meena. *Acta Chim. Pharm. Indica*, 2:32, 2012.

[61] Otfried Madelung. *Introduction to Solid-State Theory.* Springer-Verlag Berlin Hidelberg, 1996.

[62] D. J. Chadi. *Phys. Rev. B*, 16:790, 1977.

[63] Sergej Konschuh, Martin Gmitra, and Jaroslav Fabian. *Phys. Rev. B*, 82: 245412, 2010.

[64] J. J. Mortensen, L. B. Hansen, and K. W. Jacobsen. *Phys. Rev. B*, 71: 035109, 2005.

[65] Mike Finnis. *Interatomic Forces in condensed matter.* Oxford University Press, 2003.

[66] Pekka Koskinen and Ville Mäkinen. *Computational Materials Science*, 47: 237, 2009.

[67] Hendrik J. Monkhorst and James D. Pack. *Phys. Rev. B*, 13:5188, 1976.

[68] J. M. Thijssen. *Computational Physics.* Cambridge University Press, 2007.

[69] David M. Hirst. *A Computational Approach to Chemistry.* BlackWell Scientific Publications, 1990.

[70] Yasuhiko Arakawa. *IEEE Journal of selected Topics in Quantum Electroics*, 8:4, 2002.

[71] J. Wu, W. Walukiewicz, W. Shan, K. M. Yu, J. W. Ager III, S. X. Li, E. E. Haller, H. Lu, and W. J. Schaff. *J. Appl. Phys.*, 94:4457, 2003.

[72] F. Bechstedt and J. Furthmüller. *Journal of Crystal Growth*, 246:315, 2002.

[73] B. Aradi, B. Hourahine, and T. Frauenheim. *J. Phys. Chem.*, 111:5678, 2007.

[74] S. Sanna, B. Hourahine, Ü. Gerstmann, and Th. Frauenheim. *Phys. Rev. B*, 76:155128, 2007.

[75] V. Darakchieva, B. Monemar, and A. Usui. *Appl. Phys. Lett.*, 91:031911, 2007.

[76] R. C. Powell, N. E. Lee, Y. W. Kim, and J. E. Greene. *J. Appl. Phys.*, 73: 189, 1993.

[77] P. Spechta, J. C. Ho, X. Xu, R. Armitagea, E. R. Webera, E. Erni, and Kisielowski C. *Journal of Crystal Growth*, 288:225, 2006.

[78] M. A. Moram, Z. H. Barber, and C. J. Humphreys. *J. Appl. Phys.*, 102: 023505, 2007.

[79] Hisanon Yamane, Masahiko Shimada, and Francis J. DiSalvo. *Materials Letters*, 42:66, 2000.

[80] Claudia Bungaro, Krzysztof Rapcewicz, and J. Bernholc. *Phys. Rev. B*, 61: 6720, 2000.

[81] A. Tabata, A. P. Lima, L. K. Teles, L. M. R. Scolfaro, J. R. Leite, V. Lemos, B. Schöttker, T. Frey, D. Schikora, and K Lischka. *Appl. Phys. Lett.*, 74: 362, 1999.

[82] P Rinke, M. Scheffler, A. Qteish, M. Winkelnkemper, D. Bimberg, and J. Neugebauer. *Appl. Phys. Lett.*, 89:161919, 2006.

[83] R. Dingle, D. D. Sell, S. E. Stokowski, and M. Ilegems. *Phys. Rev. B*, 4: 1211, 1971.

[84] V. A. Tyagai, A. M. Evstigneev, A. N. Krasiko, A. F. Andreeva, and V. Ya. Malakhov. *Sov. Phys. Semicond.*, 11:1257, 1977.

[85] M. Smith, G. D. Chen, J. Z. Li, J. Y. Lin, H. X. Jiang, A. Salvador, W. K. Kim, O. Aktas, A. Botchkarev, and H. Morkoç. *Appl. Phys. Lett.*, 67:3387, 1995.

[86] H. P. Maruska and J. J. Tietjen. *Appl. Phys. Lett.*, 15:327, 1969.

[87] Takashi Matsuoka, Hiroshi Okamoto, Masashi Nakao, Hiroshi Harima, and Eiji Kurimoto. *Appl. Phys. Lett.*, 81:1246, 2002.

[88] B. Monemar. *Phys. Rev. B*, 10:676, 1974.

[89] H. Okumura, S. Yoshida, and T. Okahisa. *Appl. Phys. Lett.*, 64:2997, 1994.

[90] I. Vurgaftman, J. R. Meyer, and L. R. Ram-Mohan. *J. Appl. Phys.*, 89:5815, 2001.

[91] G. Ramírez-Flores, H. Navarro-Contreras, A. Lastras-Martìnez, R. C. Powell, and J. E. Greene. *Phys. Rev. B*, 50:8433, 1994.

[92] H. Okumura, K. Ohta, K. Ando, W. W. Rlihle, T. Nagatomo, and S. Yoshida. *Solid-State Electronics*, 41:201, 1997.

[93] Ching-Lien Hsiao, Ting-Wei Liu, Chien-Ting Wu, Hsu-Cheng Hsu, Geng-Ming Hsu, Li-Chyong Chen, Wen-Yu Shiao, C. C. Yang, Andreas Gällström,

Per-Olof Holtz, Chia-Chun Chen, and Kuei-Hsien Chen. *Appl. Phys. Lett.*, 92:111914, 2008.

[94] M. Cardona and N. E. Christensen. *Solid State Communications*, 116:421, 2000.

[95] Y. C. Yeo, T. C. Chong, and M. F. Li. *J. Appl. Phys.*, 83:1429, 1998.

[96] K. Kim, W. R. L. Lambrecht, and B. Segall. *Phys. Rev. B*, 56:7363, 1997.

[97] A. Punya and W. R. L. Lambrecht. *Phys. Rev. B*, 85:195147, 2012.

[98] Bernhard Grundkötter-Stock, Viktor Bezugly, Jens Kunstmann, Gianaurelio Cuniberti, Thomas Frauenheim, and Thomas A. Niehaus. *J. Chem. Theory Comput.*, 8:1153, 2012.

[99] L. E. Ramos, L. K. Teles, L. M. R. Scolfaro, J. L. P. Castineira, A. L. Rosa, and Leite J. R. *Phys. Rev. B*, 63:165210, 2001.

[100] P. Schley, C. Napierala, R. Goldhahn, G. Gobsch, J. Schörmann, D. J. As, M. Lischka, K. Feneberg, K. Thonke, F. Fuchs, and Bechstedt F. *Phys. Stat. sol. (c)*, 5:2342, 2008.

[101] Martin Magnuson, Maurizio Mattesini, Carina Höglund, Jens Birch, and Lars Hultman. *Phys. Rev. B*, 81:085125, 2010.

[102] Alexander Thorsten Blumenau. *The Modelling of Dislocations in Semiconductor Crystals*. PhD thesis, Paderborn University, 2002.

[103] A. Polian, M. Grimsditch, and I. Grzegory. *J. Appl. Phys.*, 79:3343, 1996.

[104] V. Yu. Davydov, Yu.Ẽ. Kitaev, I. N. Goncharuk, A. N. Smirnov, J. Graul, O. Semchinova, D. Uffmann, M. B. Smirnov, A. P. Mirgorodsky, and R. A. Evarestov. *Phys. Rev. B*, 58:12899, 1998.

[105] A. F. Wright. *J. Appl. Phys.*, 82:2833, 1997.

[106] S. P. Łepkowski, J. A. Majewski, and G. Jurczak. *Phys. Rev. B*, 72:245201, 2005.

[107] Kanoknan Sarasamak, Sukit Limpijumnong, and Walter R. L. Lambrecht. *Phys. Rev. B*, 82:035201, 2010.

[108] K. Sarasamak, A. J. Kulkarni, M. Zhou, and S. Limpijumnong. *Phys. Rev. B*, 77:024104, 2008.

[109] Vijay Rawat, Dmitri N. Zakharov, Eric A. Stach, and Timothy D. Sands. *Phys. Rev. B*, 80:024114, 2009.

[110] Prabhsharan Kaur, S. S. Sekhon, and Vijay Kumar. *J. Chem. Phys.*, 138: 114310, 2013.

[111] Luis Mancera, Jairo A. Rodríguez, and Noboru Takeuchi. *Phys. Stat. Sol. (b)*, 241:2424, 2004.

[112] M. P. Halsall, P. Harmer, P. J. Parbrook, and S. J. Henley. *Phys. Rev. B*, 69:235207, 2004.

[113] Lok C. Lew Yan Voon. *Electronic and Optical Properties of Semiconductors: A Study Based on the Empirical Tight Binding Model*. Dissertation.Com, 1997.

[114] M. Jaros. *Rep. Prog. Phys.*, 48:1091, 1985.

[115] Martin Fuchs and Matthias Scheffler. *Computer Physics Communications*, 119:67, 1999.

[116] C. Hamaguchi. *Basic Semiconductor Physics*. Springer-Verlag, Berlin Heidelberg, 2010.

[117] T. G. Dargam, R. B. Capaz, and B. Koiller. *Brazilian Journal of Physics*, 27/A:4, 1997.

[118] S. J. Lee, T. S. Kwon, K. Nahm, and C. K. Kim. *J. Phys. Cond. Matt.*, 2: 3253, 1990.

[119] L. Bellaiche, S.-H. Wei, and A. Zunger. *Appl. Phys. Lett.*, 70:3558, 1997.

[120] M. Henini. *Dilute Nitride Semiconductors*. Elsevier, 2005.

[121] S. Berrah, A. Boukortt, and H. Abid. *Semiconductor Physics, Quantum Electronics & Optoelectronics*, 11:59, 2008.

[122] R. R. Pelá, C. Caetano, M. Marques, L. G. Ferreira, J. Furthmüller, and L. K. Teles. *Appl. Phys. Lett.*, 98:151907, 2011.

[123] M. Moret, B. Gil, S. Ruffenach, O. Briot, Ch. Giesen, M. Heuken, S. Rushworth, T. Leese, and M. Succi. *Journal of Crystal Growth*, 311:2795, 2009.

[124] Y.-K. Kuo, B.-T. Liou, S.-H. Yen, and H.-Y. Chu. *Optics Communications*, 237:363, 2004.

[125] Y.-K. Kuo, H.-Y. Chu, S.-H. Yen, B.-T. Liou, and M.-L. Chen. *Optics Communications*, 280:153, 2004.

[126] I. Gorczyca, N. E. Christensen, A. Svane, K. Laaksonen, and R. M. Nieminen. *Acta Physica Polonica A*, 112:203, 2007.

[127] P. G. Moses and C. G. Van de Walle. *Appl. Phys. Lett.*, 96:021908, 2010.

[128] D. G. Pacheco-Salazar, F. Leite, J. R. Cerdeira, E. A. Meneses, S. F. Li, D. J. As, and K. Lischka. *Semicond. Sci. Technol.*, 21:846, 2006.

[129] J. Wu, W. Walukiewicz, K. M. Yu, J. W. Ager III, E. E. Haller, H. Lu, and W. J. Schaff. *Appl. Phys. Lett.*, 80:4741, 2002.

[130] G. Franssen, I. Gorczyca, T. Suski, A. Kamińska, J. Pereiro, E. Muñoz, E. Iliopoulos, A. Georgakilas, S. B. Che, Y. Ishitani, A. Yoshikawa, N. E. Christensen, and Svane A. *J. Appl. Phys.*, 103:033514, 2008.

[131] C. Shen, S. G. Mayorga, R. Biagioni, C. Piskoti, M. Ishigami, A. Zettl, and N. Bartlett. *Journal of Solid State Chemistry*, 147:748, 1999.

[132] D. Vogel, P. Krüger, and J. Pollmann. *Phys. Rev. B*, 55:12836, 1987.

[133] B.-T. Liou, S.-H. Yen, and Y.-K. Kou. *Appl. Phys.*, 81:1459, 2005.

[134] Y.-K. Kuo, W.-W. Lin, and J. Lin. *Jpn. J. Appl. Phys.*, 40:3157, 2001.

[135] D. Bagayoko and L. Franklin. *J. Appl. Phys.*, 97:123708, 2005.

[136] L. C. de Carvalho, A. Schleife, J. Furthmüller, and F. Bechstedt. *Phys. Rev. B*, 85:115121, 2012.

[137] A. Sher and M. van Schifgaarde. *Phys. Rev. B*, 36:4279, 1987.

[138] A. Schleife, M. Eisenacher, C. Rödl, F. Fuchs, J. Furthmüller, and F. Bechstedt. *Phys. Rev. B*, 81:245210, 2010.

[139] M. Ferhat, J. Furthmüller, and F. Bechstedt. *Appl. Phys. Lett.*, 80:1394, 2002.

[140] E. Iliopoulos, A. Adikimenakis, C. Giesen, M. Heuken, and A. Georgakilas. *Appl. Phys. Lett.*, 92:191907, 2008.

[141] E. Sakalauskas, H. Behmenburg, C. Hums, P. Schley, G. Rossbach, C. Giesen, M. Heuken, H. Kalisch, R. H. Jansen, J. Bläsing, A. Dadgar, A. Krost, and R. Goldhahn. *J. Phys. D: Appl. Phys.*, 43:365102, 2010.

[142] C. Caetano, L. K. Teles, M. Marques, A. Dal Pino Jr., and L. G. Ferreira. *Phys. Rev. B*, 74:045215, 2006.

[143] Ferhat M. and F. Bechstedt. *Phys. Rev. B*, 65:075213, 2002.

[144] Z. Liliental-Weber, K. M. Yu, M. Hawkridge, S. Bedair, A. E. Berman, A. Emara, D. R. Khanal, J. Wu, J. Domagala, and J. Bak-Misiuk. *Phys. Stat. Sol. (C)*, 6:2626, 2009.

[145] C. G. Van de Walle, M. D. McCluskey, C. P. Master, and N. M. Romano, L. T. Johnson. *Materials Science and Engineering B*, 59:274, 1999.

[146] Y. Huang, A. Melton, B. Jampana, M. Jamil, J.-H. Ryou, R. D. Dupuis, and I. T. Ferguson. *J. Appl. Phys.*, 110:064908, 2011.

[147] V. Popescu and A. Zunger. *Phys. Rev. Lett.*, 104:236403, 2010.

[148] I. H. Brown, I. A. Pope, P. M. Smowton, P. Blood, J. D. Thomson, W. W. Chow, D. P. Bour, and M. Kneissl. *Appl. Phys. Lett.*, 86:131108, 2005.

[149] X. Wang and D. Vanderbilt. *Phys. Rev. B*, 75:115116, 2007.

[150] Raffaele Resta. *Rev. Mod. Phys.*, 66:899, 1994.

[151] D. Vaschenko, G.and Patel, C. S. Menoni, N. F. Gardner, J. Sun, W. Götz, C. N. Tomé, and B. Clausen. *Phys. Rev. B*, 64:241308(R), 2001.

[152] Y. C. Shen, G. O. Mueller, S. Watanabe, N. F. Gardner, A. Munkholm, and M. R. Krames. *Appl. Phys. Lett.*, 91:141101, 2007.

[153] Kris T. Delaney, Patrick Rinke, and C. G. Walle, Van de Walle. *Appl. Phys. Lett.*, 94:191109, 2009.